Lithium Manganese Oxide Modified with Copper-Gold Nanocomposite Cladding - a Potential Novel Cathode Material for Spinel Type Lithium-ion Batteries

UNIVERSITY *of the*
WESTERN CAPE

By

Sarre Kadia Myra Nzaba

A mini-thesis submitted in partial fulfilment of the requirements for the degree of

Magister Scientiae in Nanoscience

Faculty of Science

University of the Western Cape

Bellville, Cape Town, South Africa

Supervisor: **Prof Emmanuel I. Iwuoha**

Co-Supervisor: **Dr N Ross**

December, 2014

ABSTRACT

Spinel lithium manganese oxide ($LiMn_2O_4$), for its low cost, easy preparation and nontoxicity, is regarded as a promising cathode material for lithium-ion batteries. However, a key problem prohibiting it from large scale commercialization is its severe capacity fading during cycling. The improvement of electrochemical cycling stability is greatly attributed to the suppression of Jahn-Teller distortion (Robertson *et al*., 1997) at the surface of the spinel $LiMn_2O_4$ particles. These side reactions result in Mn^{2+} dissolution mainly at the surface of the cathode during cycling, therefore surface modification of the cathode is deemed an effective way to reduce side reactions. The utilization of a nanocomposite which comprises of metallic Cu and Au were of interest because their oxidation gives rise to a variety of catalytically active configurations which advances the electrochemical property of Li-ion battery. In this research study, an experimental strategy based on doping the $LiMn_2O_4$ with small amounts of Cu-Au nanocomposite cations for substituting the Mn^{3+} ions, responsible for disproportionation, was employed in order to increase conductivity, improve structural stability and cycle life during successive charge and discharge cycles. The spinel cathode material was synthesized by co-precipitation method from a reaction of lithium hydroxide and manganese acetate using 1:2 ratio. The Cu-Au nanocomposite was synthesized via a chemical reduction method using copper acetate and gold acetate in a 1:3 ratio. Powder samples of $LiM_xMn_2O_4$ (M = Cu-Au nanocomposite) was prepared from a mixture of stoichiometric amounts of Cu-Au nanocomposite and $LiMn_2O_4$ precursor. The novel $LiM_xMn_2O_4$ material has a larger surface area which increases the Li^+ diffusion coefficient and reduces the volumetric changes and lattice stresses caused by repeated Li^+ insertion and expulsion. Structural and morphological sample analysis revealed that the modified cathode material have good crystallinity and well dispersed particles. These results corroborated the electrochemical behaviour of $LiM_xMn_2O_4$ examined by cyclic voltammetry (CV) and electrochemical impedance spectroscopy (EIS). The diffusion coefficients for $LiMn_2O_4$ and $LiM_xMn_{2-x}O_4$ obtained are 1.90 $x10^{-3}$ cm^2 / s and 6.09 $x10^{-3}$ cm^2 / s respectively which proved that the Cu-Au nanocomposite with energy band gap of 2.28 eV, effectively improved the electrochemical property. The charge / discharge value obtained from integrating the area under the curve of the oxidation peak and reduction peak for $LiM_xMn_{2-x}O_4$ was 263.16 and 153.61 mAh / g compared to 239.16 mAh / g and 120 mAh / g for $LiMn_2O_4$. It is demonstrated that the presence of Cu-Au nanocomposite reduced side reactions and effectively improved the electrochemical performance of $LiMn_2O_4$.

KEYWORDS

Energy

Lithium-ion batteries

Battery cathode materials

Lithium manganese oxide

Nanotechnology

Cu-Au nanocomposite

Doping mode

Cyclic voltammetry (CV)

Electrochemical Impedance Spectroscopy (EIS)

Energy band gap, Eg

DECLARATION

I, hereby declare that: "**Lithium manganese oxide modified with copper-gold nanocomposite cladding- a potential novel cathode material for spinel type lithium-ion batteries**" is my own work; that it has not been previously submitted for any degree or examination in any other university or higher education; and that all the sources and quotations have been indicated and acknowledged by complete references.

Sarre Kadia Myra Nzaba

Signed: 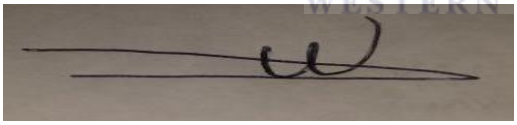

Date: December 2014

DEDICATION

I dedicate this thesis to
God Almighty,

My lovely husband

Lagouge Tartibu Kwanda,

My Children

Anais Tartibu Ngala and Yanis Tartibu

And

My parents

Mr Nzaba Charles and Mrs Moutsila Diambaka Olga Bertile

ACKNOWLEDGEMENTS

To my lovely husband- thank you for your love, care and encouragements. To my children Anais and Yanis Tartibu -the joy of being a mother gave me a new strength. To my parents Nzaba Charles and Moutsila Diambaka Olga Bertile- thank you for your prayers, love, care, and education. Thank you for the opportunity you gave me to study in a foreign country. This is my only way to make you proud. To my aunty, Lydie Gisele Moustila and uncle Christian Gervais Moutsila I really appreciated all the support you gave me. To my grand-mother, Moutsila Leko Jacqueline -I am happy because you have lived to see this day happened. To my brothers and sisters: Naomy Nzaba, Ornella Nzaba, Bechal Ores Lemeilleur Nzaba, Believe Nzaba, Francilia Moutsila, Jodie Chriscinthe Mapakou, Vianey Mapakou, Prince Moutsila, Avy Moutsila, Givry Moutsila, Saint-Christie Moutsila, Maye Moutsila,- I thank you for your affection and care. To my in-laws, Jean-louis Tartibu Nyembo, Georgettes Ngala, and my sister in law Laeticia Kabole Tartibu - thank you for your encouragements and prayers throughout. To aunty Cathrine Makanya -I am forever grateful to you for all your assistance with the kids each time I finished late with my experiments. To my dear friends and classmates though, not mentioned by name I sincerely thank you for all the times you called or sent messages to support me. To all the SensorLab members -I say thank you for all the help I received from each one of you. To the Chemistry Department especially, Prof Farouk Ameer, Prof P Baker, Dr Nazeem Jahed, Mrs Whilma Jackson I am grateful for everything you have done for me. To Dr Natasha Ross Dr Masikini Milua and Dr C Ikpo thank you for your assistance as well as your availability though it was not easy with your busy schedule, from the bottom of my heart I say thank you. To Prof Emmanuel I. Iwuoha- thank you for giving an opportunity to achieve my goal, and also for your words of encouragement because you have not only been a good supervisor but also a good mentor. To the National Nanosciences Teaching and Traning Center (NNTTP), thanks funding this program. Last but not least to God Almighty, for without you none of this would have been possible. This far you have been with me. May all the glory and honour be rendered to you.

.

Ebenezer

TABLE OF CONTENTS

ABSTRACT ii

KEYWORDS iii

DECLARATION iv

DEDICATION v

ACKNOWLEDGEMENTS vi

TABLE OF CONTENTS vii

LIST OF FIGURES xi

LIST OF TABLES xiv

LIST OF ABBREVIATIONS AND ACRONYMS xv

CHAPTER 1 : INTRODUCTION 16

1.1 Energy: the World Main Concern 17

1.2 Renewable Energy as an Alternative Source 17

1.3 Research Problems 19

1.4 The Thesis Statement 19

1.5 Rationale & Motivation 20

1.6 Aims and Objectives of the Research 21

1.7 Thesis Structure 21

1.8 Research Framework 23

CHAPTER 2 : LITERATURE REVIEW 24

2.1 Introduction 25

2.1.1 Background 25

2.1.2 Batteries components 26

2.1.2.1 Positive electrode 26

2.1.2.2 Negative electrode 26

2.1.2.3 Electrolyte 27
2.1.2.4 Separator 27
2.2 Lithium-ion Batteries 27
2.2.1 Lithium-ion batteries charge / discharge process 29
2.2.1.1 Charge process 29
2.2.1.2 Discharge process 29
2.3 $LiMn_2O_4$: the Idyllic Cathode Material for Lithium-ion Batteries 30
2.3.1 Characteristics of cathode materials for Lithium–ion batteries 31
2.3.2 Methods used for the synthesis of the spinel $LiMn_2O_4$ 32
2.3.3 The Jahn-Teller Distortion of $LiMn_2O_4$ 33
2.4 Nanotechnology and the Application of Nanomaterials 35
2.4.1 The impacts of nanomaterials in Lithium-ion batteries 35
2.4.1.1 Positive impacts of nanomaterials in lithium-ion batteries 35
2.4.1.2 Negative impacts of nanomaterials in lithium ion batteries 36
2.4.2 Bimetallic nanocomposites 36
2.4.3 Copper and gold nanocomposite 36
2.5 Cathode Material Enhancement through Nanotechnology 39
2.6 Modification of Lithium Manganese Oxide with Cu-Au Nanocomposite to Increase the Electrochemical Performance 39
2.7 $LiMn_2O_4$ Surface Modification through Doping: work done by scientists 40
2.7.1 Bulk doping 40
2.7.1.1 Single-ion doping 40
2.7.1.2 Multiple-ion doping 40
2.7.2 Surface doping or coating 41
2.8 Electrolytes 42

CHAPTER 3 : EXPERIMENTAL SECTION AND CHARACTERIZATION TECHNIQUES 44

3.1 Introduction 45

3.1.1 Reagents and materials 45

3.1.2 Powder of preparation nanoparticles $LiMn_2O_4$ cathode material 45

3.1.3 Preparation of copper-gold nanocomposite 45

3.1.4 Synthesis of $LiM_xMn_{2-x}O_4$ 46

3.1.5 Preparation of glassy carbon electrode (GCE) with $LiMn_2O_4$ and novel $LiM_xMn_{2-X}O_4$ 46

3.2 Characterization techniques 47

3.2.1 Crystal Structure Analyses, Morphological and Structural Analysis Techniques 47

3.2.1.1 High resolution scanning electron microscopy (HRSEM) 47

3.2.1.2 High resolution transmission electron microscopy (HRTEM) 48

3.2.1.3 Uv-visible spectroscopy 49

3.2.1.4 X-ray diffraction (XRD) 50

3.2.1.5 Fourier-transform infrared spectroscopy (FT-IR) 51

3.2.2 Electrochemical Techniques 52

3.2.2.1 Cyclic voltammetry (CV) 53

3.2.2.2 Electrochemical impedance spectroscopy (EIS) 56

CHAPTER 4 : RESULTS AND DISCUSSIONS OF $LiMn_2O_4$ AND Cu-Au NANOCOMPOSITE 59

4.1 Crystal Structure Analyses, Structural Analysis and Electrochemical Characterization of $LiMn_2O_4$ Spinel 60

4.1.1 Thermal gravimetric analysis (TGA) 60

4.1.2 High resolution scanning electron microscopy (HRSEM) 61

4.1.3 X-Ray Diffraction (XRD) 65

4.1.4 Fourier-transform infra-red (FTIR) of $LiMn_2O_4$ 68

4.2 Cyclic Voltammetry of Nanoparticles $LiMn_2O_4$ 69

4.2.1 The choice of electrolyte 69

4.2.2 The effect on cyclic voltammetry using 1 M Li_2SO_4 as electrolyte 72

4.3 Morphological Analysis of Cu-Au Nanocomposite 74

4.3.1 Absoption analysis of Cu-Au nanocomposite by Uv-visible spectrocopy . 74

4.3.2 High resolution transmission tlectron microscopy (HRTEM) 76

CHAPTER 5 : CHARACTERIZATION OF A NOVEL METALLIC LAYER Cu-Au NANOCOMPOSITE DOPED-$LiMn_2O_4$ 80

5.1 Morphological Analysis and Electrochemical Characterization of a Novel Metallic Layer of Cu-Au Nanocomposite Doped $LiMn_2O_4$ 81

5.1.1 High resolution scanning electron microscopy (HRSEM) 81

5.1.2 High resolution transmission electron microscopy (HRTEM) 85

5.1.3 X-ray diffraction (XRD) 89

5.1.4 Fourier-transform infra-red (FTIR) 90

5.2 Electrochemical Characterization of Novel Metallic layer of Cu-Au nanocomposite doped- $LiMn_2O_4$ 91

5.2.1 The effects of electrochemical parameters obtained from the CV of $LiMn_2O_4$ and $LiM_xMn_{2-x}O_4$ at 9 mV / s in 1 M Li_2SO_4 91

5.2.2 Redox reaction analysis 93

5.2.3 Electrochemical impedance spectroscopy (EIS) 97

CHAPTER 6 : CONCLUSION AND RECOMMENDATIONS 102

6.1 Conclusion 103

6.2 Recommendations 105

REFERENCES 106

LIST OF FIGURES

Figure 1: Conceptual diagram of this thesis..... **Error! Bookmark not defined.**

Figure 2.1: Ragone plot showing ifferent energy storage systems and their relative power and energy (Van den Bossche *et al*., 2006) 26

Figure 2.2: Li-ion battery (Meng and Arroyo-de Dompablo, 2009) 28

Figure 2.3: Schematic representation for the charge / discharge process of Lithium-ion batteries (Bazito and Torresi, 2006) 29

Figure 2.4: Structure of $LiMn_2O_4$ showing a cubic close-packing arrangement of oxygen ion at the 32e site, the lithium ion at the tetrahedral 8a site while the Mn^{3+} / Mn^{4+} ions reside at the 16d sites. 31

Figure 2.5: Energy splitting of the 3d electron states in an octahedral crystal field (Mn^{4+}) and the Jahn-Teller effect (Mn^{3+}) (Abela et al., 2009)..... 34

Figure 3.1: X-Ray Diffraction System 51

Figure 3.2: A schematic representation of the major components of the electroanalytical system used for electrochemical analysis 53

Filgure 3.3: A three electrode cell system..... 54

Figure 3.4: An example of a cyclic voltammogram response 54

Figure 3.5: A representation of the Nyquist plot displaying the kinetics parameters 57

Figure 3.6: A representation of Bode plot showing variation of impedance and phase angle with changes in frequency 57

Figure 3.7: An equivalent Randles circuit in series (Macdonald, 2006) 58

Figure 4.1: TGA curves of the as-synthesized $LiMn_2O_4$ calcined at 800 ^oC (a), 860 ^oC (b) and 880 $^o C$ (c), recorded at a heating rate of 10 °C min^{-1}..... 61

Figure 4.2: High resolution scanning electron microscopy of $LiMn_2O_4$ calcined at 880 ^oC for 15 h. 63

Figure 4.3: HRSEM Energy dispersive X-ray (EDX) of a selected area of pristine $LiMn_2O_4$ on a Nickel grid 64

Figure 4.4 XRD of $LiMn_2O_4$ precursor at (a) 400 ^oC, (b) 600 ^oC and (c) 800 ^oC with some impurities present represented by the asterisks sign (*: Mn_2O_3)..... 66

Figure 4.5: XRD pattern $LiMn_2O_4$ treated with 2 M H_2SO_4 then heated at (a) 400^oC, (b) 600 ^oC, (c) 700 ^oC, (d) 800 ^oC, (e) 860 ^oC (f) 880 ^oC for 15 h..... 67

Figure 4.6: FTIR spectra for $LiMn_2O_4$..... 68

Figure 4.7: Cyclic Voltammograms of $LiMn_2O_4$/GCE in 0.1 M $LiClO_4$ at different scan rates 69

Figure 4.8: Cyclic voltammograms of $LiMn_2O_4$ / GCE in 1 M $LiClO_4$ at different scan rates 70

Figure 4.9: Cyclic Voltammograms of $LiMn_2O_4$/GCE in 1 M $LiNO_3$ at different scan rates 70

Figure 4.10: Cyclic Voltammograms of $LiMn_2O_4$/GCE in 1 M Li_2SO_4 at different scan rates 71

Figure 4.11: Cyclic Voltammograms of $LiMn_2O_4$/GCE in 1 M Li_2SO_4 at increasing scan rates..... 72

Figure 4.12: A graph of peak current Vs square root of scan rate of $LiMn_2O_4$.. 73

Figure 4.13: Uv-visible of Cu-Au nanocomposite with Au nanoparticles (in set) 75

Figure 4.14: Energy diagram of Cu-Au nanocomposite..... 75

Figure 4.15: HRTEM of Cu-Au nanocomposite..... 77

Figure 4.16: SAED (a) and lattice image (b) of Cu-Au nanocomposite..... 78

Figure 4.17: HRTEM Energy dispersive X-ray (EDX) of Cu-Au nanocomposite on a Nickel grid. 79

Figure 5.1: HRSEM images of doped $Li[Cu\text{-}Au]_{0.02}Mn_{1.98}O_4$ with HRSEM of pristine $LiMn_2O_4$ (inset) 82

Figure 5.2: HRSEM Energy-dispersive X-ray (EDX) of a selected area of $Li[Cu\text{-}Au]_{0.02}Mn_{1.98}O_4$ on a nickel grid with EDX of pristine $LiMn_2O_4$ (inset)..... 83

Figure 5.3: Map of a selected area of $Li[Cu\text{-}Au]_{0.02}Mn_{1.98}O_4$..... 84

Figure 5.4: HRTEM of $Li[Cu\text{-}Au]_{0.02}Mn_{1.98}O_4$ with HRTEM of Cu-Au nanocomposite (inset) 86

Figure 5.5: SAED of a selected area of $Li[Cu\text{-}Au]_{0.02}Mn_{1.98}O_4$ 87

Figure 5.6: HRTEM Energy-dispersive X-ray (EDX) of $Li[Cu\text{-}Au]_{0.02}Mn_{1.98}O_4$ 88

Figure 5.7: XRD pattern of $Li[Cu\text{-}Au]_{0.02}Mn_{1.98}O_4$ calcined at 880^oC for 15 h with an increase in peak intensity. 89

Figure 5.8: FTIR spectra for $LiMn_2O_4$ and $Li[Cu\text{-}Au]_{0.02}Mn_{1.98}O_4$ 90

Figure 5.9: Cyclic voltammogram of $LiMn_2O_4$/GCE 1 M Li_2SO_4 92

Figure 5.10. Cyclic voltammogram of $Li[Cu\text{-}Au]_{0.02}Mn_{1.98}O_4$/GCE in 1 M Li_2SO_4 92

Figure 5.11: Cyclic Voltammograms of $Li[Cu\text{-}Au]_{0.02}Mn_{1.98}O_4$/GCE in 1 M Li_2SO_4 at different scan rate. 93

Figure 5.12: Cyclic voltammograms of $LiMn_2O_4$/GCE and $Li[Cu\text{-}Au]_{0.02}Mn_{1.98}O_4$/GCE in 1 M Li_2SO_4 at 9 mV / s 95

Figure 5.13: Nyquist plot of $LiMn_2O_4$ (a) and $Li[Cu\text{-}Au]_{0.02}Mn_{1.98}O_4$ with perturbation amplitude of 9 mV / s 98

Figure 5.14: The model circuit obtained for $LiMn_2O_4$ and $Li[Cu\text{-}Au]_{0.02}Mn_{1.98}O_4$ 98

Figure 5.15: The Bode plot of $LiMn_2O_4$ (a) and $Li[Cu\text{-}Au]_{0.02}Mn_{1.98}O_4$ (b) with perturbation amplitude of 10 mV 101

LIST OF TABLES

Table 1: Different cathode materials used in LIBs (Doeff, 2013) 32

Table 2: Different methods for synthesizing nanocomposites 38

Table 3: Peak current of $LiMn_2O_4$ versus square root of scan rate 73

Table 4: Electrochemical parameters from CV for $LiMn_2O_4$ and $Li[Cu\text{-}Au]_{0.02}Mn_{1.98}O_4$ 91

Table 5: The obtained values of Charge / Discharge capacity 96

Table 6: Kinetics parameters of $LiMn_2O_4$ and $LiM_xMn_{2-x}O_4$ obtained from electrochemical impedance spectroscopy at 298 K 99

LIST OF ABBREVIATIONS AND ACRONYMS

LIB	Lithium-ion battery
C	Speed of light
CV	Cyclic voltammetry
C_{dl}	Double layer capacitance
EIS	Electrochemical impedance
E_g	Energy band gap
GCE	Glassy carbon electrode
h	Planck's constant
HRTEM	High resolution electron microscopy
HRSEM	High resolution scanning electron microscopy
I_p	Peak current
I_{pa}	Anodic peak current
I_{pc}	Cathodic peak current
K_{et}	Rate constant of electron transfer
$LiMn_2O_4$	Lithium manganese oxide spinel
M_x	$[Cu –Au\ nanocomposite]_x$
R_{ct}	Charge transfer resistance diffraction
XRD	X-ray diffraction
D	Diffusion coefficient
ΔE_p	Change in potential
λ	Wavelength
η	Coulombic efficiency
τ	Time constant
SAED	Selected area electron diffraction
JCPDS	Joint committee of power diffraction standards
HOMO	Highest occupied molecular orbital
LUMO	Lowest unoccupied molecular orbital

CHAPTER 1 : INTRODUCTION

1.1 Energy: the World Main Concern

For the past few years, energy deficiencies as well as environmental pollution have become the world main concern due to the economic development and the increase in the world population. Energy plays an important role in everyday life since the beginning of civilization. However, the used sources of energy were non-renewable. Non-renewable energy sources such as fossil fuels which are regarded as resources of economic value which cannot be voluntarily replaced by natural ways on a level equal to its demand. Oil, natural gas and coal are the mainly used non-renewable energy sources. One of their advantages is that they are widely available and affordable. Two different models were used to calculate the exhaustion time of these non-renewable energy sources. On one hand, using Klass model, the depletion time found for oil, coal and gas was approximately 34, 106 and 36 years respectively. On the other hand, with the New model the depletion time for oil coal and gas obtained was 35, 107 and 37 respectively. Consequently, from the obtained new values it can be concluded that coal will remain the only available non-renewable energy sources until 2112 (Shafiee and Topal, 2009). Moreover, the by-products and mining of these fossil fuels contribute significantly to the pollution of our environment. Arguably, it came to the attention of the world that these non-renewable sources of energy would be exhausted earlier than predicted.

1.2 Renewable Energy as an Alternative Source

As result of the energy sources problems, renewable energy sources such as solar cells and wind energy have gained one of the attentions. Nevertheless, during the course of the year depending on the season the demand of these renewable energy sources increases. Because of these facts, the permanence of these powers source is unstable. Hence the search to a more convenient, environmental friendly, cost effective, as well as safe energy source is on the rise. Energy storage systems with good response from the recurrent fluctuations of the power sources could be the right choice. LIBs are the most suitable solution. LIBs have high volume energy density and are able to provide up to 1,5 times in weight energy density than batteries such as Nickel metal hydride. LIBs have a nominal voltage of (3.7 V) which is more than three times than that of Nickel metal hydride (1.2 V) and Nickel-cadmium battery. The development of cost-effective, long-lasting and abuse tolerant LIBs are being widely used because of their high energy density and good cycle life which have led them to become the

most prevalent alternative for electronic devices. Nanotubes, nanostructured bimetallic alloys, nano-oxides and nanocomposites as electrode materials may solve the volume expansion problem, avoid the high irreversible capacity and improve the electrochemical properties for the next generation of lithium rechargeable batteries. The electrochemical performance of the cathode material as part of the battery depends on the particles properties such as morphology, specific surface area, crystallinity and composition hence it is an essential part in the battery. There are different cathodes materials with good electrochemical performance, low cost as well as high stability that are investigated such as $LiNiO_2$ (Nagaura and Tozawa, 1990) and $LiCoO_2$ (Dahn *et al*., 1994) with layer of (R3m) structure, $LiNiVO_4$ and $LiCoVO_4$ (Fey *et al*., 1997) with spinel (Fd3m) structure and $LiMn_2O_4$ (Chang *et al*., 1999) with spinel (Fd3m) structure. However, $LiMn_2O_4$ has become the most promising cathode material above all since it offers lower cost, environmental friendliness, no toxicity and a better safety properties.

Spinel $LixMn_2O_4$ mainly exhibits two voltage plateaus, 4 V for $0 < x < 1$ and 3 V for $1 < x < 2$. Even though the cycling performance of spinel $LiMn_2O_4$ electrode is far better in the 4 V range than 3 V range, it shows considerable capacity fading in the 4 V range also, on long-term cycling. This capacity fading of the material has been attributed to several factors, such as: (1) the Jahn–Teller distortion caused by Mn^{3+} would lead to the degradation of cyclability in $LiMn_2O_4$ during the Li^+ intercalation and de-intercalation (Robertson *et al*., 1997), (2) dissolution of manganese into the electrolyte and decomposition of the electrolyte (Xia and Yoshio, 1997), (3) cation mixing between Li and Mn ion in the spinel lattice (Chan *et al*., 2003a) (4) oxygen loss from the spinel lattice (Yang *et al*., 2003) and (5) break down of the spinel lattice (Xia and Yoshio, 1997).

For the past few years, many have tried to improve $LiMn_2O_4$ through doping using diverse elements improve the electrochemical performance. For example, the non-metals such as B (Thirunakaran *et a*l., 2004, Chan *et al*., 2006, Liu *et al*., 2013), Br (Du *et al*., 2011), the general metals such as, Ti (Liu *et al*., 2007b), Fe (Liu *et al*., 2013), Ni (Wu *et al*., 2007), Cu (Ein-Eli *et al*., 2005), Ga (Liu *et al*., 2007a) Ag (Son *et al*., 2004, Tay and Johan, 2010), Au (Tu *et al*., 2006) the rare-earth metals La (Sun *et al*., 2012), Ce (Ha *et al*., 2007) . On the other hand, other researchers have also modified $LiMn_2O_4$ by surface coating (Li and Xu, 2008, Shi *et al*., 2010, Wang and Sun, 2012), laser annealing (Pröll *et al*., 2011), pulsed laser deposition (Yunjian *et al*., 2009). Among all these methods, doping method shows improved electrochemical performance as it can weaken the Jahn-Teller effect and improve the stability

of the structure. The increased stability of the structure and the weakened Jahn-Teller effect can both participate in the improvement of the cycle performance.

This research focus was aimed on doping the $LiMn_2O_4$ with small amount of Cu-Au nanocomposite cations for substituting the Mn^{3+} in order to prolong the life time of the cathode and improve the electrochemical performance of the cathode material

1.3 Research Problems

Due to their characteristics such as high energy and power densities, lithium-ion batteries have become the most important type of energy storage. Lithium-ion batteries find their use in electrics vehicles (EVs), portable devices. Moreover batteries are also needed in the automotive industry to reduce our consumption of oil as well as to make more environmentally friendly vehicles (Dresselhaus *et al*., 2001, Yang *et al*., 2011, Tarascon and Armand, 2001). $LiMn_2O_4$ as cathode material plays a crucial role in to the electrochemical performance of lithium-ion batteries. However, the disadvantage is that spinel $LiMn_2O_4$ suffers from severe capacity fading, especially at higher temperature (55 °C) during discharging / charging. This limits its cycle ability and does not allow its commercialization (Liang *et al*., 2008). But, because of their cost effective as well as their environmental friendliness $LiMn_2O_4$ spinel systems have become the most promising cathode materials for electrical vehicles (EV) and industrial use. In order for rechargeable battery to be commercialized, it has to be based on intercalation of compound. This leads to a search into improving the properties of the spinel $LiMn_2O_4$ cathode material. But, how can this be solved? Has become one of the focal concerns. Therefore, this MSc research work proposes a new dopant namely: Cu-Au nanocomposite that is used in the surface modification of $LiMn_2O_4$, with the expectation of improving the electrochemical performance which is investigated using cyclic voltammetry (CV) and electrochemical impedance (EIS).

1.4 The Thesis Statement

This study makes use of copper and gold as bimetallic transitions metal nanocomposite as doping materials, for the enhancement of the electrochemical performances of $LiMn_2O_4$ spinel system. The properties of copper and gold nanocomposite and $LiMn_2O_4$ are expected to improve the life cycle of the batteries at high electrode capacity as well as the charge / discharge capacity. The MSc. Research study was done based on the following questions:

1) Why the choice of $LiMn_2O_4$ as cathode materials amongst all others?

2) How will doping of nanocomposite affect the electrochemical performance of $LiM_xMn_{2-x}O_4$?

3) Does the pristine $LiMn_2O_4$ contribute to the battery performance?

4) What will the rate determining step in the lithium elimination / addition in the modified $LiM_xMn_{2-x}O_2$ be?

1.5 Rationale & Motivation

Deintercalation of Li from a transition metal oxide (cathode) causes the material's lattice to contract. Extraction of all, or even 80-90%, of the Li-ions would change the structure so much that the electrode would fail after a small number of charge / discharge cycles. In practice, batteries are as a rule designed so that only about half of the Li-ions are ever deintercalated from the cathode. The gravimetric capacities of cathode materials are thus limited to 120-160 mAh / g. Anode materials, in contrast, have gravimetric capacities of 372 mAh / g or more. The capacity difference between anode and cathode materials means that the cathode in LIBs must be several times more massive than the anode. It is thus particularly important to develop cathode materials with higher capacities. To achieve this objective, both the energy density and the current density require significant improvement. The current density is in particular determined by the Li-ion diffusion through the electrode materials. The performance of current energy storage devices still require higher energy and power densities, faster recharge rates and longer charge-discharge cycle lifetimes. The energy output of LIBs's depends on both the operating voltage (determined by redox reaction), and the charge storage capacities of the electrode materials. When a battery is discharged rapidly to provide high power, overpotential is needed to drive the electrode reaction at sufficiently fast rates, which decreases the operating voltage and the energy.

The capacity fades mainly due to the following three factors:

Dissolution of Mn^{3+}. After cycling or storage, the surface of LiMnO is rich in Mn^{3+}, contrary to the bulk structure. The Mn^{3+} at the surface may disproportionate, and Mn^{2+}-ions may dissolve in the electrolyte solutions (Jang *et al*., 1996).

Jahn-Teller effect. At the end of discharge, distortion causes $Li_{1-x}[Mn_{2-x}]O_4$ structure destruction to form a tetragonal structure, which is low in symmetry and high in disorder.

This local distortion is related to the vacancy / occupancy of the e.g. antibonding orbital of the Mn^{3+} ionizing successive charge and discharge cycles, respectively (Goodenough, 1998).
In organic solvents, the de-lithiated particles are not stable at the end of discharge; the high oxidation ability of Mn^{4+} will lead to decomposition of the solvent (Benbow *et al*., 2011).

1.6 Aims and Objectives of the Research

The aim towards improving Li-ion battery cathode performance includes the following facets that are economical and benign to human health and environment:

- Synthesis of $LiMn_2O_4$ cathode materials using cost-effective and nontoxic precursors.
- Increasing life cycle and performance (decreasing internal resistance and increasing output power) by changing the composition of the material used in the cathode; use of relatively few numbers of reagents.
- Increasing the surface area of the electrodes.
- Improving capacity by improving the structure, to incorporate more active materials.
- Improving the safety of Lithium-ion batteries.

The objectives were the following:

- To synthesize $LiMn_2O_4$ cathode material via co-precipitation method
- To synthesize Cu-Au nanocomposite via chemical reduction method
- To dope $LiMn_2O_4$ cathode materials with the synthesized Cu-Au nanocomposite
- To characterize the synthesized cathode materials via, thermal gravimetric analysis (TGA), high resolution scanning electron microscopy (HRSEM), high resolution transmission electron microscopy (HRTEM), ultraviolet-visible spectroscopy (Uv - vis), x-ray diffraction (XRD), fourier-transform infra-red (FTIR) cyclic-voltammetry (CV), electrochemical impedance spectroscopy (EIS)
- To study the electrochemical properties of the cathode materials.

1.7 Thesis Structure

This thesis comprises six (6) chapters and is structured as follows:

Chapter one

This chapter gives us an introduction of different cathode materials used for Li-ion batteries but mostly focussed on $LiMn_2O_4$ as well as the different dopants such as nanomaterial that have been done to improve its electrochemical performance. The aim and objectives are also stated in this chapter.

Chapter two

This chapter gives a literature review relating to the definition of Li-ion batteries, its main components. A better understanding of $LiMn_2O_4$ as well as nanomaterial will be presents in this section.

Chapter three

The method used for the synthesis of $LiMn_2O_4$, Cu-Au nanocomposite, Cu-Au nanocomposite-doped $LiMn_2O_4$ as well as the instrumentations and characterization used are fully detailed in this section.

Chapter four

The results found for the synthesized $LiMn_2O_4$, Cu-Au nanocomposite doped $LiMn_2O_4$ are presented and discussed in this chapter.

Chapter five

This section displays the results and discussion obtained for the novel $LiM_xMn_{2-x}O_4$

Chapter six

Finally this chapter will present the conclusion as well as recommendations.

Reference

This section is ascribed to the references that were used for this thesis.

1.8 Research Framework

For the achievement of this MSc research, the following steps had to be followed:

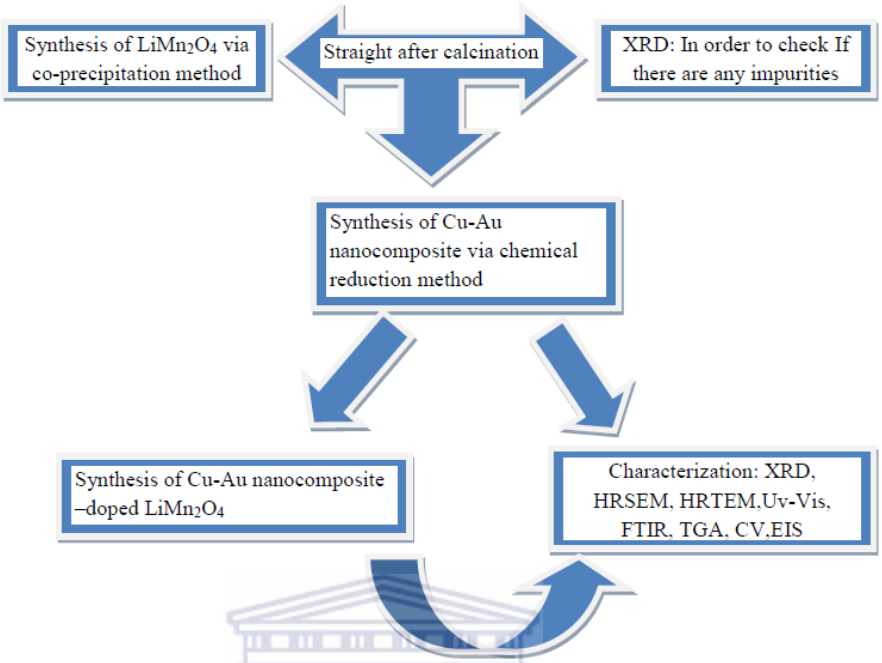

Figure 1: Conceptual diagram of this thesis

CHAPTER 2 : LITERATURE REVIEW

2.1 Introduction

2.1.1 Background

Batteries can be regarded as unit cells containing chemical energy that can be converted into electrical energy (Husain, 2011). These cells are bounded in a case to form a battery unit. A battery pack is then defined as an assembly of these separate battery units that are connected in a series and parallel grouping to deliver the expected voltage and energy to the power storage system. The stored energy in a battery is the difference in free energy between chemical components in the charged and discharged states. This available chemical energy in a cell is converted into electrical energy only on demand, using the basic components of a unit cell. The electrochemically active constituent of the positive or negative electrode is called the active material. The redox reaction takes place at the two electrodes, resulting in a bonding and releasing of electrons. The electrodes have to be electronically conducting and they are positioned at diverse sites, a separator plays the role of splitting them. Throughout battery process, electrons flow from one electrode to another. Nevertheless, this flow of electrons in the cell is maintainable only if electrons that are generated during the chemical reaction are capable to pass through an external electrical circuit that links those two electrodes. The battery terminals are regarded as joining points among the two electrodes and the external circuit. On the other hand, external circuit make sure that most of the chemical energy that is stored is released only on demand and is used as electrical energy. Batteries are divided into two different types: primary batteries defined as those that cannot be recharged for examples lithium batteries used in clocks, cameras etc. The other type is secondary batteries; these are rechargeable and can be reuse. The examples of these rechargeable batteries are: Lead-acid, Nickel-cadmium, Lithium-ion, Zinc-air, Lithium-polymer, Sodium-sulphur batteries. Figure 2.1 is a representation of Ragone plot showing different energy devices and their relative power and energy.

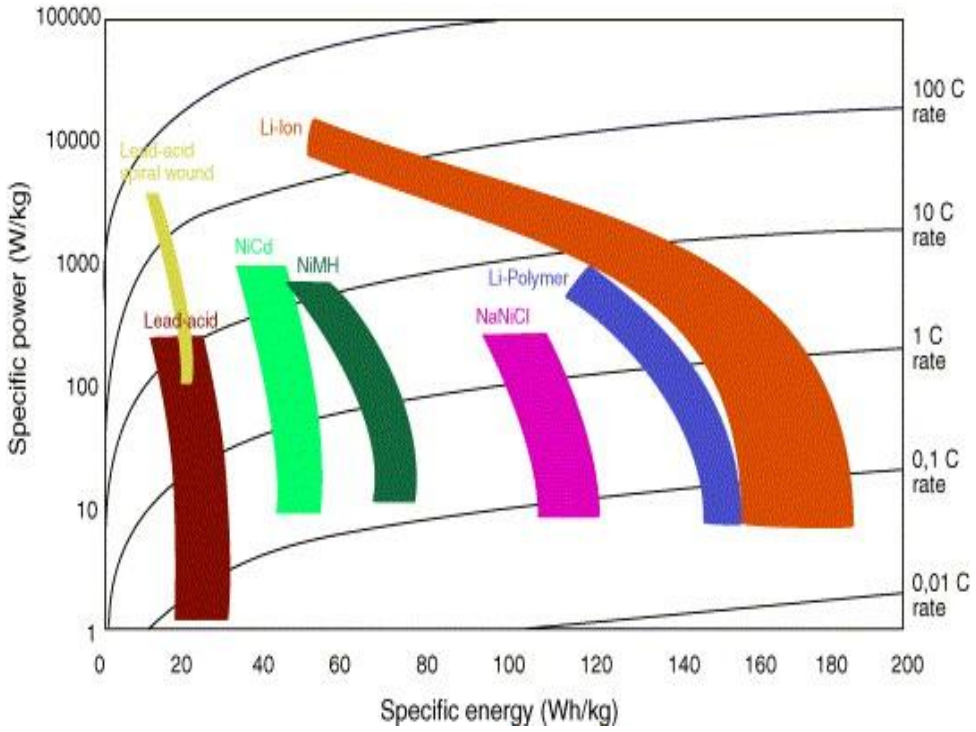

Figure 2.1: Ragone plot showing different energy storage systems and their relative power and energy (Van den Bossche *et al*., 2006)

2.1.2 Batteries components

2.1.2.1 Positive electrode

The positive electrode can be defined as an oxide or sulphide or some other compound that can easily be reduced through cell discharge. This electrode consumes electrons from the external circuit during cell discharge. Examples of positive electrodes are lead oxide (PbO_2) and nickel oxyhydroxide (NiOOH). The electrode materials are in the solid state (Husain, 2011).

2.1.2.2 Negative electrode

The negative electrode is a metal or an alloy that is adept of being oxidized through cell discharge. This electrode generates electrons in the external circuit during cell discharge. Examples of negative electrodes are lead (Pb) and cadmium (Cd). Negative electrode materials are also in the solid state within the battery cell (Husain, 2011).

2.1.2.3 Electrolyte

The electrolyte is the medium that allows the conduction of ions between the positive and negative electrode of a cell. The electrolyte must have high and selective conductivity for the ions that take part in electrode reactions, but it must be a non-conductor for electrons in order to avoid self-discharge of batteries. The electrolyte can either be solid material, liquid or gel. In addition the electrolyte can be acidic or alkaline, depending on the type of battery. Traditional batteries such as lead-acid and nickel-cadmium use liquid electrolytes. In lead-acid batteries, the electrolyte is the aqueous solution of sulphuric acid [H_2SO_4(aq)]. Advanced batteries currently under development for EVs, such as sealed lead-acid, nickel-metal-hydride (NiMH), and lithium-ion batteries utilizes an electrolyte that can either be gel, paste or resin. Lithium-polymer batteries use a solid electrolyte (Husain, 2011).

2.1.2.4 Separator

The separator can be regarded as an electrically insulating layer of material that is able to essentially separate electrodes of opposite polarity. Separator has to allow the flow of ions of the electrolyte and may also play the role of storing or allow the electrode to immobilize easily (Husain, 2011).

2.2 Lithium-ion Batteries

Lithium as a metal is known to have a high electrochemical reduction potential (3.045 V) and the lowest atomic mass (6.94), which shows promise for a battery of 3 V cell potential when combined with a suitable positive electrode. The interest towards secondary lithium cells soared soon after the arrival of lithium primary cells in the 1970s, although the main challenge was the highly reactive nature of the lithium metal with moisture, restricting the use of liquid electrolytes. But late in the 1970s, it was revealed by researchers at Oxford University that lithium can be intercalated (absorbed) into the crystal lattice of cobalt or nickel to form $LiCoO_2$ or $LiNiO_2$ tiled the way toward the development of Li-ion batteries (Husain, 2011). The use of metallic-lithium is bypassed in Li-ion batteries by using lithium intercalated (absorbed) carbons (Li_xC) in the form of graphite or coke as the negative electrode, alongside with the lithium metallic oxides as the positive electrode. The graphite has the capacity of hosting lithium up to a composition of LiC_6. Most of Li-ion batteries make

use of cobalt as positive electrode, though it is expensive but has proven to be the most adequate. Other alternative positive electrode such as nickel oxide $LiNiO_2$, is known to have a complex structure and is cost effective. Although, $LiNiO_2$ has the similar performance to lithium oxide electrodes. Another positive electrodes is known as manganese oxide based ($LiMn_2O_4$ or $LiMnO_2$) which are also under investigation, because manganese is less toxic, cheaper, and broadly available (Doeff, 2013). Figure 2.2 displayed below is a representation of a Li-ion battery.

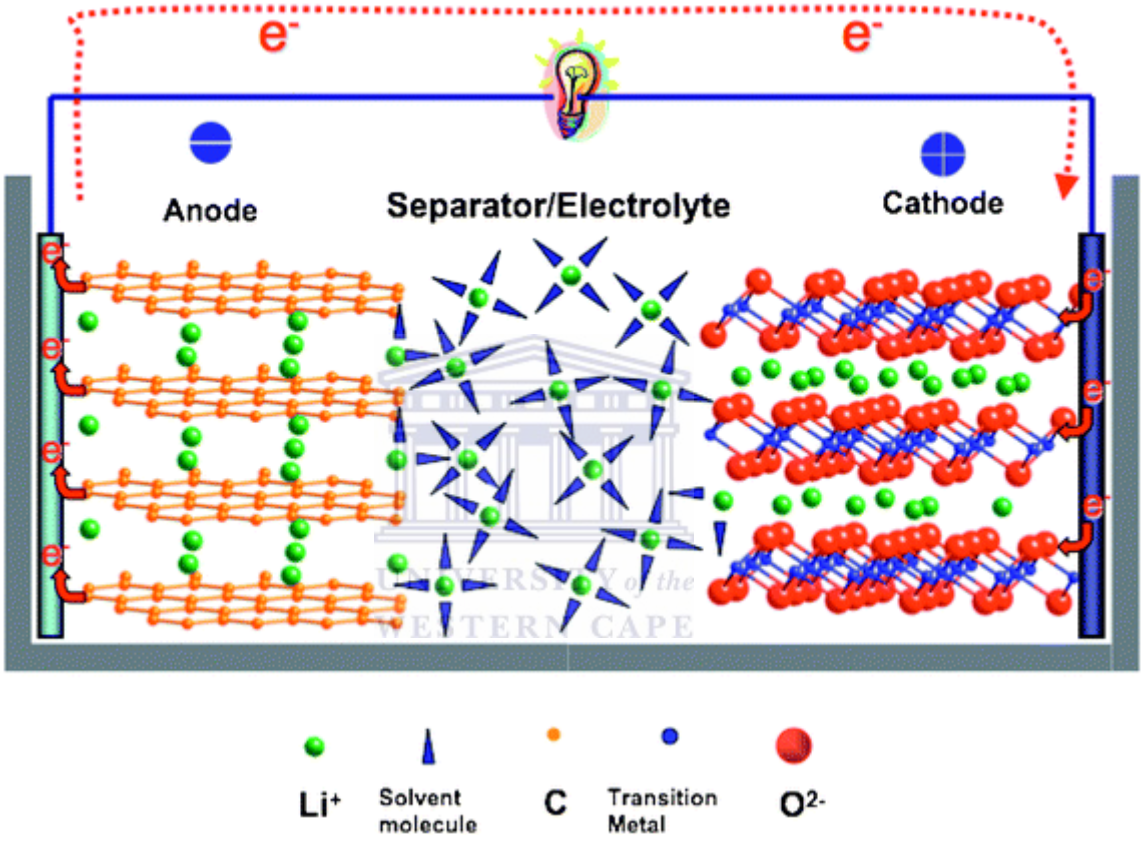

Figure 2.2: Li-ion battery (Meng and Arroyo-de Dompablo, 2009)

2.2.1 Lithium-ion batteries charge / discharge process

The charge / discharge process is illustrated below:

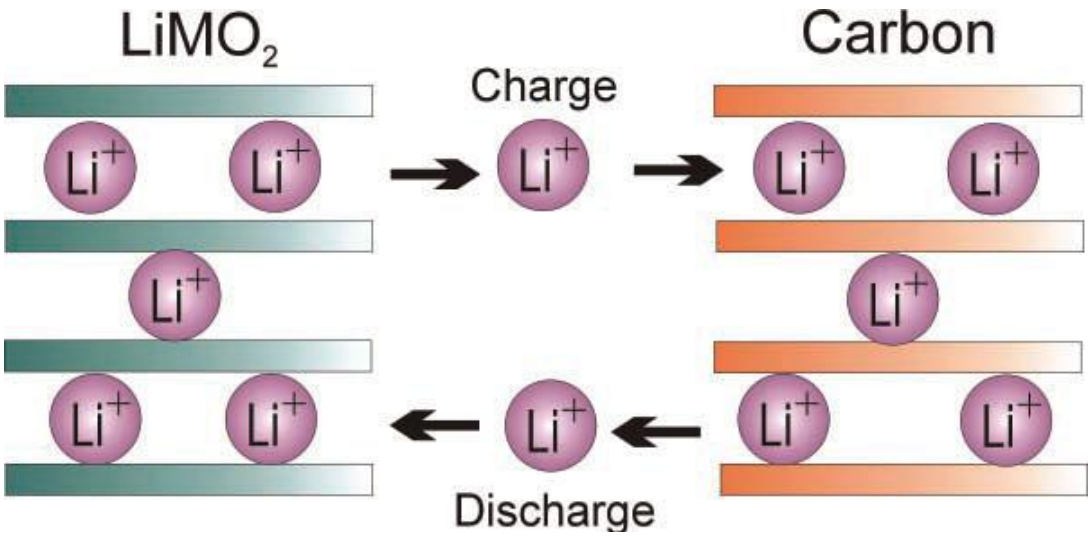

Figure 2.3: Schematic representation for the charge / discharge process of Lithium-ion batteries (Bazito and Torresi, 2006)

2.2.1.1 Charge process

During cell charge, lithium ions move in the opposite direction from the positive electrode to the negative electrode. The nominal cell voltage for a Li-ion battery is 3.6 V, which is equivalent to three NiMH or NiCd battery cells.

2.2.1.2 Discharge process

During cell discharge, lithium ions (Li^+) are released from the negative electrode that travels through an organic electrolyte toward the positive electrode. In the positive electrode, the lithium ions are quickly incorporated into the lithium compound material. The process is completely reversible.

2.3 $LiMn_2O_4$: the Idyllic Cathode Material for Lithium-ion Batteries

The $LiMn_2O_4$ cathode material is known to form (Fd3m) as spinel structure, in which manganese occupies the octahedral sites and lithium predominantly occupies the tetrahedral sites (Thackeray *et al*., 1993). Moreover Li^+ ions reside in the 8a tetrahedral sites then manganese resides in the octahedral (16d) site and the other octahedral site (16c) is empty. During Li^+ diffusion within the spinel structure, Li^+ ion firstly moves from the 8a site to the neighbour empty octahedral 16c site, after that to the next 8a site in such a way that the Li^+ ion takes the diffusion path (8a-16c-8a). The $LiMn_2O_4$ is known to have the following empirical formula: AB_2X_4, where A cations reside on the 8a tetrahedral sites, B cations reside on the 16d octahedral sites and the X cations reside on the 32e sites in a ccp (cubic close-packing) array as shown on Figure 2.4 lithium is in 8a tetrahedral sites, thus can be reversibly extracted, leading to the transformation of $LiMn_2O_4$ to λ-MnO_2.Moreover, the spinel $LiMn_2O_4$ is changed to tetragonal $Li_2Mn_2O_4$ when there are more lithium ions inserted into the 16c site at 2.8V. The overall electrochemical reaction is written as follow (Xia, 2008, Rossouw *et al*., 1990).

$$\underset{\text{Cubic}}{\lambda\text{-}MnO_2} + Li^+ + e \underset{Discharge}{\overset{Charge}{\rightleftarrows}} \underset{\text{Cubic}}{LiMn_2O_4} \underset{Discharge}{\overset{Charge}{\rightleftarrows}} \underset{\text{Tetragonal}}{Li_2Mn_2O_4\text{-}Li^+\text{-}e} \qquad (1)$$

(Eichinger and Besenhard, 1976)

In this case, the paths for lithiation and delithiation are a 3-dimensional network of channels rather than planes. This three-dimensional spinel structure leads to the improvement of the ion flow (Zhu *et al*., 2008) among the electrodes which lowers the internal resistance and increases the loading capability. The use of the spinel $LiMn_2O_4$ as cathode material in lithium ion batteries also presents advantages such as: manganese abundance, non-toxicity, low-cost, and possibility of insertion of lithium ions per unit formula. This last aspect is very appealing due to the fact that lithium-ion batteries is able to function at both 3 and 4V vs. Li / Li^+ (Thackeray, 1995). Lithium ions can be extracted from $LiMn_2O_4$ to form the λ-MnO_2 phase, while still remaining in its cubic symmetry structure (Hunter, 1981). Thus, even a small external perturbation to $LiMn_2O_4$ spinel, such as a small amount of Li^+ insertion or λ-MnO_2 extraction, leads to the reaction of high pin Mn^{3+} ions with accompanying Jahn-Teller distortion.

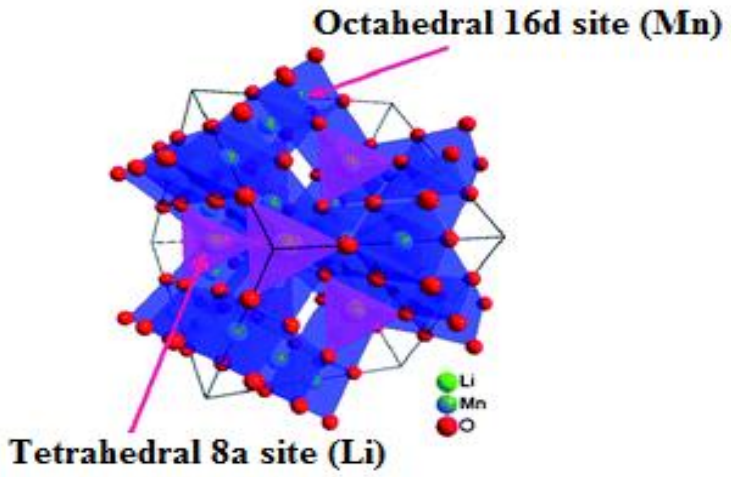

Figure 2.4: Structure of $LiMn_2O_4$ showing a cubic close-packing arrangement of oxygen ion at the 32e site, the lithium ion at the tetrahedral 8a site while the Mn^{3+} / Mn^{4+} ions reside at the 16d sites.

2.3.1 Characteristics of cathode materials for Lithium–ion batteries

Different cathode materials have been used in the making of the lithium ions batteries, among which $LiCoO_2$ is found to be the most currently commercialized cathode material but cannot meet the requirement of large scale demands due to its low energy density of 150 wh kg^{-1}, high cost, safety concern as well as toxicity. However the principal characteristics for the cathode material are as follow:

High discharge voltage: The charge reaction should have a large negative free energy: high discharge voltage.

High energy density: The host structure must have a low molecular weight and the ability to intercalate a large amount of lithium.

High power density: The host structure should have a high chemical diffusion coefficient.

Long cycle life: The structural modification during intercalation and deintercalation should be as small as possible.

The material should be chemically stable, nontoxic and inexpensive.

The handling of the material should be easy.

These characteristics make Li-ion batteries being highly suitable for EV and HEV and other applications of rechargeable batteries

Table 1: Different cathode materials used in LIBs (Doeff, 2013)

Cathode Materials	Advantages	Disadvantages
LFP ($LiFePO_4$ and variants)	Moderately low cost	Low operating voltage
	Excellent high rate performance	Low capacity, especially for substituted variants
	No resource limitations	Controlling patents
	Very slow reaction with electrolyte	
	Excellent safety (no oxygen release)	
NMC ($LiNi_1$ / $3Co_1$ / $3Mn_1$ / $3O_2$) and variants	High operating voltage	High cost of Ni and Co
	High capacity	Potential resource limitations
	Slow reaction with electrolytes	Relatively new in performance
	Moderate safety (oxygen release	Controlling patents
NCA ($LiNi_{0.8}Co_{0.15}Al_{0.05}O_2$)	Performance is well established	High cost of Ni and Co
	Slow reaction with electrolytes	
	High capacity	Potential resource limitations
	High voltage	Controlling soft patents
	Excellent high rate performance	
LMO ($LiMn_2O_4$ and variants)	Low cost	Mn solubility issue, affecting cycle life
	Excellent high rate performance	
	High operating voltage	
	No resource limitations	Low capacity
	Moderate safety (oxygen release)	

2.3.2 Methods used for the synthesis of the spinel $LiMn_2O_4$

Most of the methods used in the synthesis of $LiMn_2O_4$ are: sol-gel method, co-precipitation method and hydrothermal method. Compared with the conventional solid-state reactions, the sol-gel method is believed to offer many advantages such as lower temperature processing, better control of material morphology, smaller and more uniform particles (Liu *et al*., 2004, Fergus, 2010, Amdouni *et al*., 2006). Sol-gel method is also one of the most cost-saving and time-effective ways to produce doped metal oxides in large quantities (Balaji *et al*., 2012). Co-precipitation method can make the product smaller in size and thus higher in specific surface which is an important parameter when working with nanomaterials, but with the

disadvantages of instability in electrochemical performance. Although it is easier to control the stoichiometry of lithium manganese oxide by the co-precipitation method (Chan *et al*., 2003b) than by solid state synthesis. On the other hand, the hydrothermal method requires high temperature and high pressure (Yang *et al*., 2003) in order for the synthesis to take place. In this method, the particles obtained are superfine powders and it is easier to generate a lot of nano-scaled metal oxides powder. The particle sizes obtained from the hydrothermal method may vary from numerous nanometers to hundreds of nanometers, which generally are not easy to obtain.

The above discussed synthetic methods show that to improve the cycle performance and decrease capacity fading, a better target product which is uniform, appropriate in size, stable and pure in spinel structure is highly required, so we should choose the appropriate method according to the demands. Based on the above, the choice of co-precipitation method was made for the cathode materials synthesis in this present work.

2.3.3 The Jahn-Teller Distortion of $LiMn_2O_4$

It has been proven that the Mn^{3+} distort at the octahedral site, when the electrons located in the 3d-band of this cation are placed in the high spin of the electronic configuration. Because the high spin cation has four 3d-band electrons, it caused the distortion to occur. As a result of crystal field splitting, the electronic band splits into two main degenerate energy levels. The t_{2g} energy level d_{xy}, d_{xz} and d_{yx} are formed by the 3d electron orbital. Moreover the energy level is higher in the t_{2g} energy level and is composed of two 3d orbital such as d_{x2-y2} and d_{z2}. The electrons located in the t_{2g} orbital do not exhibit any bonding with the oxygen ion on one hand. On the other hand, the eg level is made of two electrons orbital, and these electrons orbital directly face an orbital of the oxide ions. Because the energy levels of these orbitals are degenerated, hence they are called antibonding. And if the rule of Hund is obeyed; orbital must contain its own unique electron. Henceforth the three orbitals of the t_{2g} and the one in the eg orbital in the configuration of high- spin are half filled. If the oxide ions in the z-axis move away from d_{z2} orbital, leading to a more stable d_{z2} orbital, there will be degeneracy of the e_g orbital resulting in a gain of energy. Thus, this movement leads to a distortion of the octahedral site to form an elongated octahedron called the Jahn–Teller distortion (Yamada and Tanaka, 1995). Figure 2.5 represents an illustration of Mn^{3+} in oxygen octehadra.

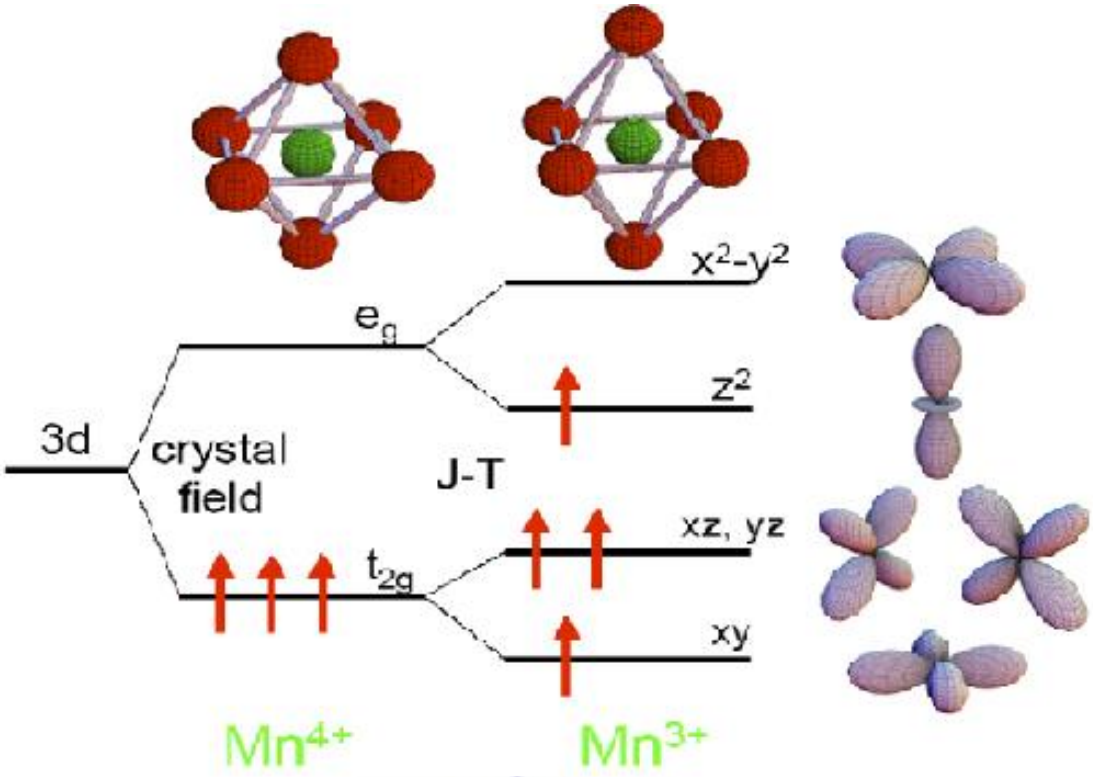

Figure 2.5: Energy splitting of the 3d electron states in an octahedral crystal field (Mn^{4+}) and the Jahn-Teller effect (Mn^{3+}) (Abela et al., 2009)

In the $LiMn_2O_4$ stoichiometry, half of the manganese cations are in the Mn^{3+} oxidation station and the other half are in the Mn^{4+} oxidation state. Surprisingly, below room temperature the stoichiometry of $LiMn_2O_4$ is orthogonal, and at temperature higher than 55 ^oC the stoichiometry of $LiMn_2O_4$ is cubic. Subsequently, the charge ordering of the spinel leads to a phenomenon that gives rise to the Jahn-Teller distortion of the cubic material (Rodriguez-Carvajal *et al*., 1998). Nevertheless, if some of the Mn cations are substituted for Lithium ion, then not half the Mn cation in the $LiMn_2O_4$ spinel will be in the 3+ oxidation state, and the rest of the cation will be in the 4+ oxidation state. It is known that the Mn^{4+} cation, cannot leads to the Jahn-Teller distortion, hence it will not be easier to make structural changes on the substituted $LiMn_2O_4$ below room temperature (Yamada and Tanaka, 1995). $LiM_xM_{2-x}O_4$ cathodes has the ability to higher Mn valence which may be need to suppress the Jahn-Teller distortion and improved of cyclic performances can be expected as well as an increased in the charge / discharge at higher voltage (Okada *et al*., 2000).

2.4 Nanotechnology and the Application of Nanomaterials

Nanotechnology is defined as the design, fabrication and application of nanostructures or nanomaterials, and it plays a crucial role in the understanding of the relationships between physical properties or phenomenon and dimensions of materials. However, some of these properties are still yet to be discovered. For instance, the band gap of semiconductors can be adjusted by fluctuating the dimensions of the materials. Moreover, nanotechnology also deals with materials or structures in nanometer scales, typically ranging from subnanometers to several hundred nanometers (Cao, 2004). One nanometer is 10^{-9} meter. Some of the areas in which this new technology is applied are: structured applications for instance in aerospace and automotive industries, energy conversion, storage and distribution, defence, chemical applications, information processing, storage and transmission and nano-biotechnology

2.4.1 The impacts of nanomaterials in Lithium-ion batteries

The decrease in size compared to bulk material could have positive and negative impacts in lithium-ion batteries.

2.4.1.1 Positive impacts of nanomaterials in lithium-ion batteries

The reduced dimensions increase considerably the rate of lithium insertion / removal, because of the short distances for lithium-ion transport within the particles. The characteristic time constant for diffusion is given by $t = L^2 / D$, where L is the diffusion length and D the diffusion constant and the time t for intercalation (Aricò *et al*., 2005).

Electron transport within the particles is also enhanced by nanometer-sized particles, as described for lithium ions (Aricò *et al*., 2005).

A high surface area permits a high contact area with the electrolyte and hence a high lithium-ion fluxes across the interface.

For very small particles, the chemical potentials for lithium ions and electrons may be modified, resulting in a change of electrode potential (thermodynamics of the reaction) (Balaya *et al*., 2006) .

The composition range over which solid solutions exist is frequently more extensive for nanoparticles and the strain associated with intercalation is often improved (Bruce *et al*., 2008).

2.4.1.2 Negative impacts of nanomaterials in lithium ion batteries

The synthesis of nanoparticles may be difficult, and their dimensions may be tricky to control.

High electrolyte / electrode surface area may lead to extra considerable side reactions with the electrolyte, and make it difficult to maintain the interparticle contact.

- The density of a nanopowder is usually minus than of the same material formed from micrometer-sized particles. The volume of the electrode increases for the same mass of material thus reducing the volumetric energy density (Bruce *et al*., 2008).

2.4.2 Bimetallic nanocomposites

Metal nanoparticles can be alienated into two groups: monometallic or bimetallic. Bimetallic nanoparticles are nanoparticles that are made up of two metal nanoparticles. Their increased in surface area have lead them to have higher catalytic properties compared to their corresponding monometallic nanoparticles (Zhou *et al*., 2006). Bimetallic nanocomposites are obtained as a result of simultaneous reduction of the metal salts to nanoparticles from successive reduction of the more noble metal salt followed by the reduction of the less noble metal salt. Bimetallic nanocomposite are of considerable interest since they possess interesting size depended electrical, chemical and optical properties (Devarajan *et al*., 2004). They are of special importance in the field of catalyst, since they often exhibit better catalytic properties than their monometallic counterparts (Zhou *et al*., 2006).

2.4.3 Copper and gold nanocomposite

Copper and gold as the earliest metal are amongst the first to be known to man. The attractive properties which made copper so useful are: good corrosion resistance, attractive colour, excellent workability and good mechanical properties and, in addition, copper has the best electrical and thermal conductivity of any commercial metal on one hand. On the other hand, because of their properties such as optical, electronic, magnetic as well as catalytic, gold nanoparticles keep on emerging compared to those of bulk materials. These unusual properties make them able to offer a wide range of applications (Daniel and Astruc, 2004, Huang and El-Sayed, 2010). Since these properties strongly depend on the shape, the size, the crystallinity and the surface structure of nanoparticles, significant progresses in synthesis methods emerged in recent years for controlling the particles morphology (Sau and Murphy,

2004, Hebié *et al*., 2013). Among the mentioned synthesis approaches in the literature, the template method, the electrochemical method, the microwave rapid heating, the laser ablation, and the seed-mediated growth methods have been undertaken to yield gold nanoparticles with uniform sizes and morphologies (Langille *et al*., 2012, Sau and Murphy, 2004). Nanocomposites have also attracted considerable attention due to their superior properties in comparison with their monometallic counter parts. Thus, copper–gold nanocomposite will then have good electronic, chemical and mechanical properties which would be able to enhance the electrochemical performances of $LiMn_2O_4$. Many methods have been used in synthesizing nanocomposites, below in Table 2 is a summary of some of the methods used for the synthesis of nanomaterials.

Table 2: Different methods for synthesizing nanocomposites

Method	Description of the Method	Advantages	Disadvantages	References
Molecular Beam	Here beams are directed to a particular metal targets using a variety of methods; laser vaporization, pulsed arc, ion and magnetron sputtering. Which leads to the formation of clusters of metallic nanoparticles including nanoalloy.	(1) Easiness of creating any type of nanoparticle or nanoalloy from metallic / alloy targets. (2) The synthesis of nanoparticles is easy and quick.	(1) Procedure is costly, and requires equipment setup in most cases.	(Alonso *et al*., 2009, Ferrando *et al*., 2008)
Ion-Implantation	In this method the implantation of two or more metal ions into a particular matrix leads to the formation of nanoallos. This generates metallic / bimetallic clusters.	(1) Metallic ions can be implanted into exact positions in a matrix. (2) Various combinations of ions can be used To yield nanoalloy clusters.	(1) Requires equipment setup which is relatively expensive compared to chemical reduction.	(Ferrando *et al*., 2008)
Electrochemical Synthesis	Using an electrolysis cell and two electrodes of metallic elements, Bimetallic alloys / nanoalloys can be created in solution. Core–shell structures have also been created Via this method.	(1) Various nanoalloy combinations can be synthesized. (2) Cell setup is rather easy and does not need extensive equipments.	(1) Use of chemicals as electrolytes which may yield harmful / toxic gases as by products from the process.	(Starowicz *et al*., 2006)
Thermal Decomposition	Thermal decomposition of metal or metal complexes (for nanoalloys) is produced using high temperature mediums or solvents.	(1) Nanoparticles can be created at relatively low temperatures. (2) Process can create nanoparticles in a wide range of sizes.	1) Requires use of chemicals and solvents which may be harmful to the environment.	(Ferrando *et al*., 2008)
Chemical Reduction	Use of precursor salts, reducing agents and stabilizer to synthesize nanoparticles. In most cases a catalyst and some heating is used.	(1) Can readily produce bulk quantities of nanoparticles and nanoalloys. (2) Process can be easily scaled up to meet mass manufacturing needs. (3) Process enables synthesis of particles close to 1 nm and this can easily be controlled. (4) Process is relatively cheaper compared to other synthesis methods since the technology is quite standard.	(1) Mass use of chemicals and some may be harmful to the environment. (2) Processing is time consuming and depends on many parameters.	(Hu and Easterly, 2009)

2.5 Cathode Material Enhancement through Nanotechnology

Various experimental strategies have been carried out in order to optimize the performance of $Li_xMn_2O_4$ spinels. Among them, the following are worth noting: change of the morphologies and size of the spinel particle (Pistoia and Wang, 1993), introduction of structural defects in the spine (Schoonman *et al.*, 1999), and doping of the spinel with diverse metallic ions (Pistoia *et al.*, 1997). Electrochemical reactions start at the electrode-electrolyte interface, hence control of the interfaces via doping can decrease the interface side-reactions with the electrolyte and improve the Li-ion diffusivity. The template method also plays a crucial role in improving electrode material efficiencies. A well-structured material improve power density, have relatively large surface area and thereby decreases the current density per unit surface area, the thin wall reduces Li^+ diffusion path length and they facilitate ionic motion more easily. The substitution of various dopants into $LiMn_2O_4$ framework can also contribute to obtain significant improvements in its electrochemical performance (Churikov *et al.*, 2009). Various dopants in cathode materials improve electrode kinetics, structural modifications and microstructural effects. Although the performance of cathode materials can be improved by doping, the microstructure formed can also be affected by the dopant additions (Amatucci *et al.*, 1996).

2.6 Modification of Lithium Manganese Oxide with Cu-Au Nanocomposite to Increase the Electrochemical Performance

Partial substitution of manganese by other metals in $LiMn_2O_4$ is a flexible method to improve cycle performance (Jang *et al.*, 1996, Hu *et al.*, 2013). Owing to their structural properties, the Li ion can be easily intercalated / deintercalated from the host, while incorporation of the transition metal conveys redox properties on the system. Copper and gold is promising intercalation host for reversible Li^+ ion based redox chemistry based on the reversible metal redox couple. Nanostructured designs of electrodes are appealing as distance of Li^+ diffusion is limited to the diameter of the nanoparticles (Oh *et al.*, 2009). It is well accepted that nanomaterial have advantages of good cycling performance and short part length for Li^+ transport over their bulk counterparts due to the large contact area between electrode and electrolyte. The increased surface area allows the electrolyte to surround individual particles for better accessibility of the electro-active material. Hence, the development of an electrically conductive nanostructured composite namely Cu-Au nanocomposite with

economically viable transition metals can permit efficient utilization of the combinative merits to acquire cathode material with higher performance.

2.7 $LiMn_2O_4$ Surface Modification through Doping: Work done by Dcientists

Many researchers have modified the surface of $LiMn_2O_4$ by using different doping mode.

2.7.1 Bulk doping

Bulk doping can be classified as single-ion doping or multiple ion doping

2.7.1.1 Single-ion doping

Single-ion doping can have single effect on the structure as well as on the electrochemical performance. But at times, it may have no influence on the electrochemical performance. Below, are some examples of single-ion doping where an increase in cycle performance and a decrease in the first discharge capacity occurred. Below, is an example of surface modification of $LiMn_2O_4$ done through single-ion doping.

Al-doped $LiMn_2O_4$ ($LiMn_{1.8}Al_{0.2}O_4$) were synthesized by a liquid source misted chemical deposition technique for a lithium micro-battery. The $LiMn_{1.8}Al_{0.2}O_4$ exhibited more improved electrochemical recharge abilities than pure spinel $LiMn_2O_4$ film, because the substitution of Al^{3+} for Mn^{3+} increased Mn-O bonding strength in the spinel framework and suppressed the two-phase behaviour of the unsubstituted spinel during the intercalation / deintercalation. It had no capacity fading over 100 cycles and showed an initial discharge capacity of 52 μAh / cm^2 (Kim *et al*., 2003). Moreover, the $LiMn_{1.8}Al_{0.2}O_4$ suffered from large initial capacity losses.

2.7.1.2 Multiple-ion doping

Multiple-ion doping can enable the specified doped $LiMn_2O_4$ to obtain strong features of different elements. Here is example where multiple-ion doping was used. In order to get an improved charge / discharge cycling performance. A chemist synthesized a doped and milled spinel $Li_{1.05}M_{0.02}Mn_{1.98}O_{3.98}N_{0.02}$ (where M = Ga^{3+}, Al^{3+} or Co^{3+}, N = S^{2-} or F^-). The doped spinel presented higher initial specific discharge capacity (117 –126 mAh / g) and had an

excellent electrochemical performance. It also had a low capacity loss even after the 300 th charge and discharge cycles (from 120 to 115 mAh / g or 4 %) (Eftekhari, 2003). It is clear that the multiple-ion doped product had high initial specific discharge capacity and long cycle performance.

2.7.2 Surface doping or coating

Surface doping and coating are not the same, but the likenesses in these two are that they can both modify the surface of the material and also save the dopant. Here are some examples of researchers who successfully modified the surface of $LiMn_2O_4$.

A researcher used Al_2O nanoparticles as coating materials, and as a result the capacity retention of spinel $LiMn_2O_4$ was improved efficiently at room temperature (25 °C) as well as at 55 °C. Moreover the surface improvement of the modified $LiMn_2O_4$ was attributed to three factors: the inhibition of a surface Jahn-Teller distortion, the decreasing of Mn^{3+} dissolution and a good electric contact among particles. As a result, the specific capacity of the modified $LiMn_2O_4$ was lower than that of pristine $LiMn_2O_4$ (Tu *et al*., 2006). The use of Cs as doping material for $LiMn_2O_4$ film provided a high capacity of 127 mA / g and diffusion coefficient of 6.4 $x10^8$ cm^2 / s which were attributed to the film's morphology and electrochemical reversibility (Polo Fonseca *et al*., 2009). A scientist modified the surface of $LiMn_2O_4$ by doping it with copper. As a result, there was an improvement in the electrochemical property through surface modification of $LiCu_xMn_{2-x}O_4$ in the $LiMn_2O_4$, especially at high C rate. Hence, the performance was due to the significant reduction of the side reactions and Mn dissolution between the interface of the cathode electrode and electrolyte (Chan *et al*., 2005). Another researcher used cobalt to modify the surface of spherical $LiMn_2O_4$ by surface doping, and this showed an improvement in the following: an increased in specific capacity and the electrochemical performance during cycling (Guo *et al*., 2007).

For this work, the modification of the surface of the $LiMn_2O_4$ was done by surface doping using Cu-Au nanocomposite due to the fact that surface doping can decrease the manganese dissolution in the electrolyte by reducing the apparent contact area with the electrolyte.

2.8 Electrolytes

In principle an idyllic electrolyte for rechargeable lithium batteries should have the following criterias (Xu, 2004):

(1) It must dissolve and dissociate completely in the nonaqueous, and the solvated ions (especially lithium cation) must flow with high mobility in the media.

(2) The anion should be stable against oxidative decomposition at the cathode.

(3) The anion should be inert to electrolyte solvents.

(4)The anion and the cation must remain immobile toward the other cell components.

(5) The anion must be toxic freeand stay stable against any reaction that can be thermally induced with electrolyte solvents and other cell components). Here are some examples of electrolyte type:

Here are some examples of different electrolyte types

$LiClO_4$ known as non-aqueous electrolyte has been widely used because of its satisfactory solubility and high conductivity(≈9.0 mS cm^{-1} in EC / DMC at 20 °C) along with its high anodic stability (up to 5.1 V on a spinel cathode surface in EC / DMC) (Guyomard and Tarascon, 1994). It has been proven that SEI films created in $LiClO_4$ electrolytes, on lithium as well as on carbonaceous anode surfaces, result in lower impedance than lithium tetrafluoroborate ($LiBF_4$) electrolytes, or those formed in $LiPF_6$ because the HF is not present in the former (Aurbach *et al*., 1997, Aurbach *et al*., 1995). During hydrolysis of $LiPF_6$ and $LiBF_4$, HF is formed, which then reacts with either alkyl carbonate or Li_2CO_3 and produces the highly resistive LiF (Aurbach *et al*., 1995, Aurbach *et al*., 1994). $LiClO_4$ has the advantages of being relatively less hygroscopic and is stable to ambient moisture compared to other electrolyte. On the other hand, when chlorine is in its high oxidation state (VII) in perchlorate it becomes a strong oxidant, which eagerly reacts with most organic species under high temperature and high current charge (Besenhard and Eichinger, 1976). In fact, in 1970s it was established that $LiClO_4$ was impractical as an electrolyte solute for industry work (Besenhard and Eichinger, 1976). However, it is still regularly used since it is easy to handle and it is low cost (Tan and Johan, 2011, Liu *et al*., 2001, Kuribayashi *et al*., 1995, Tarascon *et al*., 1995). Another type is aqueous electrolyte, which has the advantages of higher conductance and the fact that purification and drying process during production are less stringent. The costs of aqueous electrolytes are usually much lower than suitable organic electrolytes. Note: the structure of the electrode has to be adapted for the size and the

properties of the respective electrolytes. In order to avoid electrolyte depletion problem during charging, the electrolyte concentration has to be kept high. If the electrolyte reservoir is too small compared to huge surface area of the electrodes, performance of the cathode is reduced. For this MSc research study work, 0.1 M $LiClO_4$, 1 M $LiClO_4$, 1 M $LiNO_3$ and 1 M Li_2SO_4 were used as electrolyte for the electrochemical characterization of $LiMn_2O_4$ and $LiM_xMn_{2-x}O_4$.

CHAPTER 3 : EXPERIMENTAL SECTION AND CHARACTERIZATION TECHNIQUES

3.1 Introduction

This chapter describes the general experimental synthesis of $LiMn_2O_4$ via co-precipitation method, Cu-Au nanocomposite via chemical reduction and the synthesis of $LiM_xMn_{2-x}O_4$ using a stoichiometric amount of the synthesized $LiMn_2O_4$ and Cu-Au nanocomposite as well as the instruments and characterizations techniques used.

3.1.1 Reagents and materials

For the success of this work, the reagents and materials used were as follow: Manganese (II) acetate (99 %), Lithium Hydroxide (99 %), Copper (II)Acetate (99 %), Gold (III) Acetate (99 %), Sodium Citrate (99 %), Lithium perchlorate (99 %), Tri-sodium Citrate (99 %), Lithium Sulfate (99 %), Sulphuric Acid (99 %) the above mentioned chemical were purchased from Sigma-Aldrich and N-methylpyrrolidinone (NMP) (99 %), was purchased from Alfa Aesar. Deionized water (18.2 MΩ) purified by a milli-QTM system (Millipore) was used for aqueous solution preparations. Analytical grade argon (Afrox, South Africa) was used to degas the system.

3.1.2 Powder of preparation nanoparticles $LiMn_2O_4$ cathode material

Spinel $LiMn_2O_4$ was prepared via a co-precipitation method at low temperature by the reaction of a mixture of LiOH and ($MnAc_2{\cdot}4H_2O$) (Chan *et al*., 2005). A stoichiometric amount of LiOH and ($MnAc_2{\cdot}4H_2O$) with cationic ratio of Li / Mn = 1:2 were dissolved in deionized water and mixed well by stirring gently. The mixture was switched to a thermostat bath for complete reaction. The solution was then evaporated at 100 °C for 10 h to obtain the precursor powder. Finally the precursor was preheated at 400 °C for 1 hour, and then subjected to calcinations at 400 ^oC 600 °C, 800 ^oC, 860 ^oC, and 880 ^oC for 10 h, then for 15 h respectively in a muffle furnace to form $LiMn_2O_4$.

3.1.3 Preparation of copper-gold nanocomposite

Gold nanoparticles (AuNPs) were prepared through the reduction of 1.0 mM gold acetate using sodium citrate as the reducing agent. 20 mL of 1.0 mM Gold acetate solution was added to a 50 mL Erlenmeyer flask on a stirring hot plate. A magnetic stirrer was added into the solution and the solution heated to boil. To the boiling solution, 2 mL of 1% solution of

sodium citrate, ($C_6H_5O_7Na_3$) was added. Gold sol progressively formed as the citrate reduced Au^{3+} to Au^0 as seen in Equation 2. The solution was heated until a deep pink colour was observed (McFarland *et al*., 2004).

$$Au^{3+} + C_6H_5NO_7Na_3 + 2H_2O \rightarrow Au^o + C_6H_5O_7H_3 + 3Na^+ + H^+ + O_2 \quad (2)$$

Copper-gold nanocomposite (Cu-AuNPs) were synthesized via a previously reported procedure of Ag-Au alloy nanoparticles (Pal *et al*., 2009). 49 mL of water was added into a 100 mL round bottomed flask. 0.5 mL 2% (w / v) sodium citrate was added into the flask of water and the reaction mixture heated to 92 °C. 0.5 mL of a mixture of 10 mM gold acetate and 10 mM copper acetate solution was added into the reaction mixture and the temperature regulated between 90 °C and 92 °C and refluxed for 1 hour. The volume of the mixture was adjusted so as to prepare Cu-Au nanocomposite with Cu / Au ratio of 1:3 by mixing 0.125 mL of 10 mM $Cu(OAc)_2$ and 0.375 mL of 10 mM $Au(O_2CCH_3)_3$. After refluxing the mixture at temperature between 90 °C and 92 °C for 1 hour, a colour change was observed in the solution (light pink) indicating the formation of nanocomposite according to the hallmarks reported in the literature (Shin *et al*., 2008).

3.1.4 Synthesis of $LiM_xMn_{2-x}O_4$

For the surface modification of $LiM_xMn_{2-x}O_4$, (where M = Cu-Au nanocomposite), a stoichiometric amount of the as synthesized copper-gold nanocomposite was poured into a beaker, then an addition of a stoichiometric amount of the synthesized semi crystalline power of $LiMn_2O_4$ was added to the solution then evaporated at 100^{o}C until the crystalline $LiM_xMn_{2-x}O_4$ was obtained. Finally, the obtained powder was calcined at 880^{o}C for 15h.

3.1.5 Preparation of glassy carbon electrode (GCE) with $LiMn_2O_4$ and novel $LiM_xMn_{2-x}O_4$

For the successful achievement of the electrochemical measurements, GCE was polished using 1.0 followed by 0.3, then 0.05 μm alumina slurries and rinsed thoroughly with distilled water then sonicated in ethanol and water respectively. 4 μL solutions of the as synthesized $LiMn_2O_4$ and Cu-Au nanocomposite doped $LiMn_2O_4$ dissolved in N-methylpyrolidinone (NMP) were drop-coated onto the surface of the polished GCE and left to dry at room

temperature overnight and it is denoted as $LiMn_2O_4$/GCE and $LiM_xMn_{2-x}O_4$/GCE (where M = Cu-Au nanocomposite) respectively.

3.2 Characterization techniques

In this present work, , thermal gravimetric analysis (TGA), high resolution scanning electron microscopy (HRSEM), high resolution transmission electron microscopy (HRTEM, X-ray diffraction (XRD), fourier-transform infra-red (FTIR), ultraviolet visible spectroscopy (Uv-vis) and cyclic voltammetry (CV), electrochemical impedance spectroscopy (EIS) were used to investigate the physical characteristics and electrochemical properties of $LiMn_2O_4$, Cu-Au nanocomposite and novel Cu-Au nanocomposite doped- $LiMn_2O_4$ samples.

3.2.1 Crystal Structure Analyses, Morphological and Structural Analysis Techniques

3.2.1.1 High resolution scanning electron microscopy (HRSEM)

High resolution scanning electron microscopy (HRSEM) is a versatile imaging technique capable of producing three-dimensional images of material surfaces. Today HRSEM is one of the most frequently used instruments in material research due to its combination of high magnification, large depth of focus, greater resolution and ease of sample observation. The basic operation in HRSEM entails the interaction of an accelerated highly monoenergetic electron beam, originating from the cathode filament, with the atoms at the sample surface. The electron beam is focused into a fine probe which is restored over the sample. The scattered electrons are collected by a detector, modulated and amplified to produce an exact reconstruction of the sample surface and particle profile. A requirement for effective performance is that the surface of the samples should be electrically conductive. During operation electrons are deposited onto the sample. These electrons must be conducted away to earth, thus conductive materials such as metals and carbon can be placed directly into the HRSEM whereas non-metallic samples have to be coated with a gold metal layer to be observed (Cherstiouk *et al*., 2003). Many scanning electron microscopes have an energy dispersive spectrometer (EDX) detection system, which detects and displays most of the spectra of the elements contributing to the sample composition.

HRSEM was used for the characterization of the surface morphology of $LiMn_2O_4$ and novel $LiM_xMn_{2-x}O_4$. The micrographs were obtained using a Zeiss Auriga HRSEM analyser. The detector used, was a secondary electron (SE) type with substitutable accelerating voltage of 25 KV. The maximum resolution used was 10 µm. EDX coupled to the HRSEM was used and to determine elemental composition of the as synthesized cathode materials. The samples were coated with carbon then placed on a nickel grid.

3.2.1.2 High resolution transmission electron microscopy (HRTEM)

Electron microscope is a type of microscope that uses a beam of electrons to create an image of the specimen. It is capable of much higher magnifications and has a greater resolving power than a light microscope, allowing it to see much smaller objects in finer detail. They are large, expensive pieces of equipment, generally standing alone in a small, specially designed room and requiring trained personnel to operate them. Because the TEM has an unparalleled ability to provide structural and chemical information over a range of length scales down to the level of atomic dimensions, it has developed into an indispensable tool for scientists who are interested in understanding the properties of nanostructures materials and in manipulating their behaviour (Ariga *et al*., 2012). High resolution Transmission electron microscopy (HRTEM) finds its main application in the determination of size, distribution as well as the morphology of synthesized nanoparticles. The principle of HRTEM works in much the same way as an optical microscope. A beam of electrons, generated by the high voltage electron emitter situated at the top of the lens column, interacts with the sample as it passes through the entire thickness of the sample and a series of magnifying magnetic lenses, where they are ultimately focused at the viewing screen at the bottom of the column.

For the achievement of this work, HRTEM was used to determine the size, morphology and the crystallinity of the materials (Kirkland and Hutchison, 2007) using a Tecnai G^2 F2O X-Twin MAT. HRTEM characterizations were performed by placing a drop of the solution on a carbon coated nickel grid and dried under electric bulb for 30 min. Furthermore HRTEM was used to investigate if $LiM_xMn_{2-x}O_4$ had any doping layer of the as prepared Cu-Au nanocomposite

3.2.1.3 Uv-visible spectroscopy

Uv-vis spectroscopy involves the spectroscopy of photons in the Uv-visible region of the electromagnetic spectrum and can be defined as a technique used to study the electronic transitions of materials having transition energy between 10^2-10^3 kJ / mol. When using Uv-vis spectroscopy, one can easily monitor the color as well as the time at once. That monitored colour is the wavelength at which the maximum of the absorption band occurs, and it is written as: λmax, together with the absorbance which occurs at each of these wavelengths. The absorption spectrum tells us about the nature of the material generated. The Absorption light at a specific wavelength is determined by the ratio: I_t / $I_{i,}$ where I_t is the transmitted light and I_i is the incident light. Henceforth, Absorbance can be expressed by the following:

$$A = -\log I_t / I_{i,} \quad (3)$$

given that each molecule has a definite amount of light. For instance, when Uv-vis light is absorbed by a material, its concentration can be monitor using Beer Lambert relationship given by

$$A = \varepsilon\lambda cl \quad (4)$$

Where λ is the fixed wavelength at which the absorbance is determined, ε is the extinction coefficient (cited at the same value of λ), and l is the optical path length of the sample holder. Moreover, Uv-vis spectroscopy known as one of the best way to identify the analyte, this is due to the fact each precise analyte absorbs energy in the form of photons at different wavelengths (Monk, 2008). Consequently, one is able to identify a definite analyte by the application of Uv-vis spectroscopy.

Uv-visible spectroscopy was used to study the properties of the synthesized Cu-Au nanocomposite as it is known that Uv-visible had the proficiency to the interband electronic transition of semiconductors. The measurements were recorded over a range of 400-800 nm using 2 cm^3 quartz cuvettes with Nicolette Evolution 100 Spectrometer (Thermo Electron Corporation, UK).

3.2.1.4 X-ray diffraction (XRD)

X-ray diffraction (XRD) is a versatile, non-destructive technique which has the ability to reveal detailed information about the chemical composition, the crystallographic structure of natural as well as manufactured materials. Henceforth, XRD is an essential method for the characterization of material. Additionally, XRD is a powerful tool in the study of crystallinity and atomic structure of materials and forms an integral part of the comprehensive characterization study of the consolidated composite carbon material. It is used extensively in the determination of the Bravais lattice types and unit cell dimensions. X-ray diffraction methods can be classified into two types: spectroscopic and photographic. The spectroscopic technique known as the X-ray powder diffractometry, or simply X-ray diffractometry, is the most widely used diffraction method. Because spectroscopic methods can replace most photographic methods, photographic techniques are not widely used as diffractometry in modern laboratories. Additionally, photographic methods are mostly used for the determination of unknown crystal structures (Leng, 2008). In X-ray diffraction, crystalline solids are bombarded with a collimated x-ray beam which causes crystal plane atoms, serving as diffraction gratings, to diffract x-rays in numerous angles. Each set of crystal planes or Miller indices (hkl) with inter-plane spacing (d*hkl*) can give rise to diffraction at only one angle. The diffraction angle is defined from Bragg's law in the equation 3 below, where the intensities of the diffracted X-ray are measured and plotted against the corresponding Bragg angles (2θ) to produce a diffractogram.

$$n\lambda = 2d\mathrm{Sin}\theta \qquad (5)$$

where:

λ = Wavelength of the X-rays

d = Spacing of the planes in the crystal

2θ = Angle of diffraction

For the purpose of this study, XRD was used to investigate the crystallinity phase as well as the purity of the as synthesized cathode material. The x-ray diffraction (XRD) was conducted using Bruker AXS D8 Advance diffractomer (Cu Kα = 1.5406 A^o, voltage 40 KV and current 40 mA) and was recorded in the range 10 -75 degrees. Below in Figure 3.1 is an example of an x-ray diffraction machine.

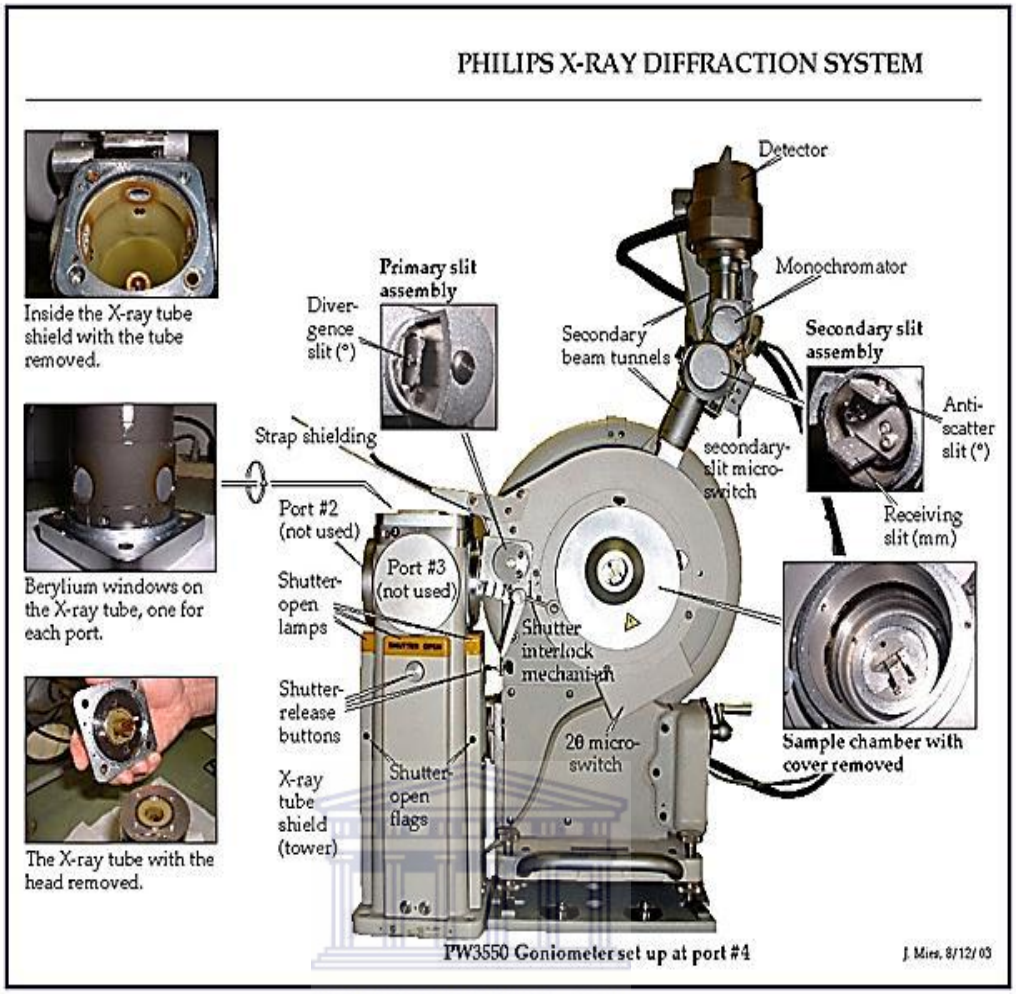

Figure 3.1: X-Ray Diffraction System

3.2.1.5 Fourier-transform infrared spectroscopy (FT-IR)

Fourier-Transform infrared spectroscopy (FT-IR) is more generally applicable towards many samples, since it does not require a Uv chromophore, but rather requires infrared light which is absorbed by the molecular bonds to cause transitions between molecular vibrational states (Vakkasoglu *et al*., 2009). So, it is the absorption measurement of different infrared frequencies by a sample positioned in the path of an infrared beam. The main goal of FT-IR spectroscopic analysis is to determine the chemical functional groups in the sample. The IR spectrum refers to electromagnetic waves whose wavelengths range from 0.78 μm to 1000 μm. However the more manageable, the wave number unit (cm^{-1}) is generally used instead of microns thus the total IR spectrum ranges from 14,286 cm^{-1} to 28.5 cm^{-1}. The advantages of FT-IR are: its superior speed, sensitivity and have been applied to many areas that are very difficult or nearly impossible to analyse by IR-dispersive instruments. Instead of viewing each

component frequency sequentially as in a dispersive IR-spectrometer, all frequencies are examined simultaneously in Fourier transform infrared (FT-IR) spectroscopy (Hallam, Online 2010).

FTIR was used to examine the presence of frequency band responsible for the formation of spinel cathode materials in the range of 500 -4000 cm^{-1} using a PerkinElmer model Spectrum series.

3.2.2 Electrochemical Techniques

Electrochemistry affords some of the most sensitive and informative analytical techniques in the chemists arsenal. Electroanalytical method such as cyclic voltammetry, stripping voltammetry, differential pulse polarography, square wave and chronoamperometry complements other analytical techniques such as chromatography and spectroscopy and are not only capable of assaying trace concentrations of an electroactive analyte, but also supply useful information concerning its physical and chemical properties. Electrochemical methods of analysis include all methods of analysis that measure current, potential and resistance and relate them to analyte concentration. Quantities such as oxidation potentials, diffusion coefficients, electron transfer rates, and electron transfer numbers are readily obtained using electroanalytical methods, and are difficult to obtain using other techniques. Arguably, the most popular electroanalytical techniques are cyclic voltammetry, and square wave. This section describes the basic components of the modern electroanalytical system as well as the principles of cyclic voltammetry (CV) and electrochemical impedance spectroscopy (EIS).

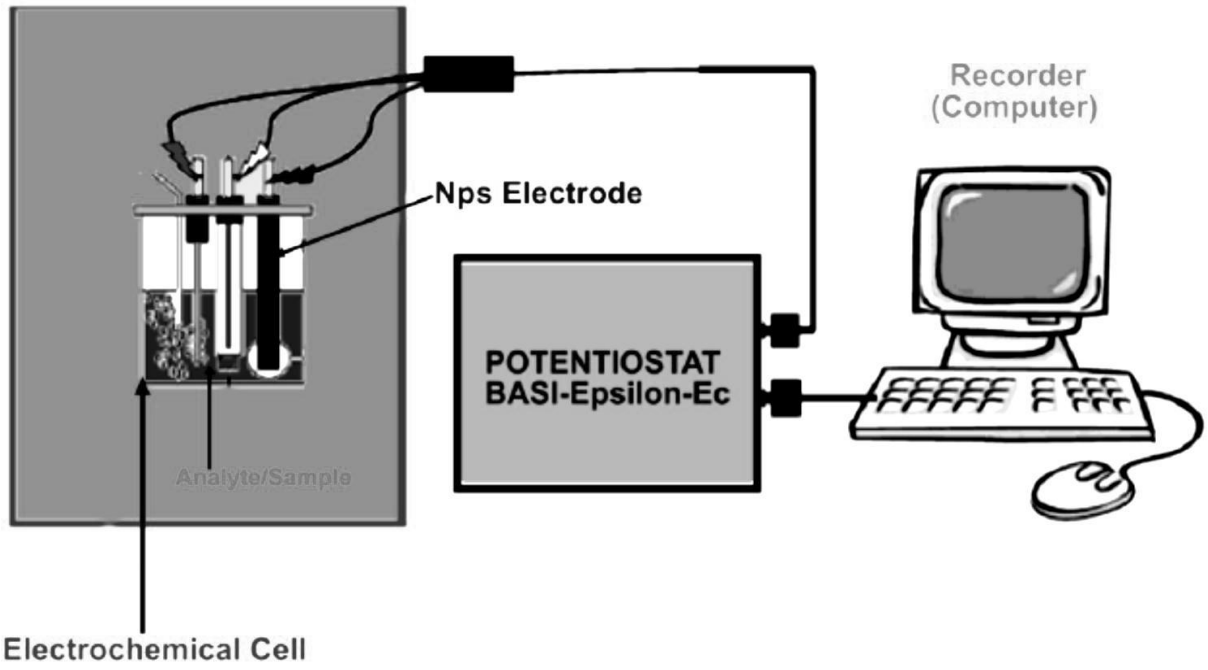

Figure 3.2: A schematic representation of the major components of the electroanalytical system used for electrochemical analysis

3.2.2.1 Cyclic voltammetry (CV)

Cyclic voltammetry is also called linear scan voltammetry and is classified under sweep techniques. The word voltammetry comes from "voltam-" which refers to both potential ("volt-") and current ("am-"). The technique works in the way that different potential are applied at a working electrode at some scan rate (v) in both direction (Forward and reverse) while the current is simultaneously monitored. The instrumentation components for the cyclic voltammetry analysis are: (a) potential equipment (potentiostat) and (b) and electrochemical cell which consist of three electrodes namely working electrode (WE), auxiliary electrode (AE) and reference electrode (RE). During the analysis an electrochemical analyser is connected to a three electrode cell as shown on Figure 3.2.

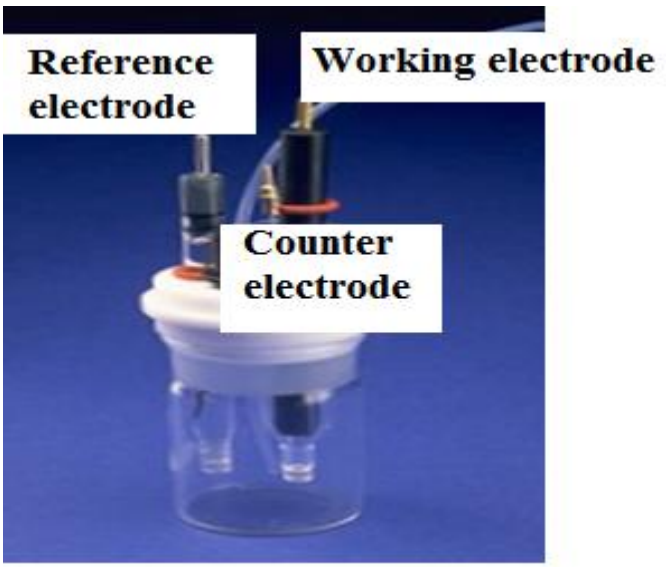

Filgure 3.3: A three electrode cell system

For the duration of a cyclic voltammetric experiment, the potential is ramped from an initial potential *E*i to a more positive or negative potential but, at the end of the linear sweep there is a change in direction of the potential scan which will then reversed, most often stopping at the initial potential *E*i. This allows the measurement of the potential which is usually measured between the reference electrode and the working electrode. However, the current is measured between the working electrode and the auxiliary electrode (Monk, 2008) This data is plotted as current versus potential as shown below in Figure 3.4.

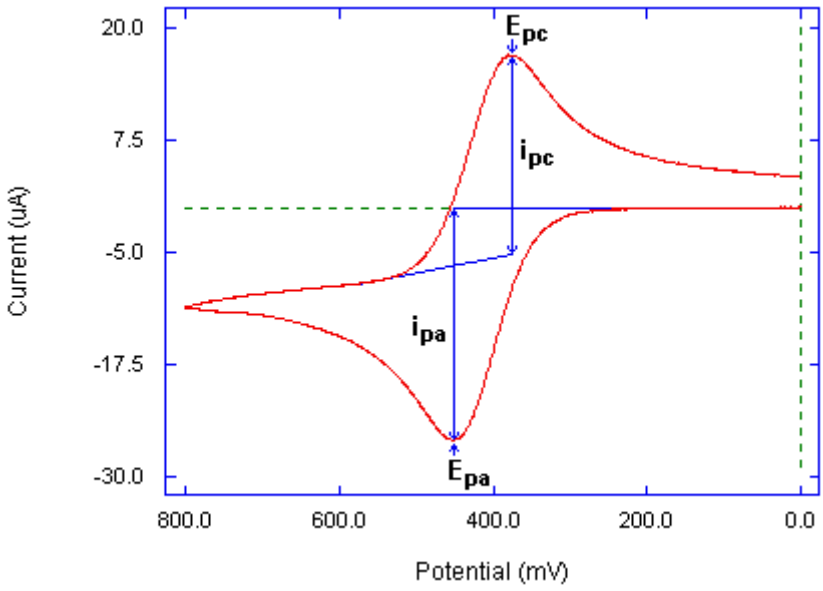

Figure 3.4: An example of a cyclic voltammogram response

During cyclic voltammetry, the forward part is where oxidation takes place, when scanned from a negative to a positive potential. The reverse part of the CV is where reduction takes place, with the potential running from a positive to a negative potential. Additionally if potential is scanned during the forward part of the CV scan from a positive to a negative value, reduction would then occur and oxidations during the reverse CV scan. The parameters obtained from cyclic voltammetry are: peak potentials (E_{pc}, E_{pa}), peak current (I_{pc}) of the cathodic and, peak current (I_{pc}) of the anodic peaks, respectively.

Consequently, theses above mentioned parameters can be used to obtain the most important information needed for the sample under investigation. The information can either be, to determine whether the electrochemical process displayed by the sample is reversible, or irreversible or quasi –reversible. Moreover it can also give an insight on how fast or how slow the electron process is, the same as diffusion process. Δ*E*p is the peak separation (V), which occurs when the electron transfer is fast relative to the diffusion of electroactive species present in the solution at the surface of electrode, and the reaction is said to be electrochemically reversible. The peak separation is given by the following equation:

$$\Delta Ep = [Epa - Epc] = 2.3\frac{RT}{nF} \qquad (6)$$

Where, ΔEp is the peak separation, (n) is the number of electrons involved in the electrochemical process can be estimated from the above equation, *F* is the Faraday constant (96,485C mol^{-1}), *R* is the gas constant (8.314 J mol^{-1} K^{-1}) and *T* is the absolute temperature (K). Thus, for a reversible redox reaction at 25 °C (298 K) with *n* electrons, Δ*E*p should be 0.0592 / *n* V or about 60 mV for one electron (Gosser, 1993). The diagnostic tests for electro-reversibility of a redox couple carried out by cyclic voltammetry are listed below.

1. *I*pc = *I*pa

2. The peak potentials, *E*pc and *E*pa, are independent of the scan rate (*v*)

3. The formal potential (*E*º′) is positioned mid-way between *E*pc and *E*pa, so *E*º′ = (*E*pa + *E*pc) / 2.

4. *I*p is proportional to *v*½

5. The separation between Epc and Epa is 59 mV / n for an n-electron couple (i.e. ΔEp = | Epa - Epc | = 0.0592 / n V).

In the present MSc research work, cyclic voltammetry was measured using a BAS 50B electrochemical analyzer from Bioanalytical systems inc. (West Lafayette, IN) with conventional three- electrode system consisting of glassy carbon electrode (GCE) as the working electrode (A = 0.071 cm^2), platinum wire as the auxiliary electrode and Ag / AgCl (3 M NaCl) as the reference electrode. Alumina micro powder and polishing pads were obtained from Buehler, IL, USA and used for polishing the GCE. All experimental solutions were purged with high purity argon gas and blanketed with argon atmosphere during measurements. The following 0.1 M $LiClO_4$, 1 M $LiClO_4$, 1 M $LiNO_3$ and 1M Li_2SO_4 were used as electrolyte, with a potential window between -1000 -750 mV. The scan rate used were 1 -7 mV / s then 9 mV / s was specifically used for comparison purposes between pristine $LiMn_2O_4$ and modified $LiMn_2O_4$. The experiments were carried out at controlled room temperature (25 °C).

3.2.2.2 Electrochemical impedance spectroscopy (EIS)

EIS analysers are potentiostats that are designed particularly for the measurement of AC impedance and have typical frequency ranges of 10 mHz-100 kHz. A workstation is required to control both potentiostats and EIS analyzers. For the signal amplification and elimination of the background noise, digital post processing is usually engaged. EIS is known as an excellent, non-destructive, accurate as well as rapid insitu technique for inspecting processes that occur at the surface of the electrode as for this work glassy carbon electrode (GCE) was the case. Throughout a controlled-potential EIS experiment, the electrochemical cell is detained at equilibrium and the DC potential is fixed, and a small amplitude (5 –10 mV) AC wave form is overlaid on the DC potential which leads to a generation of a response from the equilibrium position. The obtained response to the applied perturbation is usually sinusoidal, and may differ in phase and amplitude from the applied signal. The obtained data of EIS is generally expressed in a Nyquist plot and bode plot as shown below in Figure 3.5 and Figure 3.6 respectively. Inappropriately, these measurements required a long time in order to be done reliant on the frequency range as well as the stability of the electrochemical system. The imaginary impedance (Z_{Im}) and the real impedance (Z_{Re}) are chronicled as a function of the applied frequency and the obtained data are plotted as Z_{Im} vs Z_{Re} which is the nyquist plot. These obtained data are also simulated using ZView software which aid in giving not only the electrical equivalent circuits as shown in Figure 3.7 but also important information of the interface such as solution resistance (R_s), electron transfer resistance (R_{ct}), Warburg element (W) and double layer capacitance (C_{dl}), are obtained (Macdonald, 2006).

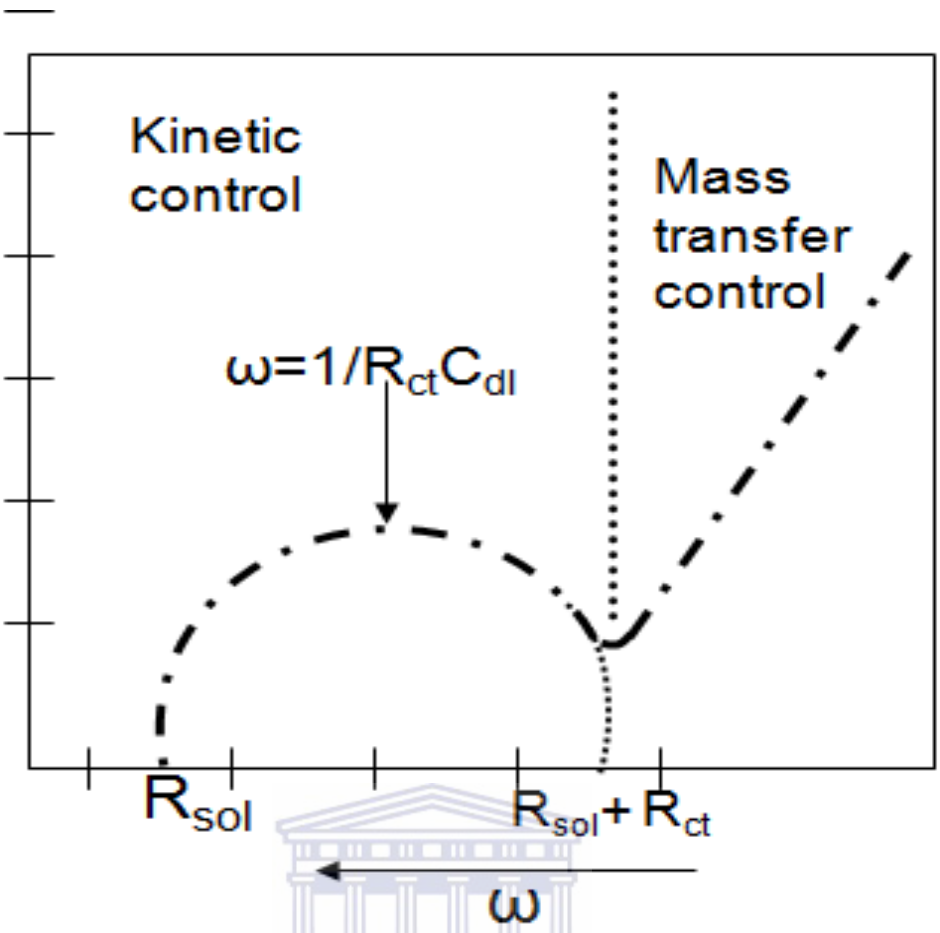

Figure 3.5: A representation of the Nyquist plot displaying the kinetics parameters

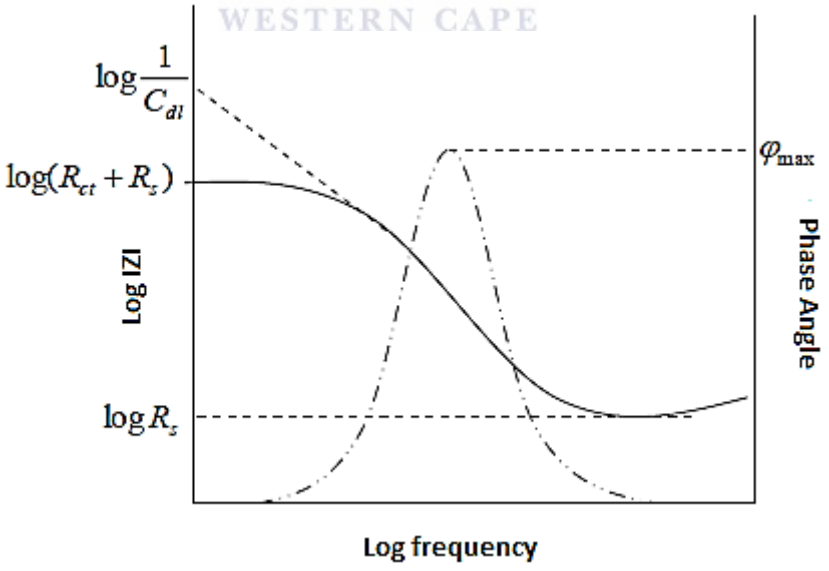

Figure 3.6: A representation of Bode plot showing variation of impedance and phase angle with changes in frequency

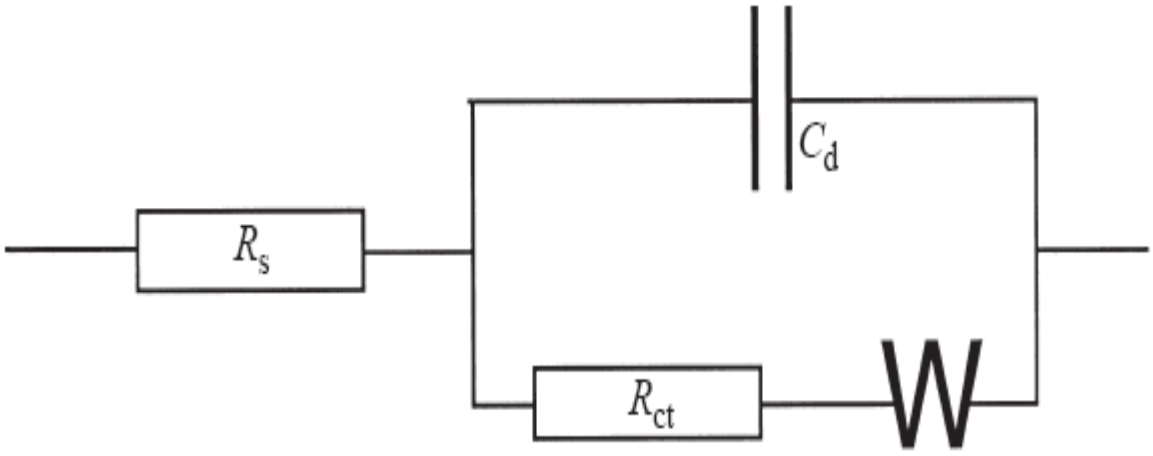

Figure 3.7: An equivalent Randles circuit in series (Macdonald, 2006)

Electrochemical impedance spectroscopy (EIS) measurements were recorded with Zahner IM6ex Germany using electrodes from BioAnalytical systems, BAS, US in three-electrode electrochemical cell with 1 M Li_2SO_4 as electrolyte in the frequency range between 100 mHz to 100 KHz. The amplitude of the applied sine wave potential was 10 mV, whereas the ambient applied dc potential was set at the formal potential (1.05V). The obtained data were plotted in the form of complex plane diagrams (Nyquist and Bode plots).

CHAPTER 4 : RESULTS AND DISCUSSIONS OF $LiMn_2O_4$ AND Cu-Au NANOCOMPOSITE

4.1 Crystal Structure Analyses, Structural Analysis and Electrochemical Characterization of $LiMn_2O_4$ Spinel

4.1.1 Thermal gravimetric analysis (TGA)

Stoichiometric $LiMn_2O_4$ is known as an n-type semiconductor, in which the dc conductivity increases by approximately one order of magnitude as the low-temperature phase (orthorhombic) is transformed into the high-temperature phase (cubic) at a temperature close to room temperature.

In This work thermal gravimetric analysis (TGA) was employed in order to establish the preheating as well as the minimum calcination temperature by applying a heating rate of 10 °C / min from room temperature to 880 °C. Figure 4.1 below proved that weight loss occurred at the three temperature ranges: 20-200 °C then by 200-500 °C and finally 500-600 °C. The miniature weight loss of the first region was ascribed to the superficial water loss due to the hygroscopic nature of the precursor. In the second region, the weight loss is due to the decomposition of the inorganic and the organic constituents of the precursor then by crystallization of $LiMn_2O_4$ phase. Finally in the third region, we observe a flatness of the TGA, which tells us that there are no phase transformation is present, and that any additional heating will simply increase the crystallinity of the sample structure. Henceforth, there is about 2.5% weight loss when the sample was heated to 200 °C, which is attributed to the adsorption of water. From 200 and 350 °C, about 5.5% weight loss is attributed to removal of acetates, followed by 2 wt% loss due to the elimination of the surfactant.

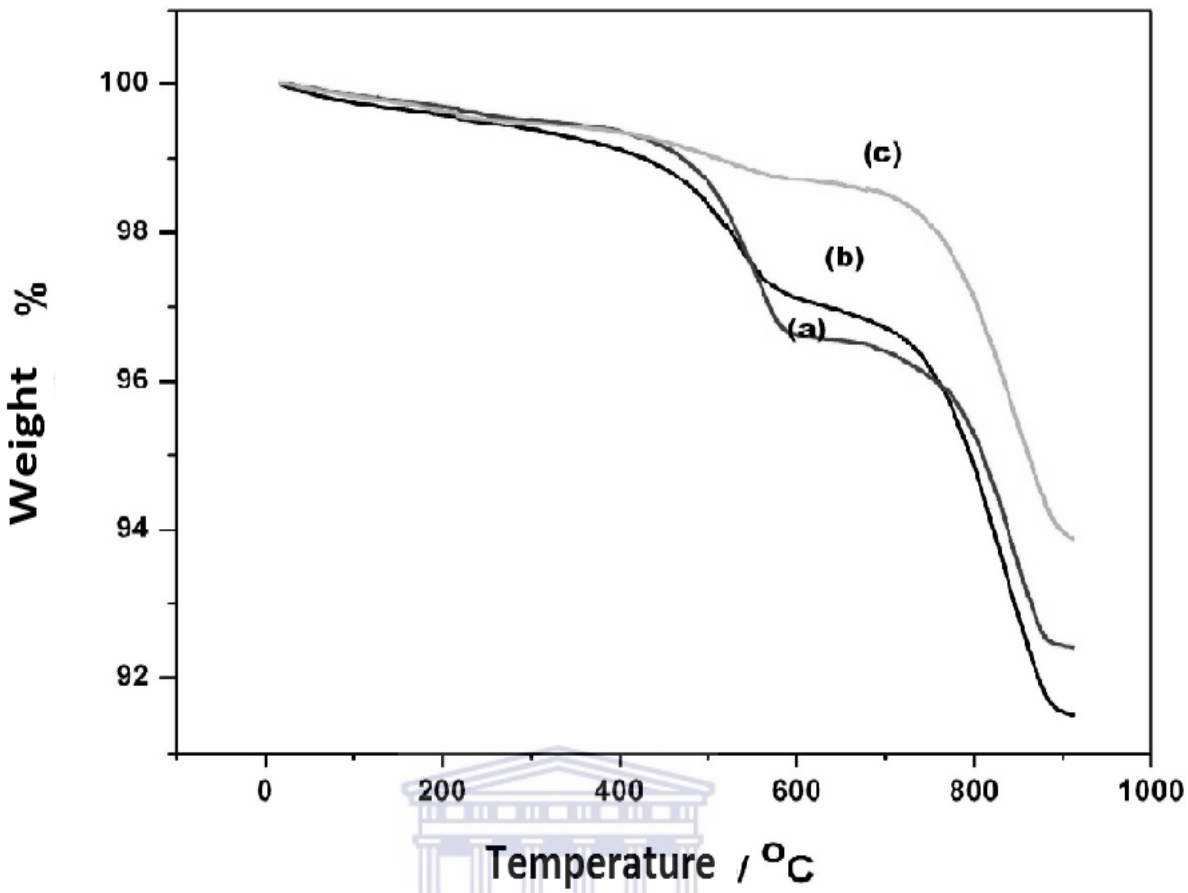

Figure 4.1: TGA curves of the as-synthesized $LiMn_2O_4$ calcined at 800 °C (a), 860 °C (b) and 880 ° C (c), recorded at a heating rate of 10 °C min^{-1}

4.1.2 High resolution scanning electron microscopy (HRSEM)

The high resolution scanning electron microscopy is customarily used to acquire phases based on crystalline structure or qualitative chemical analysis. In this MSc research work, HRSEM was used in order to get high definition morphology of the synthesized spinel $LiMn_2O_4$. The corresponding morphology of $LiMn_2O_4$ as seen in Figure 4.2 is derived from co-precipitation method as explained in the previous chapter. HRSEM micrograph of the pristine $LiMn_2O_4$ shows that the nanoparticles have a rough surface and that two types of particles are seen: primary particles with a shape of spinel of about 50 nm and the secondary particles which are much bigger with a size of more or less 200 nm and which are well agglomerated by those smaller particles. One of the most significant effects of small particles is their ability to support higher rate of lithium inercalation / deintercalation from the oxide host (Jiang and Abraham, 1996). The pristine $LiMn_2O_4$ has obvious visible fringes, indicating that the crystals of spinel $LiMn_2O_4$ grow very well and have good crystallinity which agrees with the XRD

results (Li and Xu, 2008). In order to confirm the composition of pristine $LiMn_2O_4$, with the exception of Lithium as it is not possible to obtain the percentage of lithium, EDX analysis was performed and the obtained results are shown in the Figure 4.3 below. Manganese appears at: Kα = 5.8951 KeV and Lα = 0.6374 whereas oxygen appears at: Kα = 0.5249 KeV which agree perfectly with literature (Williams, 2001). Based on the EDX provided, we noticed that the peak intensity of oxygen is higher than that of manganese this is attributed to the fact that oxygen had a higher composition during the synthesis of nanoparticles $LiMn_2O_4$.

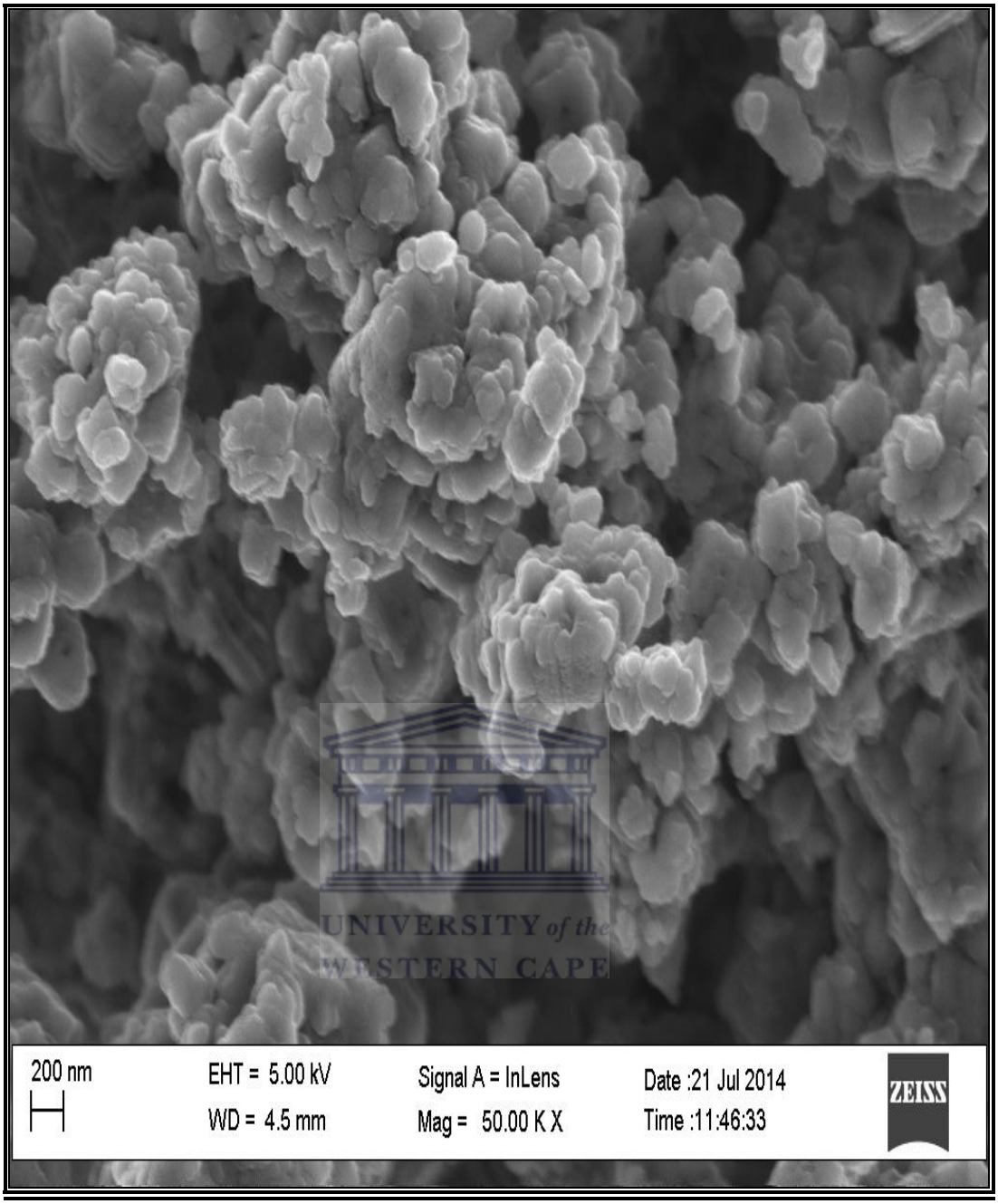

Figure 4.2: High resolution scanning electron microscopy of $LiMn_2O_4$ calcined at 880 ^oC for 15 h.

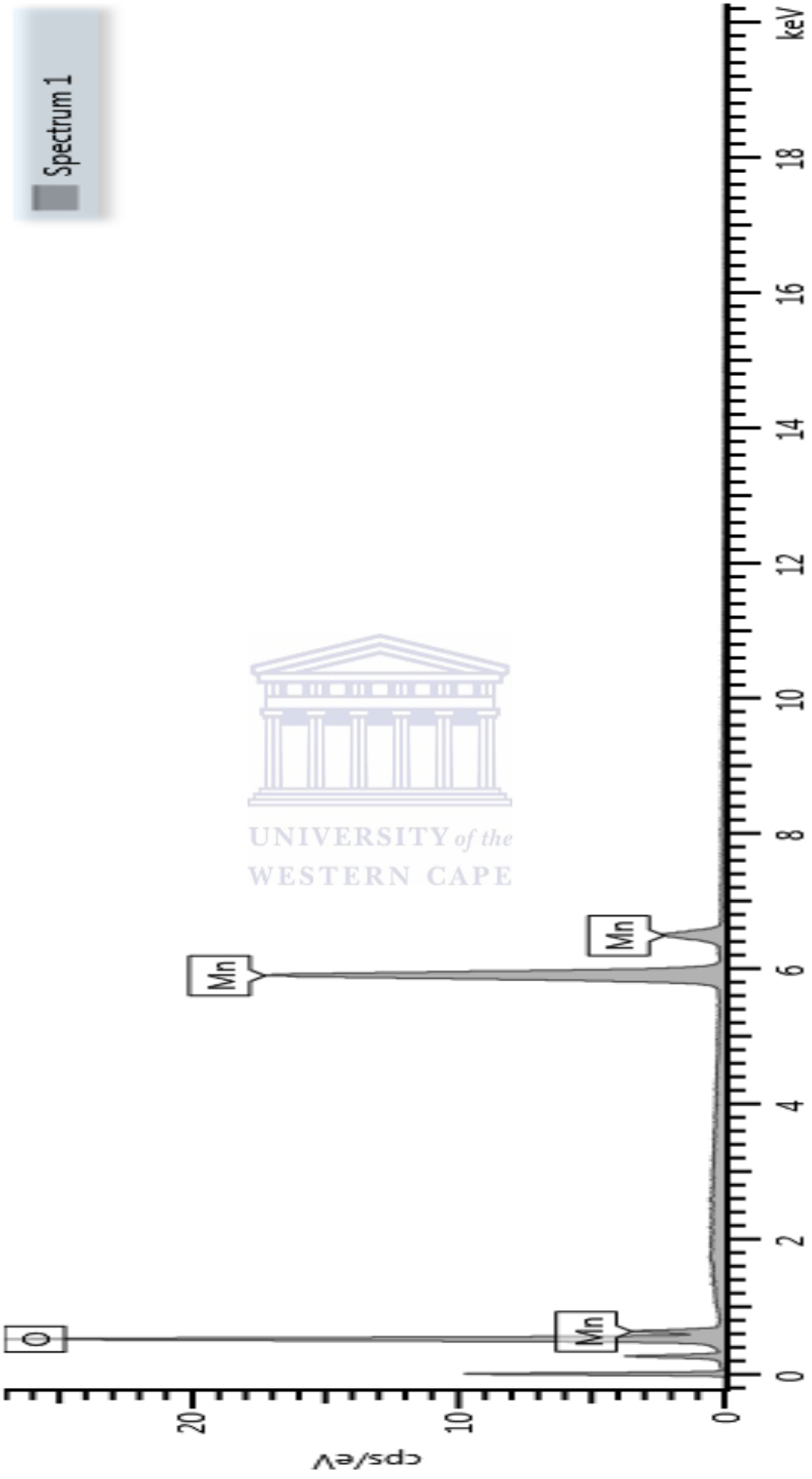

Figure 4.3: HRSEM Energy dispersive X-ray (EDX) of a selected area of pristine $LiMn_2O_4$ on a Nickel grid

4.1.3 X-Ray Diffraction (XRD)

In order to confirm the phase composition and the crystallinity of the heat-treated powder, analysis by XRD is essential. The co-precipitated precursor was heated at 400^{o}C, 600^{o}C and 800^{o}C for 10 h in order to investigate its evolution to the final spinel structure. The XRD pattern of the precursor $LiMn_2O_4$ calcined at 400^{o}C, 600 ^{o}C and 800 ^{o}C for 10 h is shown in Figure 4.4. There appear some broad diffraction peaks of low intensity at 400 ^{o}C, which indicated the incomplete formation of $LiMn_2O_4$. In addition the broadening in peak at 400 ^{o}C is attributed to the small particle present in the HRSEM image of pristine $LiMn_2O_4$ as seen in Figure 4.2. Several minor peaks are also present, which are identified as impurities such as Mn_2O_3. At this stage, it can be concluded that the material is not phased- pure as yet. Lithium manganese oxide with well-developed crystallinity is obtained at 800^{o}C for 10 h. $LiMn_2O_4$ was further acclaimed at various temperatures for 15 h as shown in Figure 4.5. With increase in temperature, the peak intensity and crystallinity of $LiMn_2O_4$ increases while the impurity phase still appears. But once, $LiMn_2O_4$ powder is treated with 2 M sulphuric acid (H_2SO_4) the impurity phase Mn_2O_3 disappeared completely. Thus, it is concluded that an effective way to avoid the formation of the impurity phase is by raising the heat-treated temperature with 2 M sulphuric acid (H_2SO_4) or by prolonging the sintering time (Ying *et al*., 2001). The broadening of diffraction peaks at high scattered angles is indicative of residual strains, which are caused by inhomogeneity of cation or anion non-stoichiometry vacancies, and grain boundary effects in the structure (Naghash and Lee, 2000). In fact, the strains can be reduced or removed through an increase in the heat-treatment temperature. The XRD patterns of the samples from at 800^{o}C to 880°C agree with the pattern of the pure cubic spinel phase of $LiMn_2O_4$ (JCPDS file no. 00-035-0782). The main diffraction peaks, namely, (111), (311), and (400) remain at the same 2θ values for all samples. The ratio of the (111) and (311) (or (400) peaks are greater than unity. The evolution of the precursor $LiMn_2O_4$ with increase in temperature can be summarized as:

Solution based precursor:

$$\xrightarrow{\text{Lower temperature}} \text{decomposition of the product } MnO + O_2$$

$$\xrightarrow{\text{Lower temperature}} \text{spinel phase}$$

$$\xrightarrow{\text{Higher temperature}} \text{crystalline, single phase spinel}$$

The values of lattice parameter a = 8.24, 8.25, 8.26 Å, respectively, obtained for the samples heated at 800, 860 and 880°C agree well with the values reported in the literature (Chan *et al*., 2005). It is known that the value of the lattice parameter of $LiMn_2O_4$ powders is affected by

heating temperature used. For instance, Naghash and Lee synthesized $LiMn_2O_4$ by aqueous co-precipitation of Li and Mn salts (Naghash and Lee, 2000). The precipitate obtained at ambient conditions was calcined at different temperatures and the evolution of the spinel structure was monitored by XRD studies. The lattice parameter increased with the increase of temperature from 8.17 Å at 250 °C to 8.26 Å at 870 °C. But in this present no increase in lattice constant had occurred in the temperature range from 400 ^{o}C-700 ^{o}C, rather a slight increase in the lattice constant was noticed between 800 -880 ^{o}C.

.

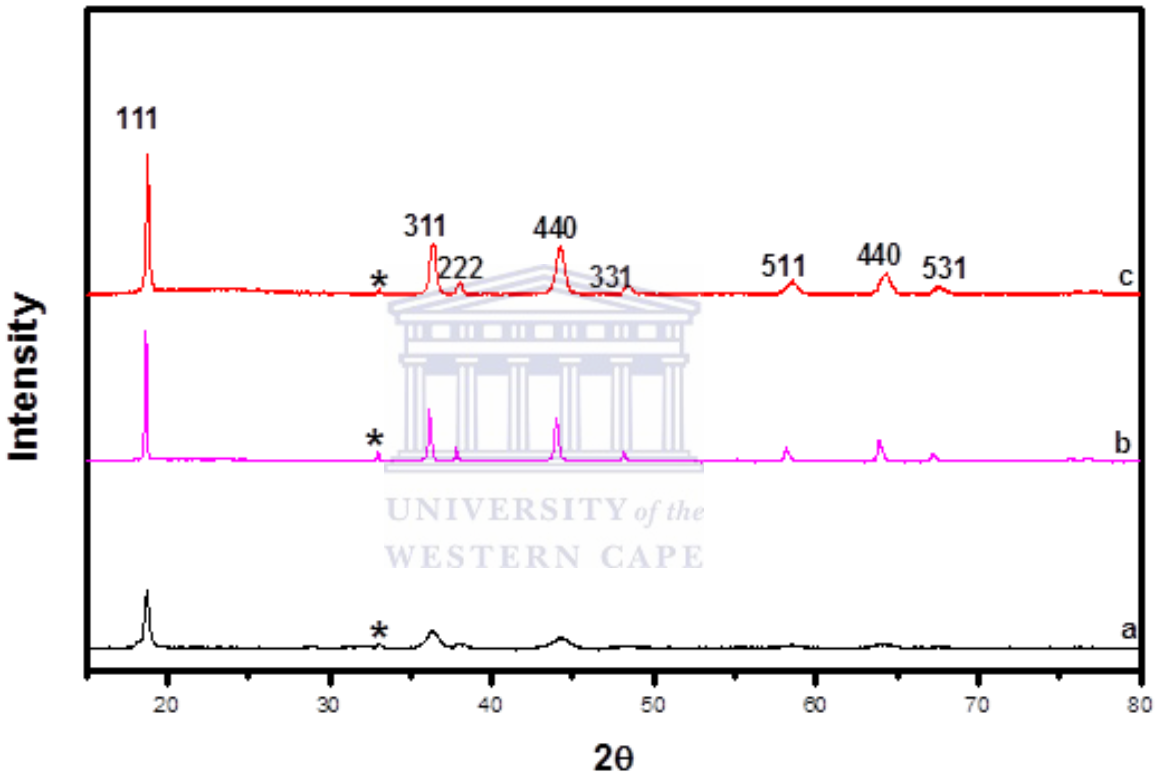

Figure 4.4 XRD of $LiMn_2O_4$ precursor at (a) 400 ^{o}C, (b) 600 ^{o}C and (c) 800 ^{o}C with some impurities present represented by the asterisks sign (*: Mn_2O_3)

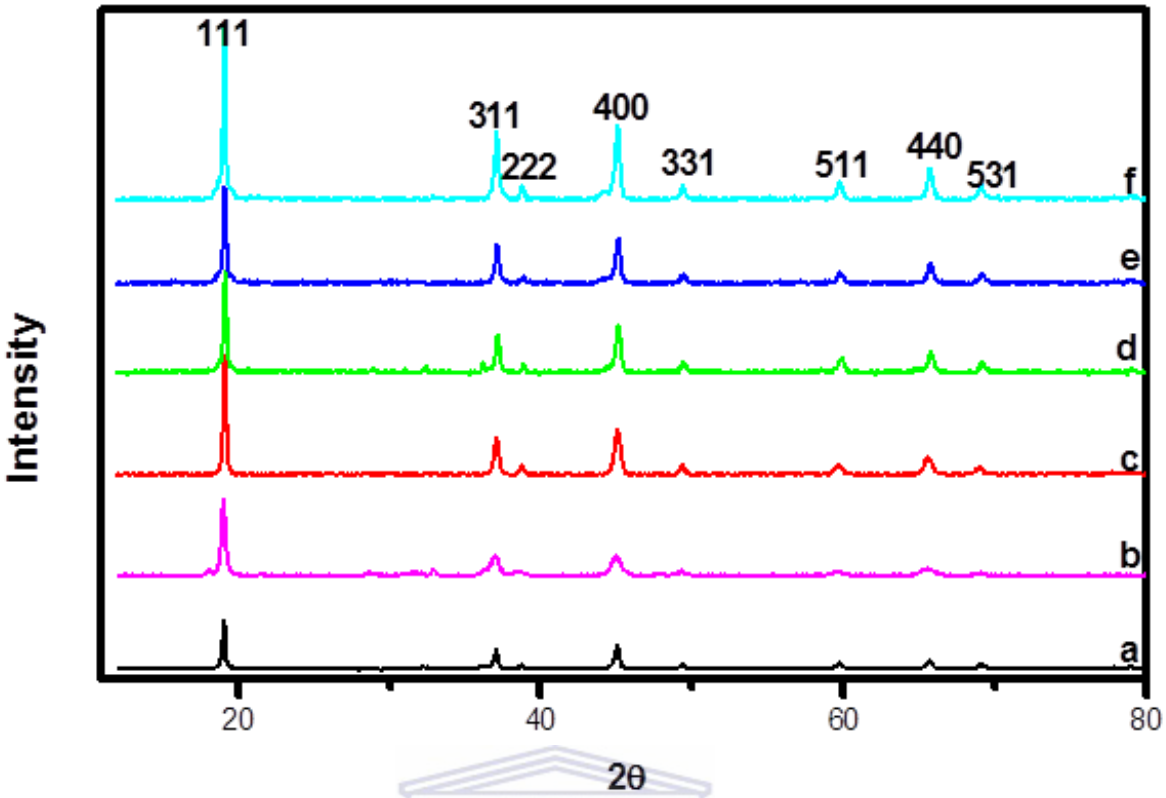

Figure 4.5: XRD pattern $LiMn_2O_4$ treated with 2 M H_2SO_4 then heated at (a) 400^{o}C, (b) 600 ^{o}C, (c) 700 ^{o}C, (d) 800 ^{o}C, (e) 860 ^{o}C (f) 880 ^{o}C for 15 h.

4.1.4 Fourier-transform infra-red (FTIR) of $LiMn_2O_4$

Spinel lithium manganese oxide ($LiMn_2O_4$) powder has been successfully prepared by co-precipitation method using lithium hydroxide and manganese acetate with a ratio of 1:2 respectively. Fourier transform infrared (FTIR) spectroscopy was used to study the structure coordination of the obtained powder in the range 500 -4000 cm^{-1}. The FTIR spectrum is shown in Figure. 4.6. In the spectrum we could see few prominent bands and few weak bands at different wavelength regions. Amongst the bands that are observed from the FTIR spectra, we see that they appeared at, 509, 615, 1220, 1360 and 2970 cm^{-1}. Two frequency bands are observed 509 and 615 cm^{-1}, which are responsible for the formation of $LiMn_2O_4$. They are assigned to the asymmetric stretching of MnO_6 groups which have been reported in the literature (Wei *et al*., 2004). On the other hand, the 1220 and 1360 Cm^{-1} frequency bands are attributed to the O-H bending vibration joined with manganese. The absorption band observed at 2970 cm^{-1} is ascribed to the O-H stretching vibration. From the FTIR spectra, it is revealed that the synthesized product is a single phase $LiMn_2O_4$ compound.

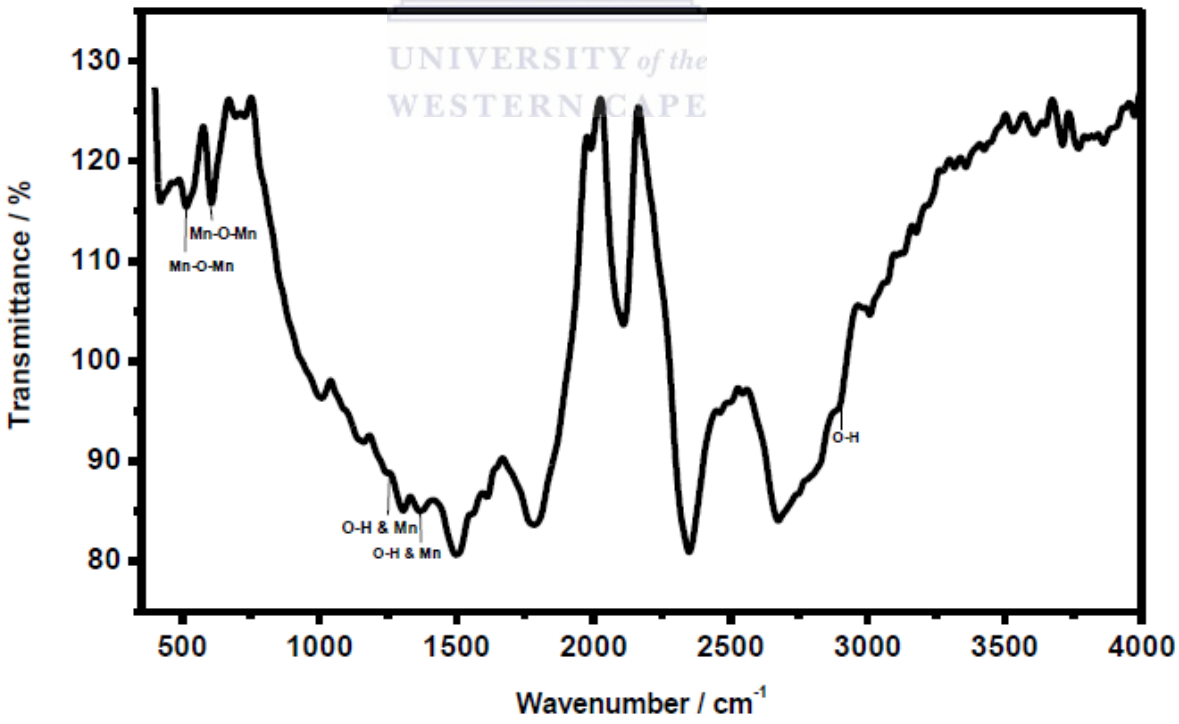

Figure 4.6: FTIR spectra for $LiMn_2O_4$

4.2 Cyclic Voltammetry of Nanoparticles $LiMn_2O_4$

4.2.1 The choice of electrolyte

The choice of 1 M Li_2SO_4 as electrolyte for electrochemical characterization of this MSc research work was done based on few factors that are detailed in the section below. The electrochemistry of the synthesized pristine $LiMn_2O_4$ was studied in four different electrolytes: 0.1 M $LiClO_4$ 1 M $LiClO_4$, 1 M $LiNO_3$ and 1 M Li_2SO_4.

Figure 4.7 and Figure 4.8 represent the cyclic voltammograms of pristine $LiMn_2O_4$ in 0.1 M $LiClO_4$ and 1 M $LiClO_4$. It can be clearly seen that as the scan rate is increased the current also increases. Additionally, a pair of redox peaks lies on the positive site of the applied potential. There is a slight shift that is clearer at 7 mV / s when using 1 M $LiClO_4$. Additionally, the cyclic voltammograms seem to be unstable though it is the same electrolyte but different concentration. This is suggestive of no moral reversibility behaviour.

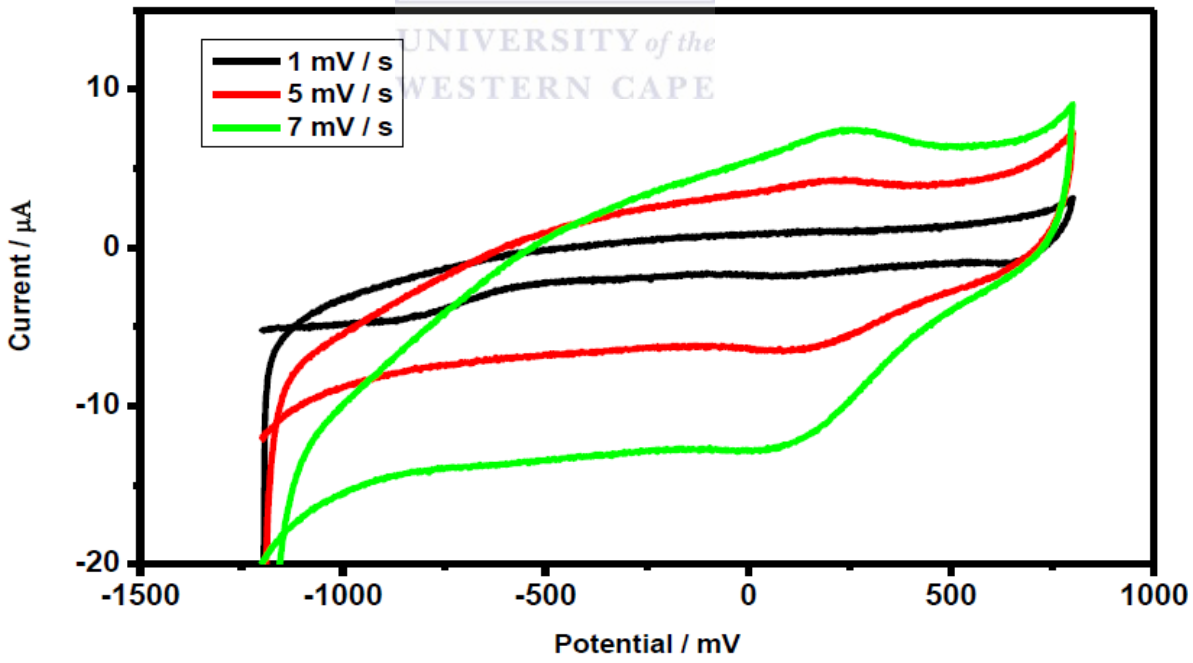

Figure 4.7: **Cyclic Voltammograms of $LiMn_2O_4$/GCE in 0.1 M $LiClO_4$ at different scan rates**

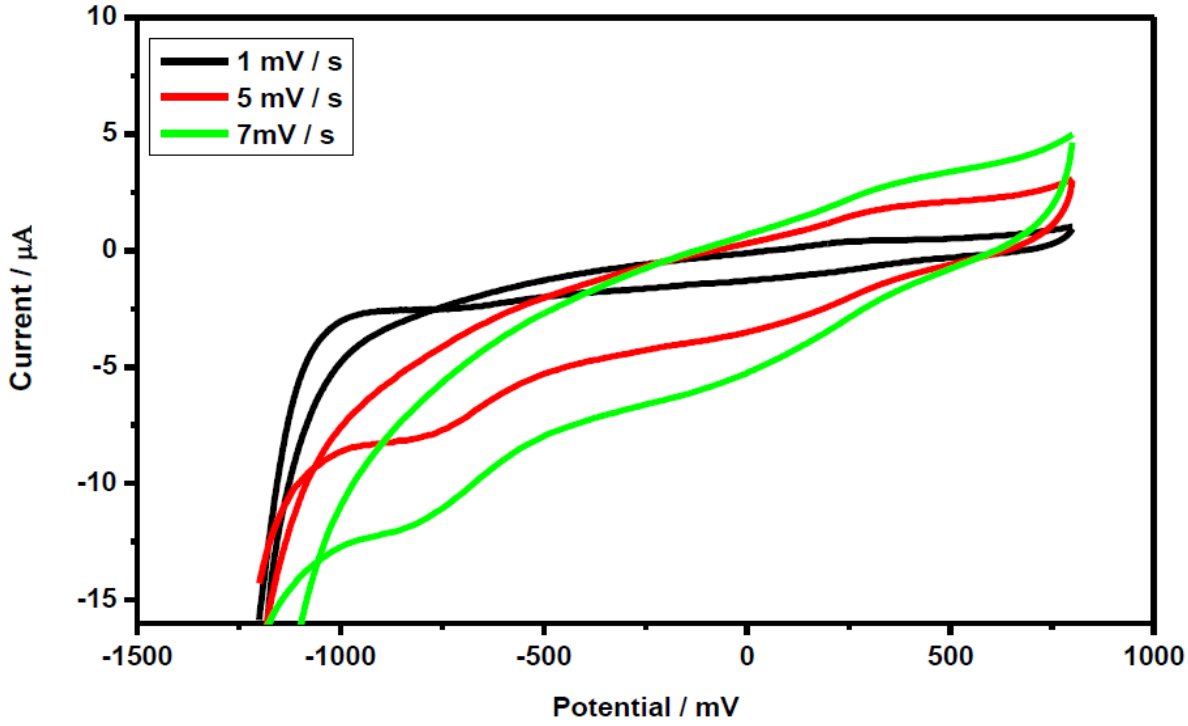

Figure 4.8: Cyclic voltammograms of $LiMn_2O_4$ / GCE in 1 M $LiClO_4$ at different scan rates

Figure 4.9: displays the cyclic voltammograms of pristine in 1 M $LiNO_3$. From the displayed CV it can be visibly seen that the change in scan rate doesn't really make any change on the current. This implies that current is not dependent of scan rate.

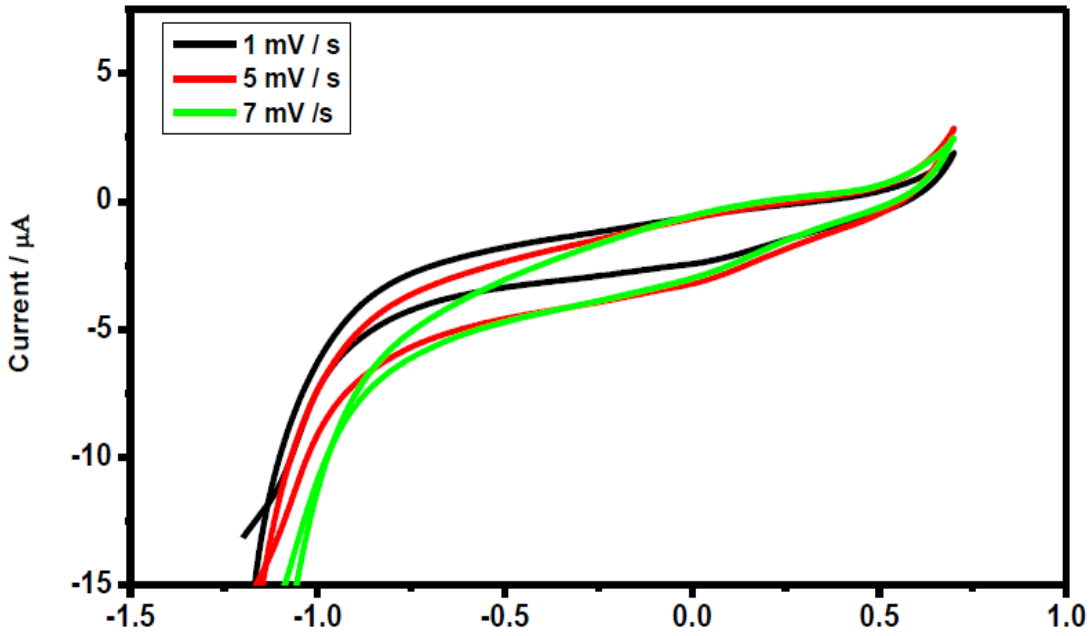

Figure 4.9: **Cyclic Voltammograms of $LiMn_2O_4$/GCE in 1 M $LiNO_3$ at different scan rates**

Figure 4.10 parades the cyclic voltammograms of pristine $LiMn_2O_4$ in 1 M Li_2SO_4. The anodic peak current increases with increase in scan rate, while the cathodic peak current decreases. This indicates a linear dependence of the peak current on scan rates. This means that, $LiMn_2O_4$ is a conductive material that undergoes a speedy reversible electron transfer reaction in 1 M Li_2SO_4.

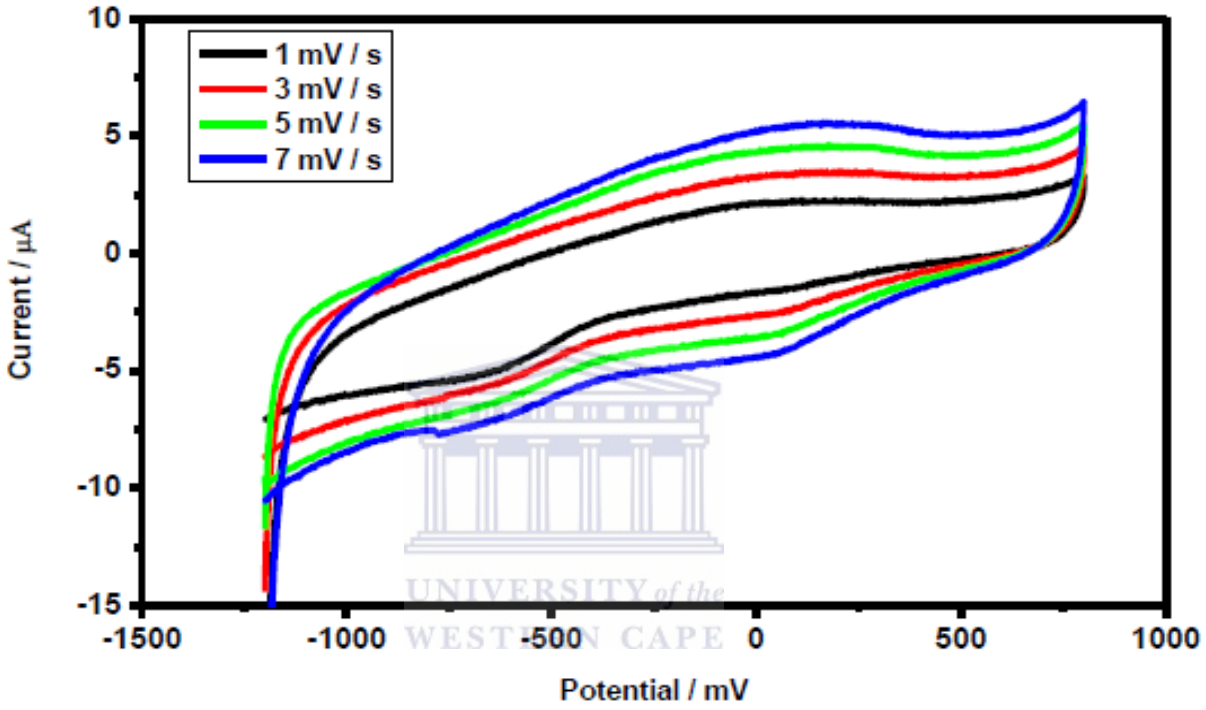

Figure 4.10: Cyclic Voltammograms of $LiMn_2O_4$/GCE in 1 M Li_2SO_4 at different scan rates

From the four displayed cyclic voltammetry responses, it is seen that the obtained voltammogram response varies with electrolyte used. Moreover, the synthesized $LiMn_2O_4$ is found to be more stable in 1 M Li_2SO_4. Consequently 1 M Li_2SO_4 is established to be a suitable electrolyte in this present MSc research study for $LiMn_2O_4$ since it exhibits better electrochemical performance.

4.2.2 The effect on cyclic voltammetry using 1 M Li_2SO_4 as electrolyte

Figure 4.11 represents the cyclic voltammogram $LiMn_2O_4$ at different scan rates varying from 1 -7 mV / s, showing an increase in current intensity as the scan rate increases thus proving that as the scan rate is increased, more electric field is generated. Two pairs of redox peaks were observed in this present work as found by some researchers however, the broadening in peak implies that the process takes place in two steps. The pair of peak A and C_1 is attributed to the insertion / deinsertion of Li^+ at $LiMn_2O_4$ which can be summarized by the following equation:

$$LiMn_2O_4 \leftrightarrow Li_{1-x}Mn_2O_4 + xLi^+ + xe^- \quad (7)$$

The above equation is a typical characteristic which is ascribed to the deintercalation process of Li^+ in the 8a tetrahedral sites of the spinel (Kiani *et al*., 2011)**.** A_1 peak is ascribed to the removal of lithium ion from the tetrahedral sites where Li-Li interaction takes place. Table 3 shows the peak parameter obtained for $LiMn_2O_4$. The effect of sweep rate is examined by plotting the peak current Vs $\upsilon^{1/2}$. It is found that the peak current increases linearly with increase in scan rate.

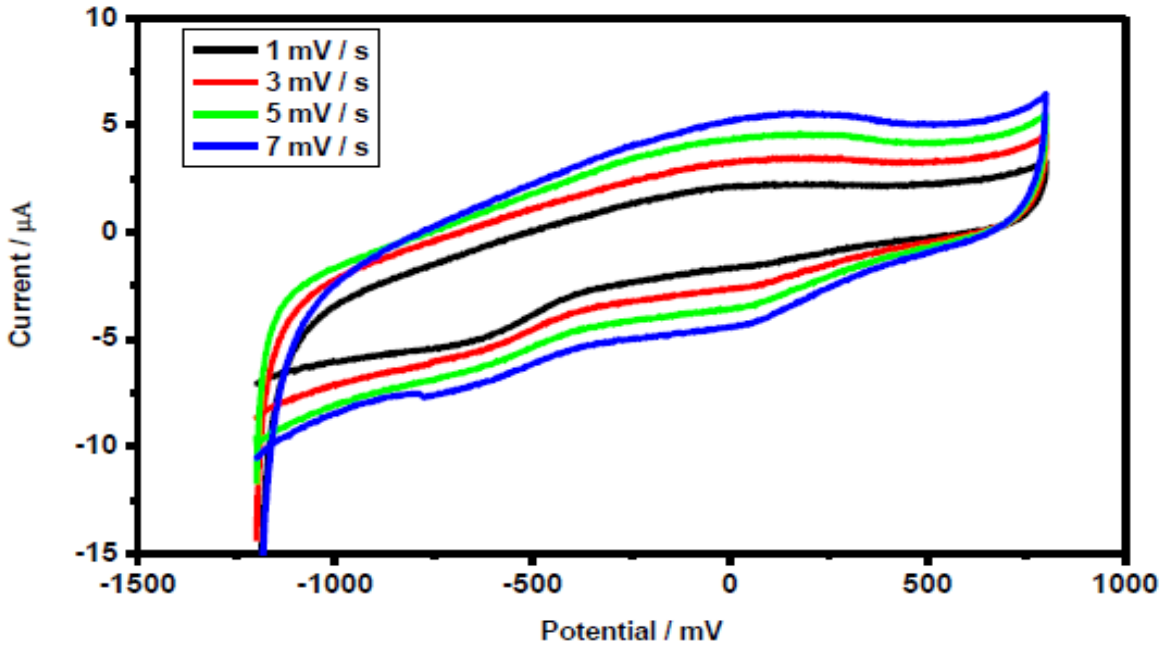

Figure 4.11: Cyclic Voltammograms of $LiMn_2O_4$/GCE in 1 M Li_2SO_4 at increasing scan rates

Table 3: Peak current of $LiMn_2O_4$ versus square root of scan rate

Scan Rate / mV / S	Square root of scan rate / $(mV)^{1/2} s^{-1/2}$	I_p^{ox} / μA	I_p^{red} / μA
1	1	2.059	-1.615
3	2.23	3.410	-2.589
5	2.64	4.298	-3.720
7	3.16	5.57	-4.483

Figure 4.12 below represents a plot of peak current versus root of scan rate which shows that the anodic current peak current increases with increase in scan rate while the cathodic peak current becomes more negative.

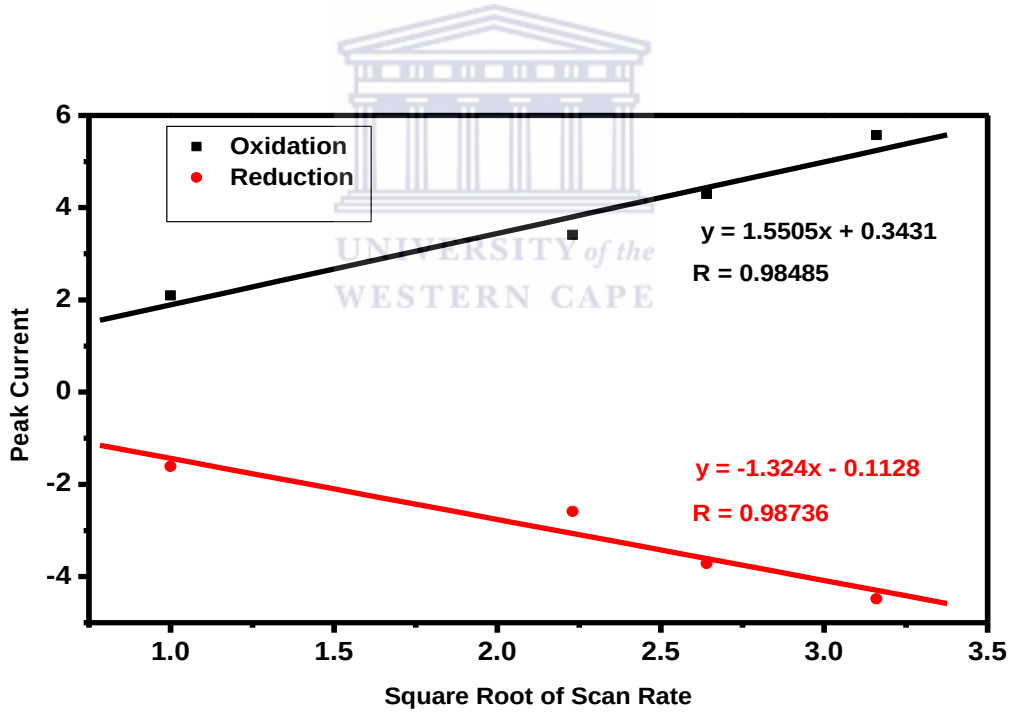

Figure 4.12: A graph of peak current Vs square root of scan rate of $LiMn_2O_4$

4.3 Morphological Analysis of Cu-Au Nanocomposite

4.3.1 Absoption analysis of Cu-Au nanocomposite by Uv-visible spectrocopy

Uv–vis spectroscopy is a very useful technique for estimating the optical band gap of a semiconductor. The optical band gap is related to the electronic conductivity of the materials. The formation of Cu-Au (1:3) nanocomposite by simultaneously reducing copper and gold was confirmed using Uv-visible spectroscopy. Figure 4.13 below shows the visible absorption of copper-gold nanocomposite, and that of gold nanoparticles (inset). Absorption band with maximum intensity of 547 nm is observed for copper-gold nanocomposite and of 528 nm for gold nanoparticle (inset). Moreover the peak of the latter is broader than that of the former; this may be due to the presence of copper and gold. The appearance of a single absorption at 547 nm shows that Cu-Au nanocomposite was formed. In addition the broadening of the peak obtained is due to the residue of the cooperative oscillation of the Plasmon's surface (Taleb *et al*., 1997). Furthermore, the presence of the red shift as well as the broadening in the absorption band of Cu-Au nanocomposite compare to the pure gold nanoparticles that has a narrower peak is observed. This implies that the Cu-Au nanocomposite has a larger size distribution because they are more clustered. Energy band gap, known as the difference between LUMO and HOMO is calculated, and the value of 2.28 eV is obtained for the synthesized nanocomposite. This suggests that, it's a semiconductor as shown in Figure 4.14. This implies that, Cu-Au nanocomposite will be able to enhance the conductivity of $Li[Cu\text{-}Au]_{0.02}Mn_{1.98}O_4$ cathode materials. The formula below, was used to calculate the energy band gap.

$$E = \frac{hc}{\lambda} \tag{8}$$

Where, E is the band gap energy, h is the Planck's constant with a value of $4.135667516 \times 10^{-15}$ eV, C is the speed of light with a value of 3×10^{8} m / s and λ is the absorption peak wavelength; the value obtained during this experiment is 547 nm.

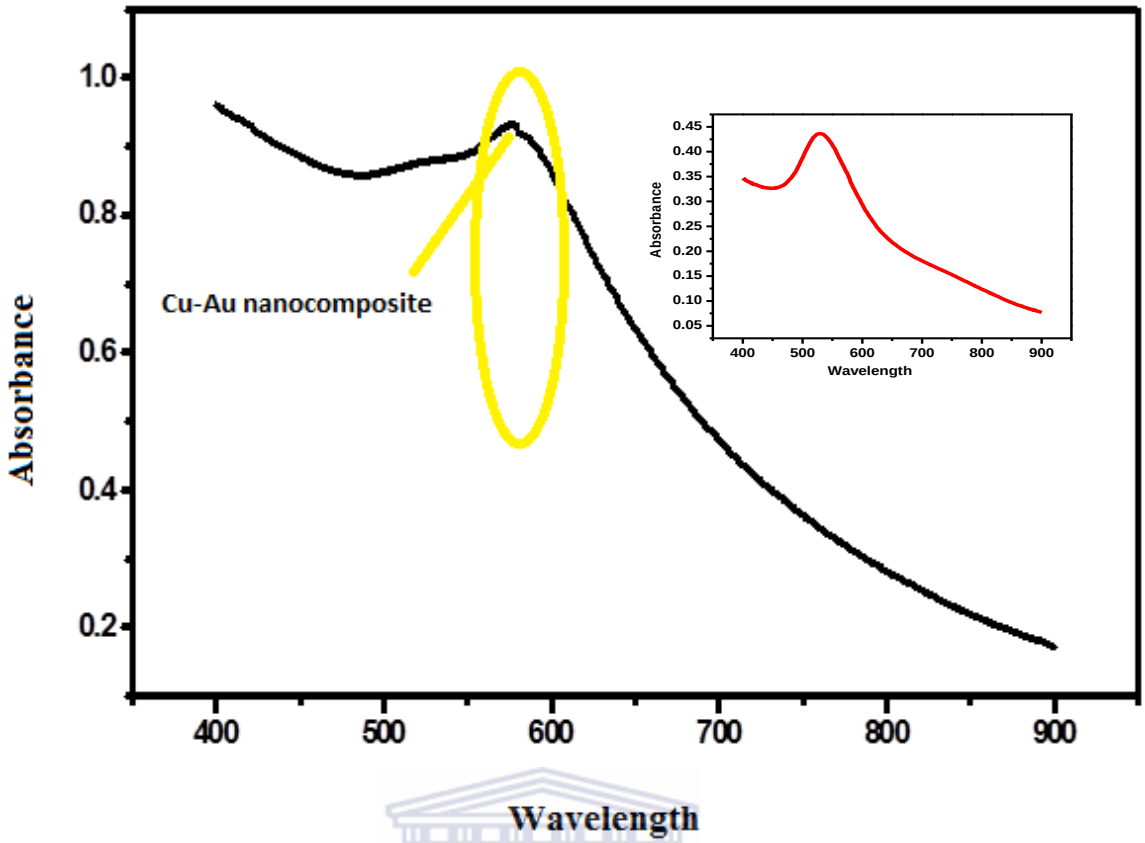

Figure 4.13: Uv-visible of Cu-Au nanocomposite with Au nanoparticles (in set)

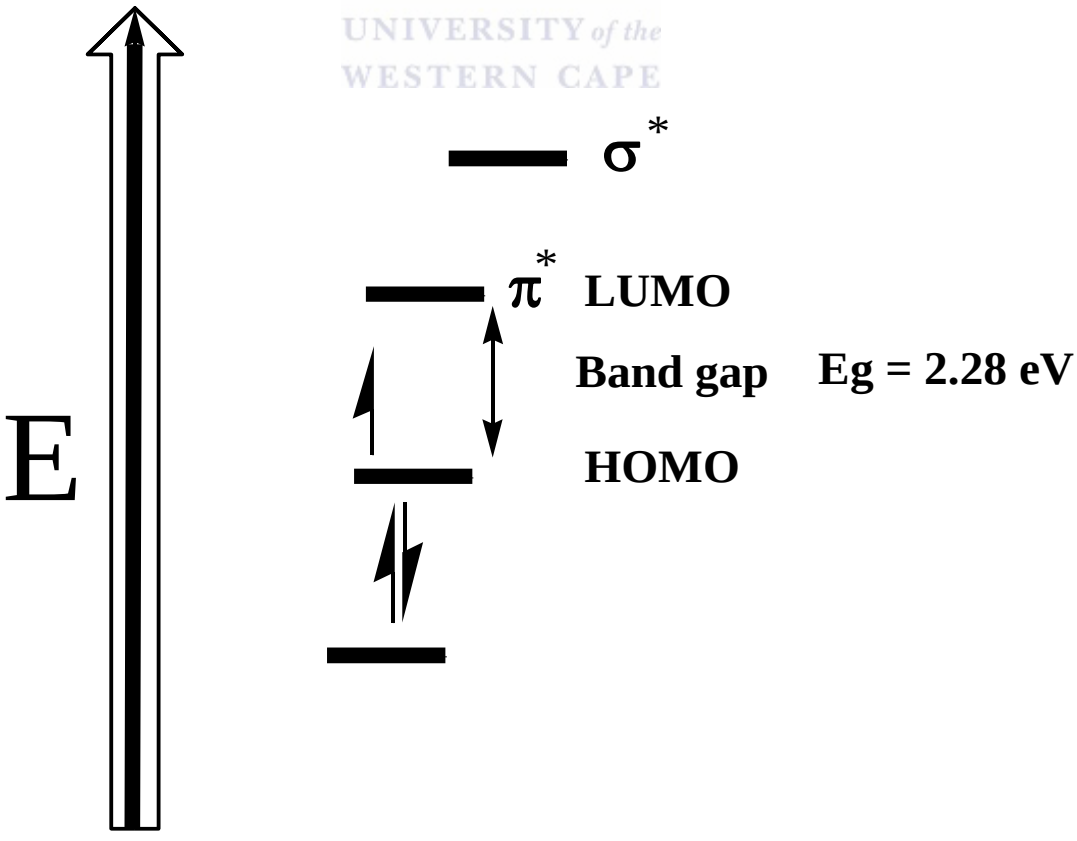

Figure 4.14: Energy diagram of Cu-Au nanocomposite

4.3.2 High resolution transmission tlectron microscopy (HRTEM)

As stated in the previous section, Cu-Au nanocomposite with a ration of (1:3) was synthesized using a chemical reduction method by simultaneously reducing copper acetate and gold acetate with sodium citrate as the reducing agent which also played a role of the capping agent. Negatively charged trisodium citrate molecules were adsorbed on the surface of the nanocomposite leading to a repulsion of the nanoparticles against each other thus stabilizing the nanocomposite by stopping them from aggregating. Figure 4.15 shows the HRTEM image of Cu-Au nanocomposite. The darker core comes from gold due to the fact that they have a higher electron density than copper. From the particle size distribution, it is observed that, the particles size is in the range of 20-40 nm were observed for the Cu-Au nanocomposite. The use of trisodium citrate affects the size of Cu-Au nanocomposite which implies that, with increase of trisodium citrate a decrease in size of the nanocomposite will be observed. Figure 4.16 (a) is the selected area electron diffraction (SAED) of Cu-Au nanocomposite and Figure 4.16 (b) represents the obtained lattice parameter of the nanocomposite. EDX analysis, as seen on Figure 4.17 was further used to confirm the presence of copper and gold. The peak intensity of gold is higher than that of copper due to the fact more gold was used during the synthesis of Cu-Au nanocomposite. On the other hand, nickel and carbon are also observed. This is because; nickel was used as a grid which was coated with carbon. The lines of the synthesized Cu-Au nanocomposite are in impeccable agreement with literature where copper appears at Kα = 8.0413 KeV and Lα = 0.9297 KeV, gold at Lα = 0.7135 KeV and Mα = 2.1205 KeV (Williams, 2001).

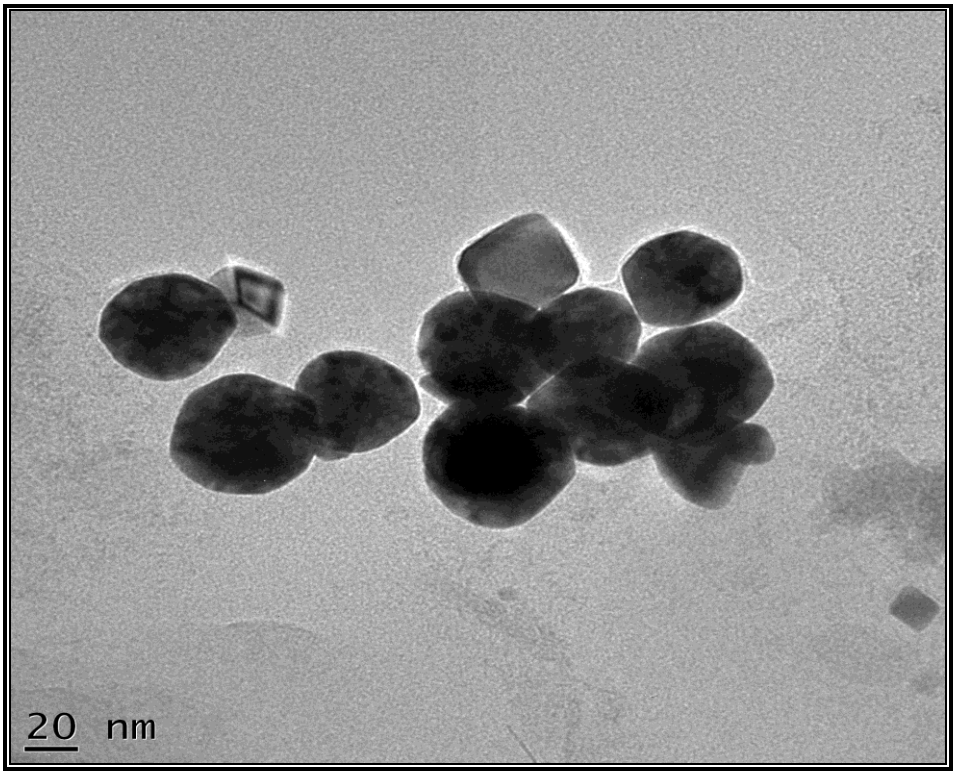

Figure 4.15: HRTEM of Cu-Au nanocomposite

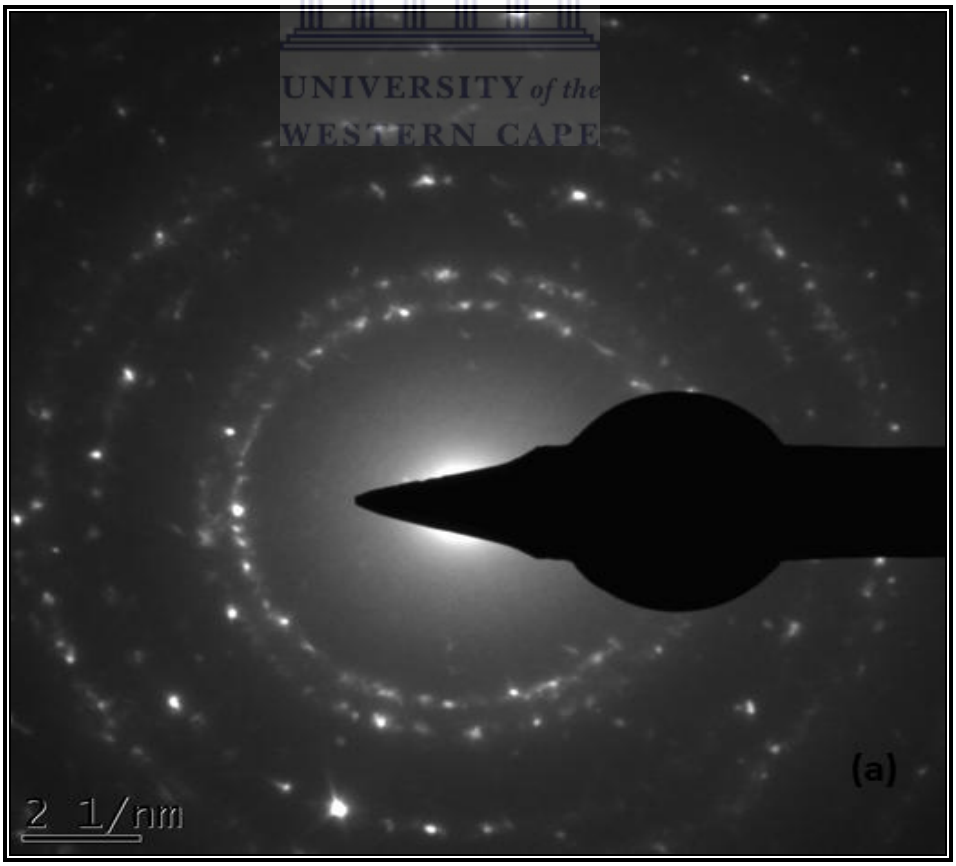

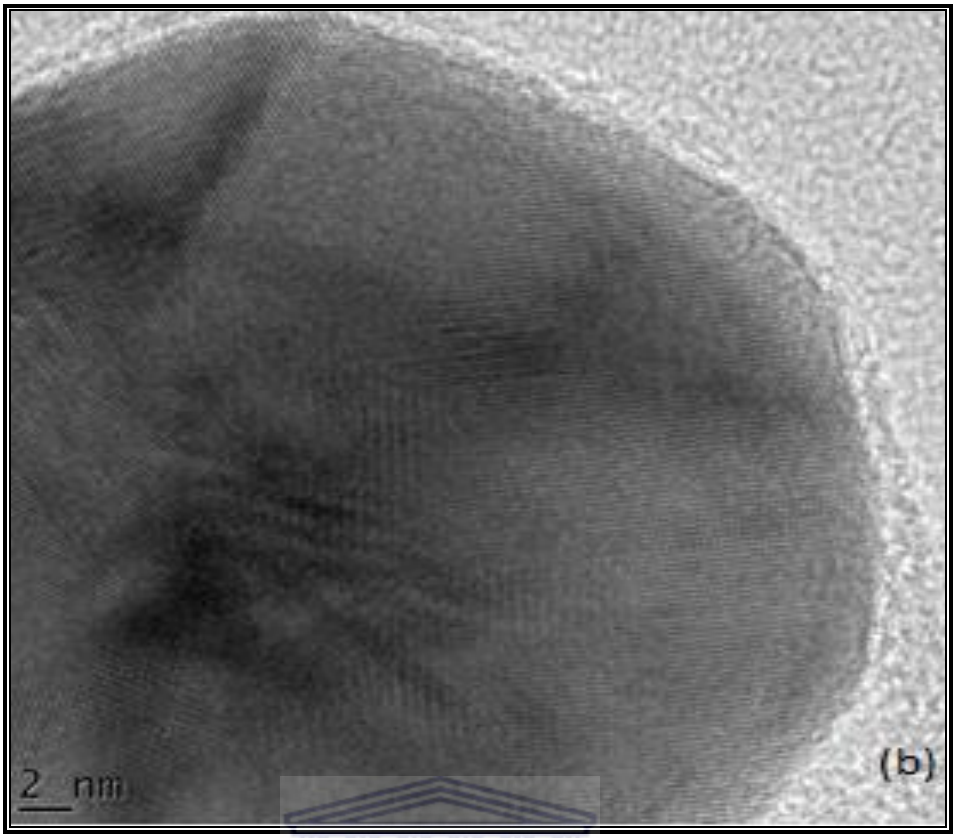

Figure 4.16: SAED (a) and lattice image (b) of Cu-Au nanocomposite

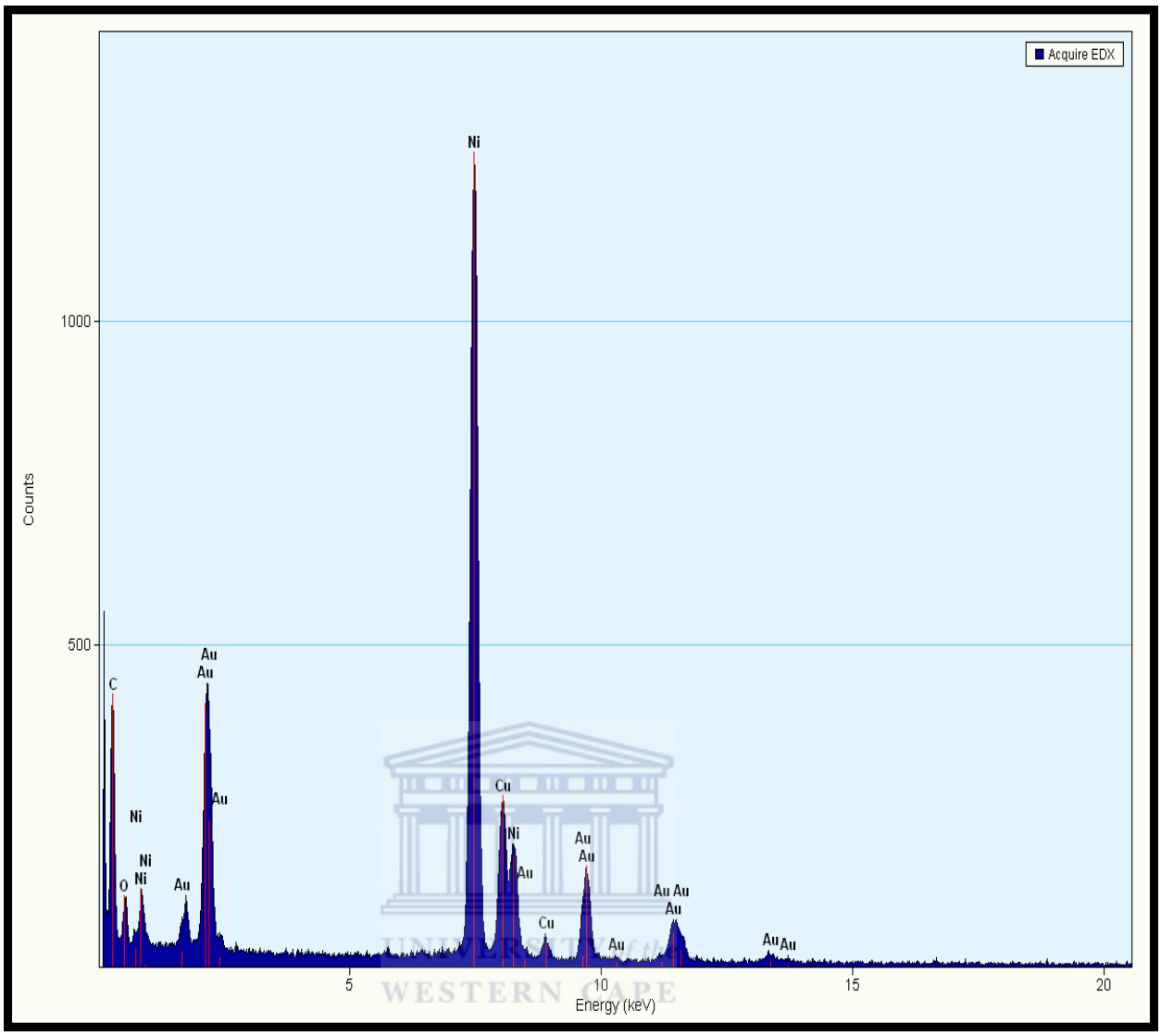

Figure 4.17: HRTEM Energy dispersive X-ray (EDX) of Cu-Au nanocomposite on a Nickel grid.

CHAPTER 5 : CHARACTERIZATION OF A NOVEL METALLIC LAYER Cu-Au NANOCOMPOSITE DOPED-$LiMn_2O_4$

5.1 Morphological Analysis and Electrochemical Characterization of a Novel Metallic Layer of Cu-Au Nanocomposite Doped $LiMn_2O_4$

5.1.1 High resolution scanning electron microscopy (HRSEM)

High resolution scanning electron microscopy (HRSEM) is a versatile imaging technique capable of producing three-dimensional images of material surfaces**.** HRSEM was used to determine the morphology, the particle size distribution and the elemental composition of Cu-Au nanocomposite-doped $LiMn_2O_4$. The crystallized size of the as prepared particles was calculated by use of the Scherrer's equation:

$$d=\frac{0.9\lambda}{B\cos\theta} \quad (9)$$

Where λ represents the wavelength, d is the mean crystallite in volume; B is the width at the maximum hump of the broadened diffraction peak. The high resolution image of Cu-Au nanocomposite doped-$LiMn_2O_4$ shows a well-developed octahedral structure with sharp edges and high crystallinity bounded by eight (111) planes with particles size ranging between 50-200 nm as seen in Figure 5.1 (Ying *et al*., 2001). In addition the Cu-Au nanocomposite appears as a tinny irregular shape, across the particles of pristine $LiMn_2O_4$. As it is known that, particles at the nanoscale have a large surface area, thus the Li^+ diffusion length could easily be reduce during the charge / discharge process which would lead to the improvement of the cathode material. Consequently, the incorporation of the Cu-Au nanocomposite would enhance the electrochemical performances of the cathode. For further confirmation of the composition of $Li[Cu\text{-}Au]_{0.02}Mn_{1.98}O_4$, EDX analysis was performed. But, with EDX analysis, it is not possible to detect the presence of lithium since it is outside the EDX detection range. The EDX results obtained, show that manganese appears at: Kα = 5.8951 KeV and Lα = 0.6374 whereas the oxygen appears at: Kα = 0.5249 KeV, gold at: Lα = 9.7135 KeV and Mα = 2.1205 KeV; finally copper appears at: Kα = 8.0413 KeV and Lα = 0.9297 KeV which agree with literature (Williams, 2001). EDX analysis thus reveals the evidence of the formation of $Li[Cu\text{-}Au]_{0.02}Mn_{1.98}O_4$ as seen on Figure 5.2 and Figure 5.3. Figure 5.2 shows that the highest peak intensity is observed for oxygen, followed by that of manganese and this is also noticed in the EDX of pristine $LiMn_2O_4$ (inset). This is due to the fact that the oxygen and manganese had the major composition during the synthesis. In the map of the selected area of $Li[Cu\text{-}Au]_{0.02}Mn_{1.98}O_4$ as seen in Figure 5.3, copper is in light blue colour, gold is in yellow, manganese is in green and oxygen is in red. Moreover, with regard to other

researchers results obtained in the surface modification of $LiMn_2O_4$, here no evident change in the surface modification of $LiMn_2O_4$ through doping with Cu-Au nanocomposite has been observed. Henceforth, HRTEM is done in order to ascertain if there is a doping layer of Cu-Au nanocomposite present.

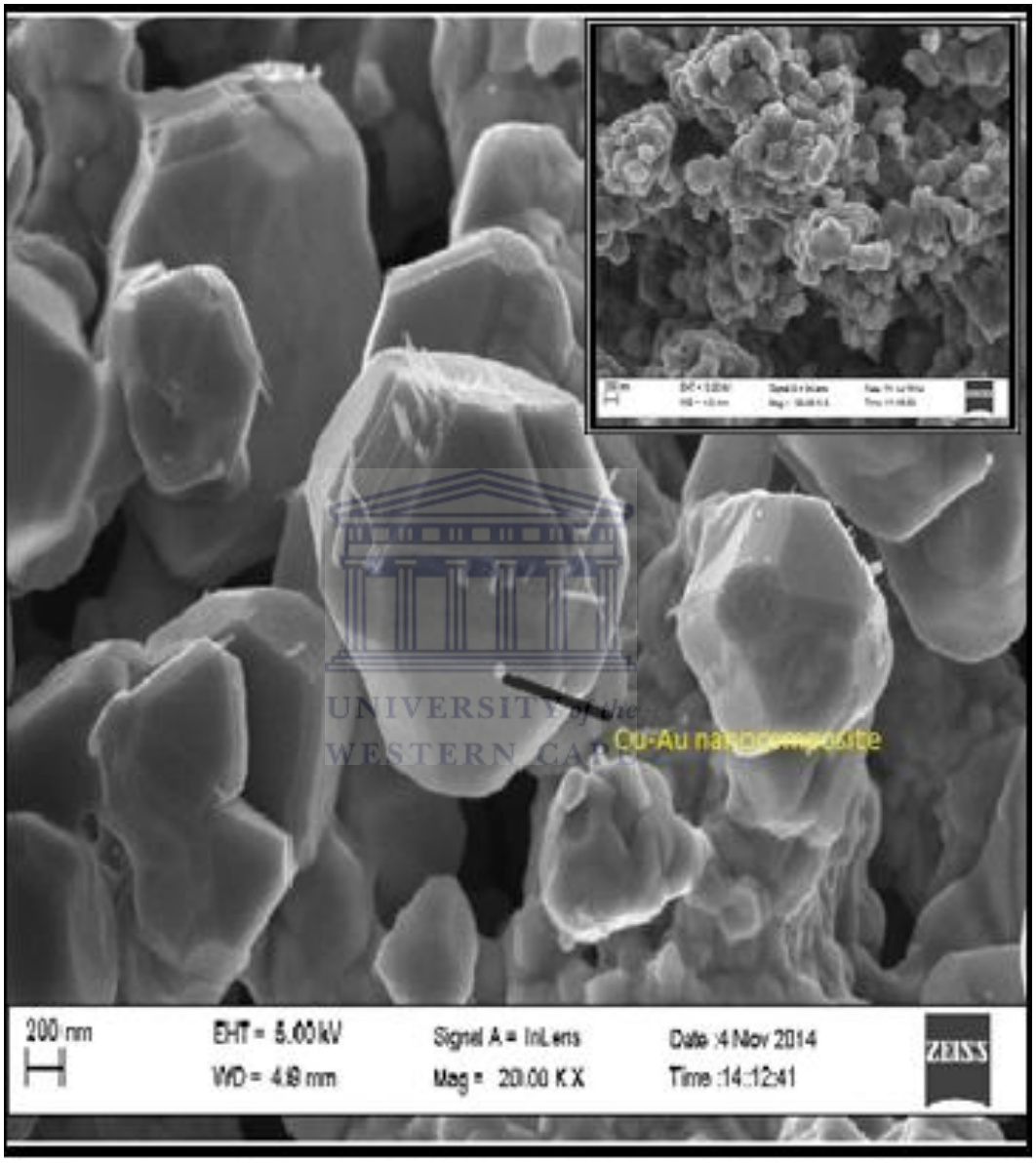

Figure 5.1: HRSEM images of doped $Li[Cu\text{-}Au]_{0.02}Mn_{1.98}O_4$ with HRSEM of pristine $LiMn_2O_4$ (inset)

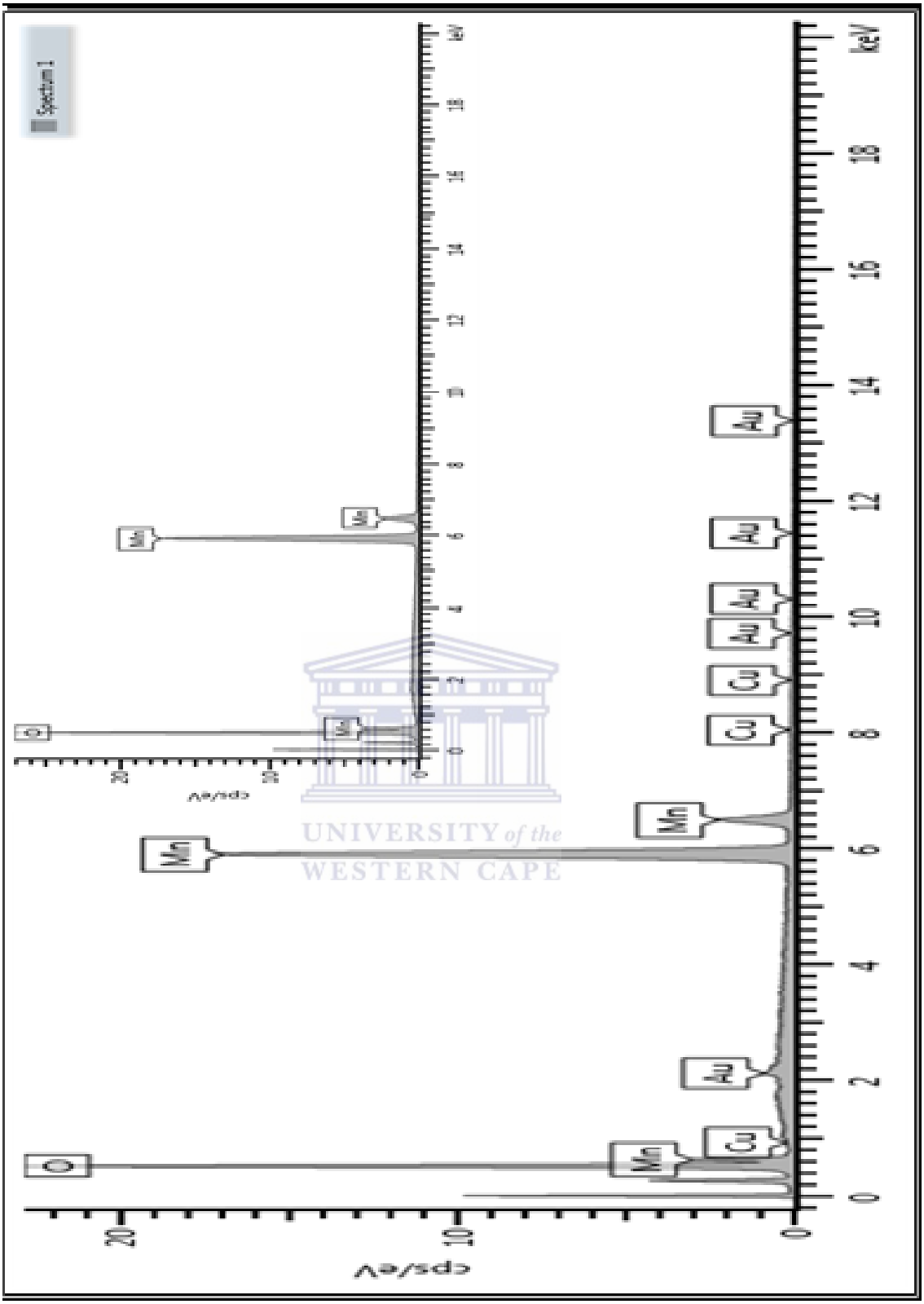

Figure 5.2: HRSEM Energy-dispersive X-ray (EDX) of a selected area of Li[Cu-Au]$_{0.02}$Mn$_{1.98}$O$_4$ on a nickel grid with EDX of pristine LiMn$_2$O$_4$ (inset)

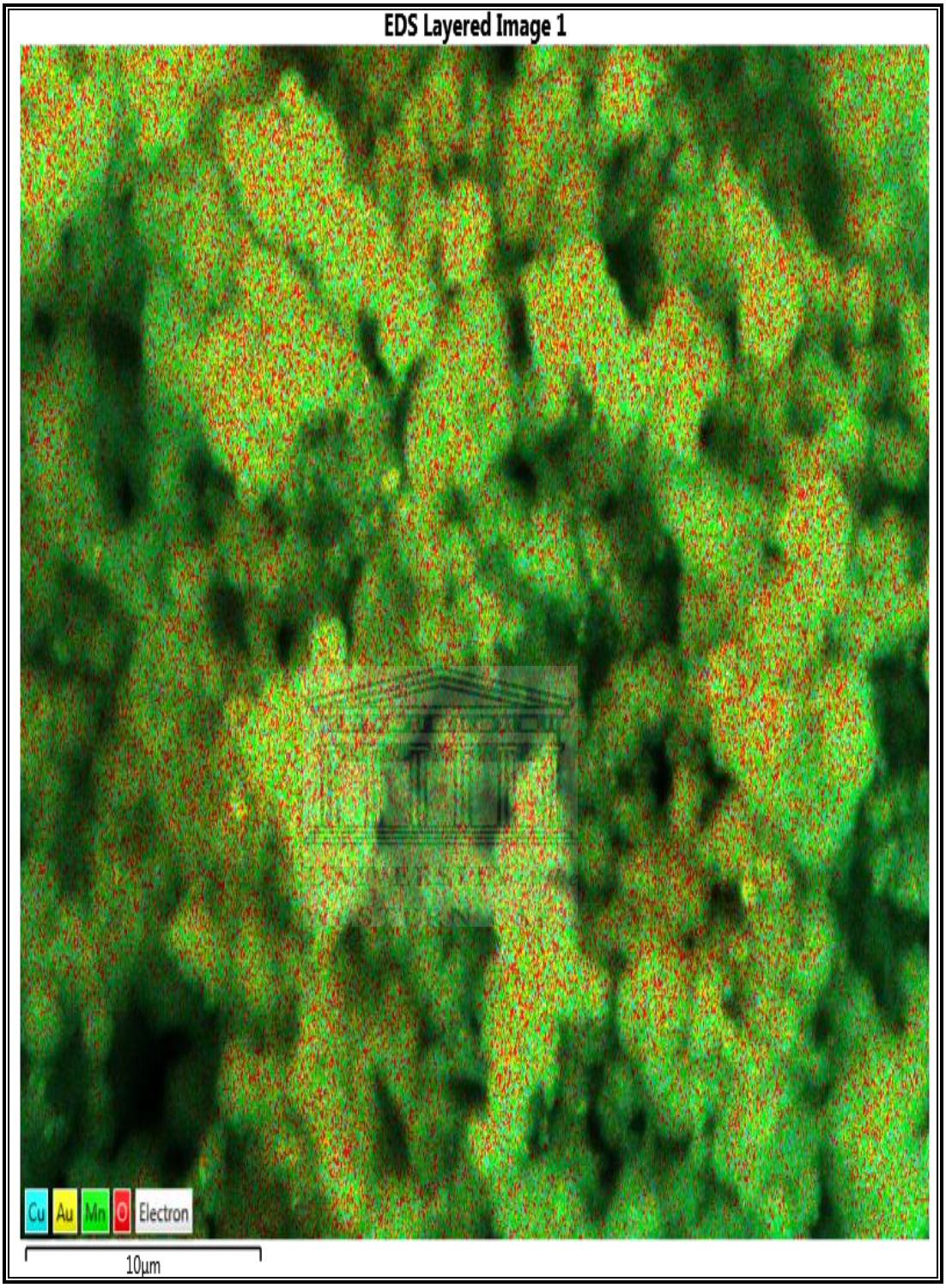

Figure 5.3: Map of a selected area of $Li[Cu\text{-}Au]_{0.02}Mn_{1.98}O_4$

5.1.2 High resolution transmission electron microscopy (HRTEM)

For a better understanding of the morphology as well as the nanostructure of the synthesized $Li[Cu\text{-}Au]_{0.02}Mn_{1.98}O_4$ cathode material, HRTEM observation was conducted on the material heat-treated at high temperature. Figure 5.4 shows a higher resolution image of $Li[Cu\text{-}Au]_{0.02}Mn_{1.98}O_4$ powder calcined at 880 ^oC for 15 h with HRTEM of Cu-Au nanocomposite (inset). The crystallite size of the powder prepared is around 20 -50 nm. Moreover, the obtained HRTEM reveals that the surface of $Li[Cu\text{-}Au]_{0.02}Mn_{1.98}O_4$ cathode powder is only doped with a thin layer of Cu-Au nanocomposite. Figure 5.5 shows the selected area electron diffraction of $Li[Cu\text{-}Au]_{0.02}Mn_{1.98}O_4$ corresponding to a hexagonal cubic- shape like nanoparticles with a size of around 50 nm. The particles appear to be well crystalline with a good dispersion which leads to a higher surface area which is in perfect conformity with xrd results obtained. Additionally, Figure 5.5 also discloses that Cu-Au nanocomoposite- doped $LiMn_2O_4$ has the same pattern zone of (111) as pristine $LiMn_2O_4$. Contrasting, other material used in the surface modification of pristine $LiMn_2O_4$ for instance, metal oxides or inorganic which would partly obstruct Li^+ from penetrating the doping layer into $LiMn_2O_4$. Here, $Li[Cu\text{-}Au]_{0.02}Mn_{1.98}O_4$ with nearly the similar structure as pristine $LiMn_2O_4$ might render the Li^+ pass over the Cu-Au nanocomposite doping layer more effortlessly. Based on the obtained result comparing with the one obtained for Cu-Au nanocomposite we can conclude that Cu-Au nanocomposite is present in the morphology of $Li[Cu\text{-}Au]_{0.02}Mn_{1.98}O_4$. Figure 5.6 displays the EDX obtained, which further confirms the presence of copper as well as that of gold.

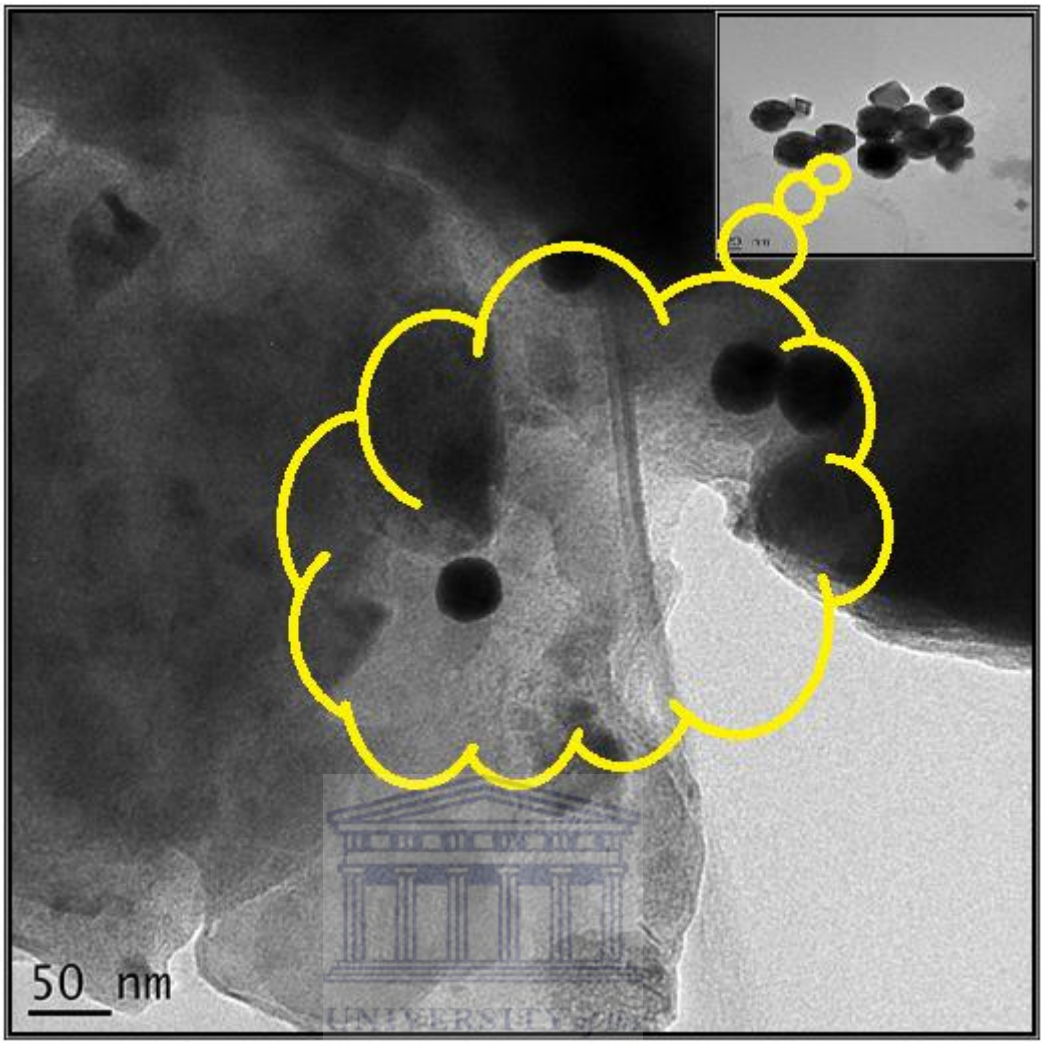

Figure 5.4: HRTEM of $Li[Cu\text{-}Au]_{0.02}Mn_{1.98}O_4$ with HRTEM of Cu-Au nanocomposite (inset)

Figure 5.5: SAED of a selected area of $Li[Cu\text{-}Au]_{0.02}Mn_{1.98}O_4$

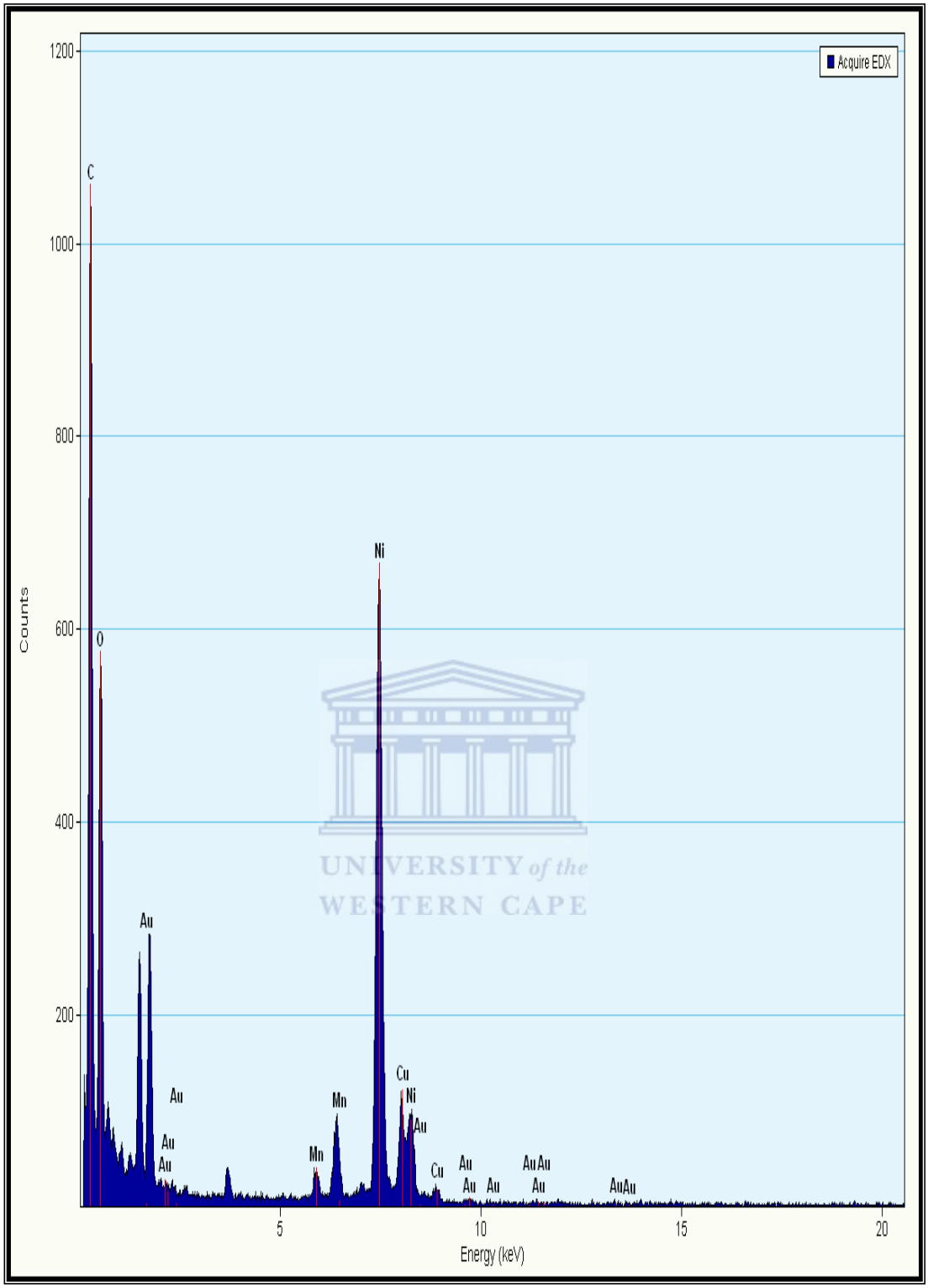

Figure 5.6: HRTEM Energy-dispersive X-ray (EDX) of $Li[Cu\text{-}Au]_{0.02}Mn_{1.98}O_4$

5.1.3 X-ray diffraction (XRD)

Figure 5.7 represents the X-ray diffraction (XRD) pattern of the as prepared Li[Cu-Au]$_{0.02}$Mn$_{1.98}$O$_4$ calcined at 880^{o}C for 15 h. From the XRD below, we notice an increase in peak intensity in Li[Cu-Au]$_{0.02}$Mn$_{1.98}$O$_4$ as compared to the XRD pattern obtained of LiMn$_2$O$_4$. This suggests an increase in crystallinity which is in perfect agreement with the HRSEM results obtained. Moreover no change was observed on the lattice parameter of the modified LiMn$_2$O$_4$. It has been concluded that LiMn$_2$O$_4$ hasn't changed its structure after surface modification using Cu-Au nanocomposite. The obtained result is also confirmed by the HRSEM results. However, we found some closeness in diffraction peaks for copper and gold which are indexed with respect to the Joint Committee Powder Diffraction Standards (JCPDS: 0004-0784) and (JCPDS: 04-0836) cards respectively.

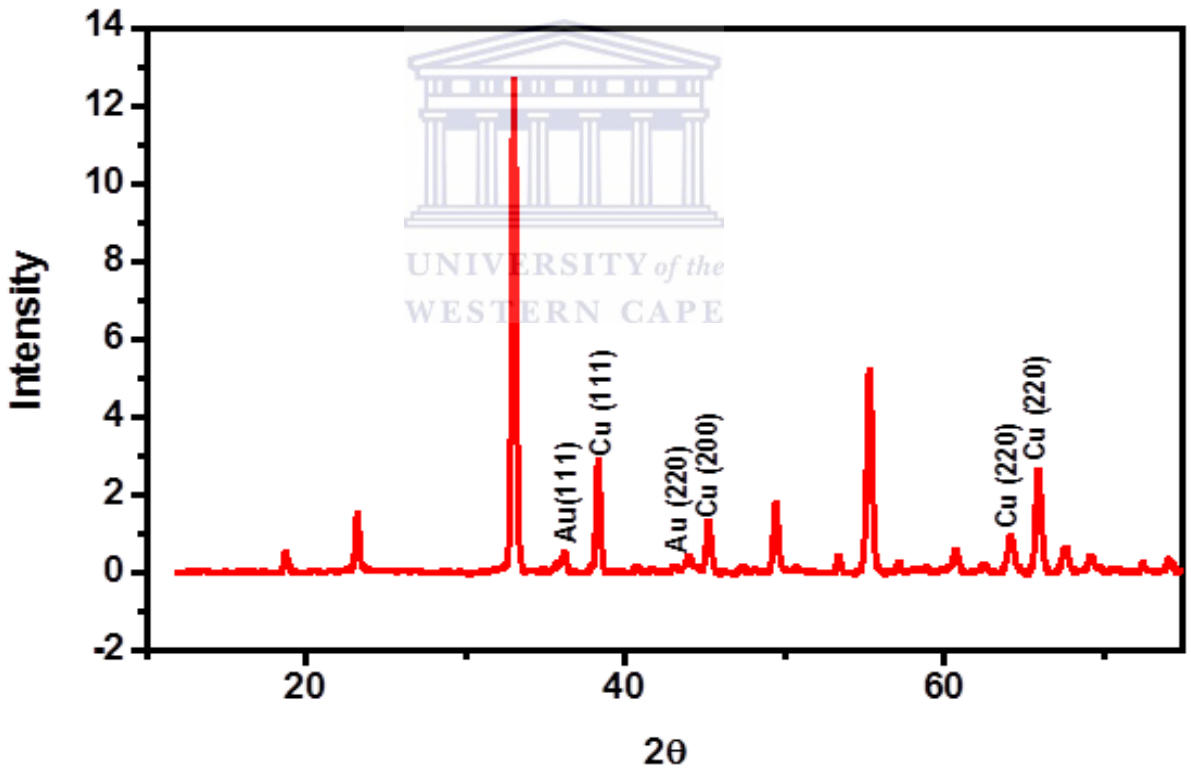

Figure 5.7: XRD pattern of Li[Cu-Au]$_{0.02}$Mn$_{1.98}$O$_4$ calcined at 880^{o}C for 15 h with an increase in peak intensity.

5.1.4 Fourier-transform infra-red (FTIR)

FTIR spectroscopy is painstaking to be an active tool in solid-state chemistry because it delivers information on the structural environment of inorganic solids. The FTIR spectra of the pristine $LiMn_2O_4$ as well as that of a novel metallic layer Cu-Au nanocomposite doped-$LiMn_2O_4$ calcined at 880 ^oC are represented by Figure 5.8 in the wave number range of 500 - 4000 cm^{-1}. The bands observed in the range of 500 -600 cm^{-1} are characteristics of manganese-oxygen (Mn-O) vibration peaks and mirrors the structural environment of MnO_6 octahedral responsible for the formation of $LiMn_2O_4$ (Raja *et al.*, 2009). Moreover no additional frequency band was observed for copper and gold. Based on XRD results gotten for this MSc research work, $LiMn_2O_4$ preserved its structure after surface modification through doping of Cu-Au nanocomposite the same is observed in the FTIR spectra of $Li[Cu\text{-}Au]_{0.02}Mn_{1.98}O_4$, as no much change is observed in the spectra but only a change in peak intensities. Consequently, it is suggested that Cu-Au nanocomposite didn't diffuse into the whole cathode material but only on the surface of $LiMn_2O_4$ powder.

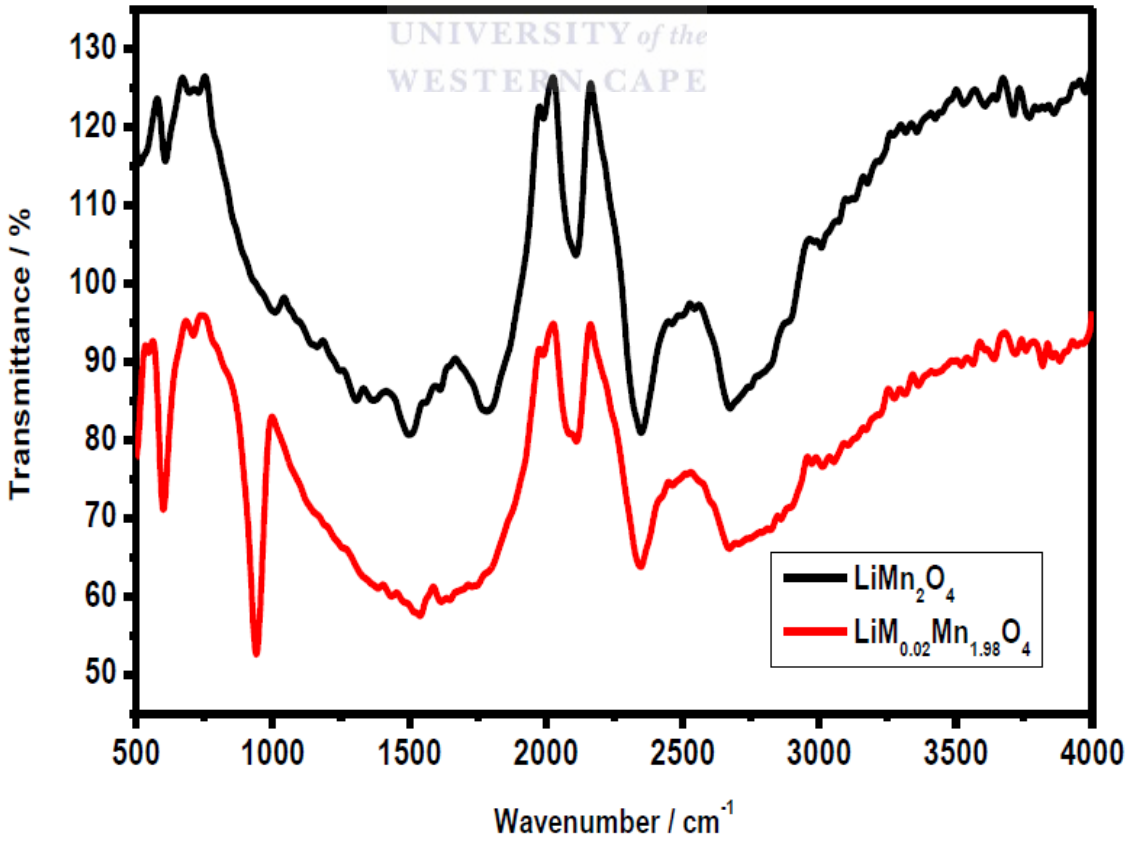

Figure 5.8: FTIR spectra for $LiMn_2O_4$ and $Li[Cu\text{-}Au]_{0.02}Mn_{1.98}O_4$

5.2 Electrochemical Characterization of Novel Metallic layer of Cu-Au nanocomposite doped- $LiMn_2O_4$

5.2.1 The effects of electrochemical parameters obtained from the CV of $LiMn_2O_4$ and $LiM_xMn_{2-x}O_4$ at 9 mV / s in 1 M Li_2SO_4

Table 4 below displays the electrochemical parameters that contribute toward the redox reaction taking place at the anode and cathode. The peak separation (ΔE_p) for the synthesized $LiMn_2O_4$ and the novel $Li[Cu\text{-}Au]_{0.02}Mn_{1.98}O_4$ are 887 mV and -88 mV respectively. The least peak separation was obtained for $Li[Cu\text{-}Au]_{0.02}Mn_{1.98}O_4$. Thus, it is concluded that $Li[Cu\text{-}Au]_{0.02}Mn_{1.98}O_4$ has a more reversible behaviour than the pristine $LiMn_2O_4$. Moreover, the peak separation values for both are larger than the ideal condition where $\Delta E_p = 0$. This implies that Mn^{3+} / Mn^{4+} reaction is controlled by the insertion / deinsertion of Li^+ in the cathode materials. Consequently, the least ΔE_p would shorten the Li-ion path responsible for the faster reaction. This is due to the presence of Cu-Au nanocomposite in the cathode material leading to the decrease in peak separation ($\Delta E_{p)}$ from 887 to -88 mV. The broadening in peak is more obvious in pristine $LiMn_2O_4$ than in $Li[Cu\text{-}Au]_{0.02}Mn_{1.98}O_4$ as observed in Figure 5.9 and Figure 5.10. This is due to the fact that $LiMn_2O_4$ has a reduced surface and with an elongated diffusion path of Li^+.

Table 4: Electrochemical parameters from CV for $LiMn_2O_4$ and $Li[Cu\text{-}Au]_{0.02}Mn_{1.98}O_4$

Cathode materials	E_{pa1} (mV)	E_{pc1} (mV)	ΔE_{p1} (mV)	I_{pa1} / I_{pc1} (µA)	E_{pa2} (mV)	E_{pc2} (mV)	ΔE_{p2} mV	I_{pa2} / I_{pc2} (µA)
$LiMn_2O_4$	177	-710	887	0.66				
$LiM_xMn_{2-x}O_4$	-180	-92	-88	0.45	192	153	39	2

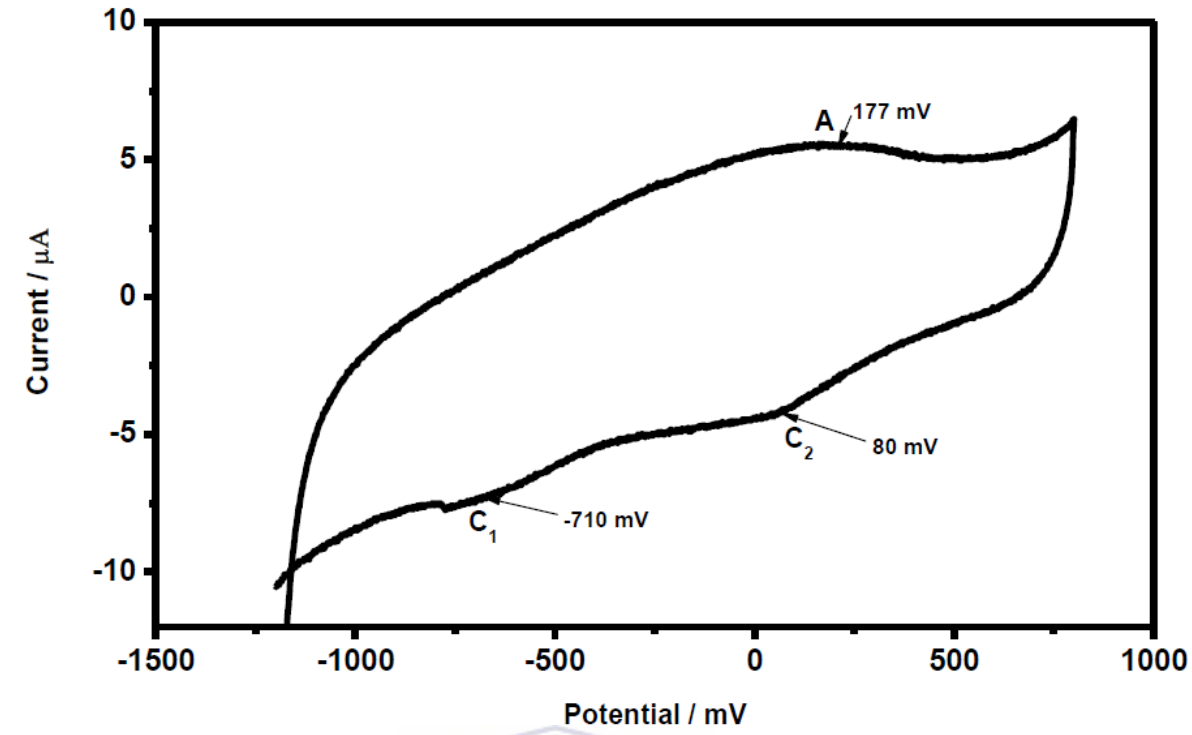

Figure 5.9: Cyclic voltammogram of $LiMn_2O_4$/GCE 1 M Li_2SO_4

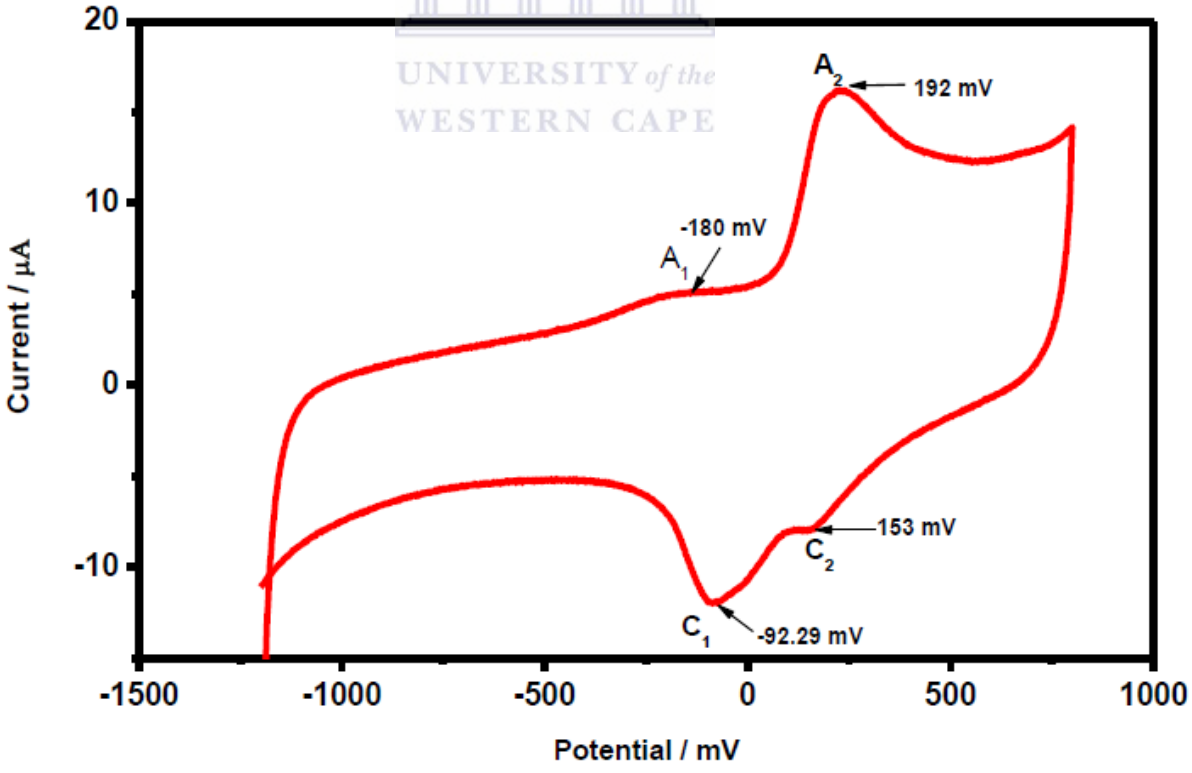

Figure 5.10. Cyclic voltammogram of $Li[Cu\text{-}Au]_{0.02}Mn_{1.98}O_4$/GCE in 1 M Li_2SO_4

5.2.2 Redox reaction analysis

The active cathode material of a secondary lithium-ion battery is a host compound, where lithium ions can be inserted and extracted reversibly during the cycling process. In the last few years, the use of nanomaterials for Li-ion cathodes instead of conventional materials has become very attractive to perk up the performance of lithium rechargeable batteries. Several groups have shown that nanosized materials are emerging as successful solutions to enhance rate capability and cyclic stability of these electrodes (Sides *et al*., 2005, Odani *et al*., 2003, Curtis *et al*., 2004).

In this present work, the cyclic voltammogram results of a glassy carbon electrode (GCE) in 4 µL of $LiMn_2O_4$ and $LiMn_{0.02}Mn_{1.98}O_4$) heated at 880^{o}C for 15 h.

Figure 5.11, shows an increase in current as the scan rate is increased. Even though, it has been reported that the stability as well as the insertion / extraction of Li^+ takes place in two steps (Gummow *et al*., 1994). Nevertheless in this present study not such two distinct peaks during oxidation and reduction were observed for $LiMn_2O_4$ except for $Li[Cu\text{-}Au]_{0.02}Mn_{1.98}O_4$.

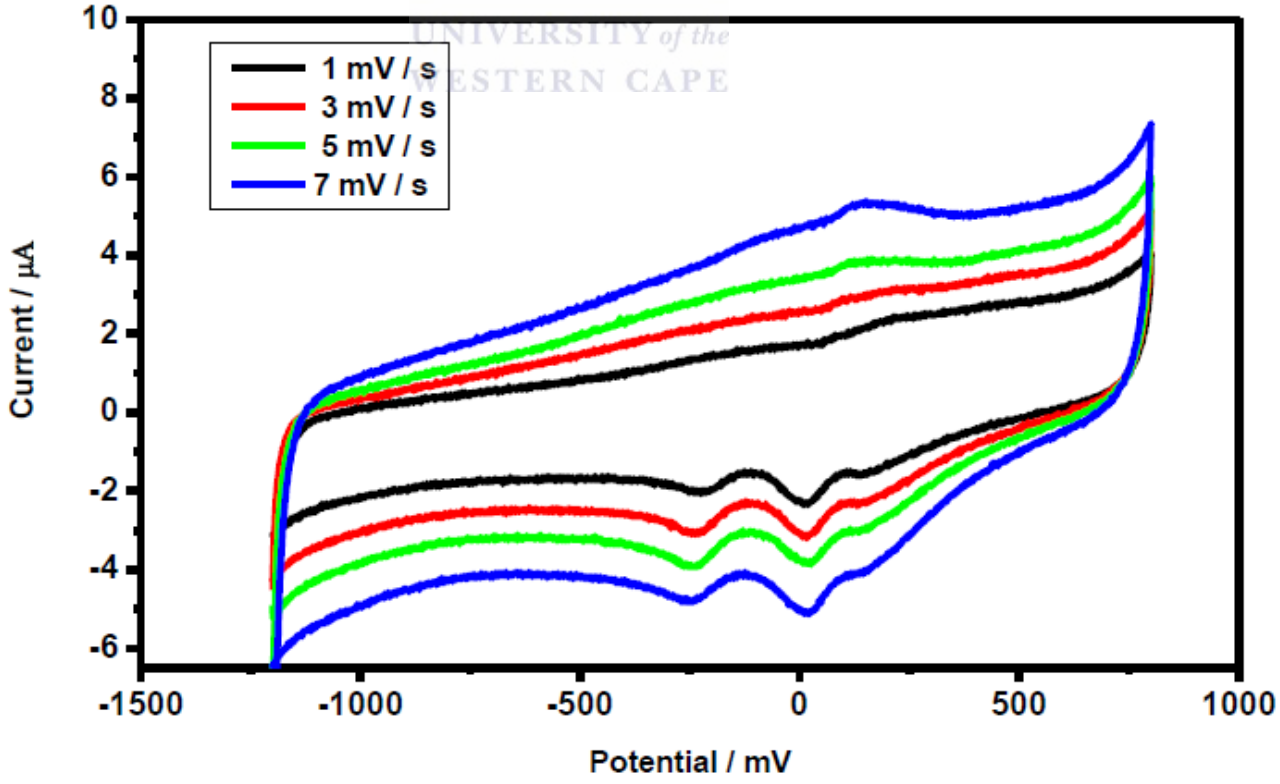

Figure 5.11: Cyclic Voltammograms of $Li[Cu\text{-}Au]_{0.02}Mn_{1.98}O_4$/GCE in 1 M Li_2SO_4 at different scan rate.

Additionally, the broadened peak in $LiMn_2O_4$ as seen in Figure 5.12 shows that the process takes place in two steps. Similar result was reported by a researcher (Rao *et al*., 2001). The cyclic voltammogram of $Li[Cu\text{-}Au]_{0.02}Mn_{1.98}O_4$ shows two pairs of redox peaks. This is attributed to the insertion / deinsertion of lithium ion at $Li[Cu\text{-}Au]_{0.02}Mn_{1.98}O_4$. Equation 10 is a typical characteristic attributed to the deintercalation process of Li ion in 8a tetrahedral sites of $LiMn_2O_4$ spinel (Kamarulzaman *et al*., 2009).

$$LiMn_2O_4 \leftrightarrow Li_{1-x}Mn_2O_4 + xLi^+ + xe^- \quad (10)$$

The first peak C_1 is attributed to the removal of lithium ions from the tetrahedral sites where Li–Li interactions occur, whereas the second peak C_2 is attributed to the removal of lithium ions again from the tetrahedral sites but where Li–Li interaction does not occur. However, the cathode material doped with Cu-Au nanocomposite $Li[Cu\text{-}Au]_{0.02}Mn_{1.98}O_4$ show more than 2.5 times higher peak current than pristine $LiMn_2O_4$ in all corresponding peaks. The peaks for the $LiM_xMn_{2-x}O_4$ are sharper than those of pristine $LiMn_2O_4$. The sharpness in peak in the $Li[Cu\text{-}Au]_{0.02}Mn_{1.98}O_4$ votltammogram suggests that, electrochemical reaction is complete at a shorter period of time which is in perfect agreement with the EIS results obtained in Figure 5.15. On one hand, the sharpness in the peak in $Li[Cu\text{-}Au]_{0.02}Mn_{1.98}O_4$ also indicates an easier ion transfer which leads to an improvement of the reaction kinetics. The diffusion coefficient was calculated, and found to be $1.90\times10^{-3}\,cm^2s^{-1}$ and $6.90\times10^{-3}\,cm^2s^{-1}$ for $LiMn_2O_4$ and $Li[Cu\text{-}Au]_{0.02}Mn_{1.98}O_4$ respectively. On the other hand, the sharper peak also implies that the deintercalation process of Li ion can take place at a speedy rate. Furthermore, the cathode material $Li[Cu\text{-}Au]_{0.02}Mn_{1.98}O_4$ with Cu-Au nanocomposite incorporated have a larger interface area which provides additional lithium ions for diffusion which need to travel a shorter path inside the particle than in $LiMn_2O_4$, leading to the high ion exchange current as obtained in EIS. In addition, during the discharge process, small particles can provide more interfacial region for contact within the liquid electrolyte and can consequently increase the opportunity for lithium ions to intercalate back into the host structure, resulting in a higher Coulombic efficiency as was calculated in this work, the value found is 50 % and 59 % for $LiMn_2O_4$ and $Li[Cu\text{-}Au]_{0.02}Mn_{1.98}O_4$ respectively (Yi *et al*., 2007). In addition the decrease in peak in the 100 mV region implies that the presence of Mn^{3+} but in a small amount which would not appear at very low scan rate (Lu *et al*., 2001, Paulsen *et al*., 2000). This leads us to presume that manganese was in its 4+ oxidation state (Saıdi *et al*., 2003). Consequently, we can say that the modification of $LiMn_2O_4$ surface through doping has an improvement in the electrochemical activity of pristine $LiMn_2O_4$.

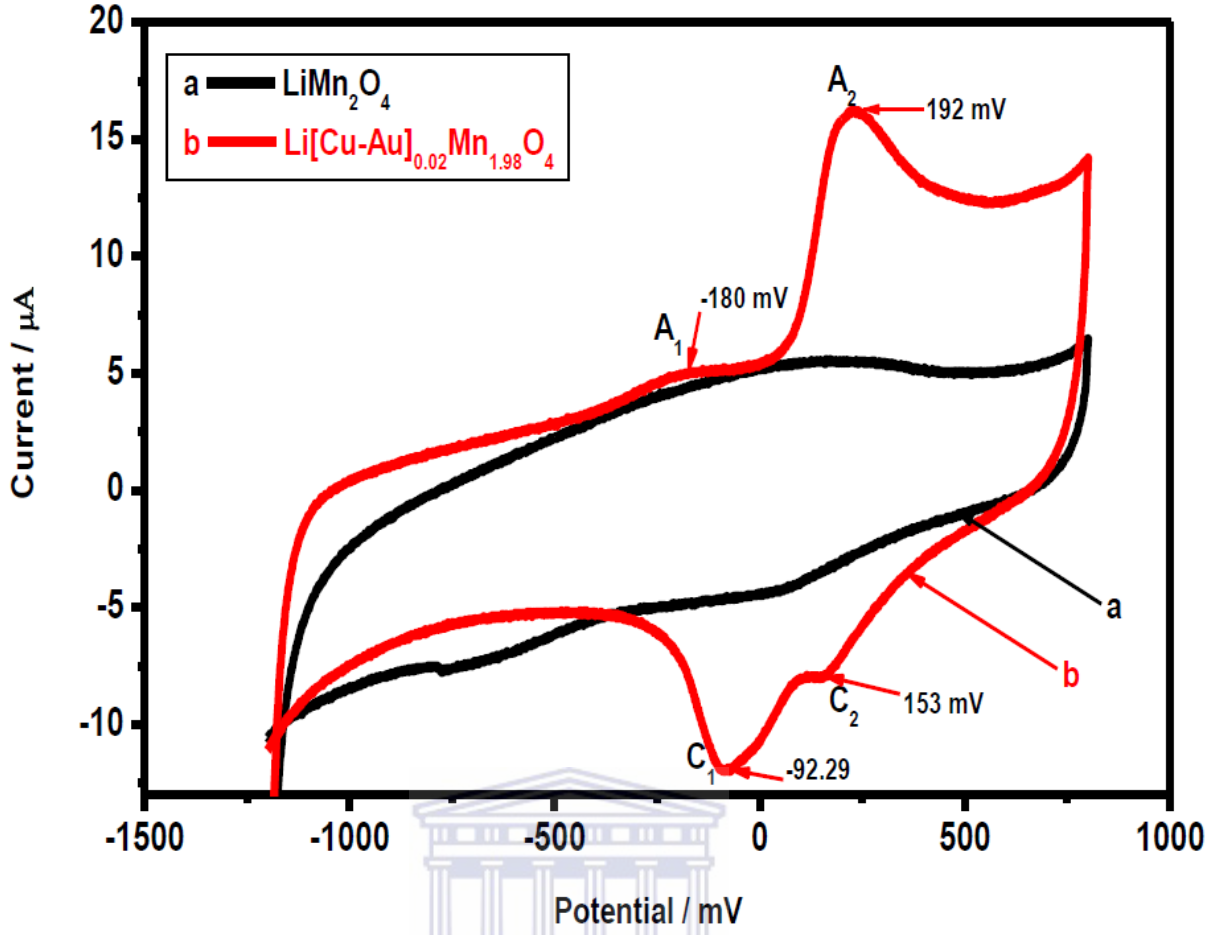

Figure 5.12: Cyclic voltammograms of $LiMn_2O_4$/GCE and $Li[Cu\text{-}Au]_{0.02}Mn_{1.98}O_4$/GCE in 1 M Li_2SO_4 at 9 mV / s

Table 5 displays value obtained for the discharge of $LiMn_2O_4$ and $Li[Cu\text{-}Au]_{0.02}Mn_{1.98}O_4$ at scan rate 9 mV / s which is 120 mAh / g and 153 mAh /g respectively. But, the theoretical value of $LiMn_2O_4$ is 148 mAh / g as reported by some researchers (Yi *et al.*, 2007). Henceforth, our novel $Li[Cu\text{-}Au]_{0.02}Mn_{1.98}O_4$ exhibited better electrochemical performance additionally a decrease in the dissolution of Mn^{2+} in electrolyte is noticed. The following steps were used to calculate the capacities of $LiMn_2O_4$ and that of $Li[Cu\text{-}A]_{0.02}Mn_{1.98}O_4$. After the integration of the selected area of the reduction peak of $LiMn_2O_4$, the value obtained is $4.66\times10^{-5}AV$.

Knowing that charge $$Q=\frac{\text{Area}\,(AV)}{\text{Scan Rate}\,(V/S)} \tag{11}$$

Hence $$Q=\frac{4.66\times10^{-5}AV}{9\times10^{-3}\,(V/S)} \tag{12}$$

$$Q = 5.17\times10^{-3}AV \tag{13}$$

The unit of battery for capacity are in Amper hour (Ah), since 3600s = 1h, hence 3600 As = 1Ah

Thus,

$$Q = \left(\frac{5.17 \times 10^{-3}}{3600} \right) Ah \quad (14)$$

$$Q = 1.43 \times 10^{-6} Ah \quad (15)$$

The specific capacity of the battery is then obtained by dividing the capacity by the active mass used on the surface of the electrode. The amount of $1.2 \times 10^{-5} g$ was used.

Consequently,

$$\text{Discharge Specific Capacity} = \frac{Q(Ah)}{\text{Active Mass}(g)} \quad (16)$$

$$\text{Discharge Specific Capacity} = \frac{1.43 \times 10^{-6} \times 1000}{1.2 \times 10^{-5}} \quad (17)$$

$\text{Discharge Specific Capacity} = 120\,mAh/g$, the same method was used to calculate the capacities of charge / discharge of the others. The obtained results are in the table below (Martin, 2013).

Table 5: The obtained values of Charge / Discharge capacity

Cathode Materials	Charge / mAh / g	Discharge / mAh / g	η* / %
$LiMn_2O_4$	**39.16**	**120**	**50**
$LiM_xMn_{2-x}O_4$	**263,04**	**153.61**	**59**

* **η** value was calculated with the equation: $\eta = \frac{\text{Discharge capacity}}{\text{Charge capacity}} \times 100\%$ (17)

5.2.3 Electrochemical impedance spectroscopy (EIS)

Electrochemical impedance spectroscopy (EIS) studies were performed on fresh cells from 100 mHz - 100KHz of the $LiMn_2O_4$ and $Li[Cu\text{-}Au]_{0.02}Mn_{1.98}O_4$ cathodes materials.

Usually, the impedance curves of $LiMn_2O_4$ display two partially overlapped semi-circles in the high and medium frequency regions and an inclined line in the low frequency region. Where, the first semi-circle at higher frequency is related to the formation of a passivation film on the surface and the second semi-circle at lower frequency is attributed to the Li^+ charge transfer at the interface (Mohamedi *et al*., 2001). But, not such two semi-circles are observed in this present MSc research work. This may be attributed to the frequency window used during the experiment, as the frequency window ranged between 100 mHz – 100 KHz. The obtained data is in agreement with literature (Zhao *et al*., 2012).

Figure 5.13 represents the Nyquist plot of the pristine $LiMn_2O_4$ and $Li[Cu\text{-}Au]_{0.02}Mn_{1.98}O_4$. The low frequency straight line seen can be associated with Li^+ ion diffusion in the bulk of the electrode. A well-defined semicircle at high frequency which is attributed to the complex charge transfer processes from the electrolyte to the electrode material. It is known that the Rct refers to the charge transfer resistance, and in this case it's an elevated resistance in the high frequency region and is associated with the Li^+ ion transfer process at the electrode–electrolyte interface (Wang *et al*., 2005, Yi *et al*., 2007). The diffusion rate of Li^+ in the electrolyte solution is far greater than that of Li^+ in solid-state active material, thus the charge transfer resistance can be considered as the rate-determining step of the diffusion process of Li^+ during the charge / discharge of the battery. Moreover, from the Nyquist plot it can be concluded that $LiMn_2O_4$ is less catalytic than $Li[Cu\text{-}Au]_{0.02}Mn_{1.98}O_4$. This means that the electron transfer is slow in $LiMn_2O_4$, hence a higher value obtained for the resistance charge transfer (Rct) and time constant (τ) for $LiMn_2O_4$ compared to that obtained for $Li[Cu\text{-}Au]_{0.02}Mn_{1.98}O_4$.

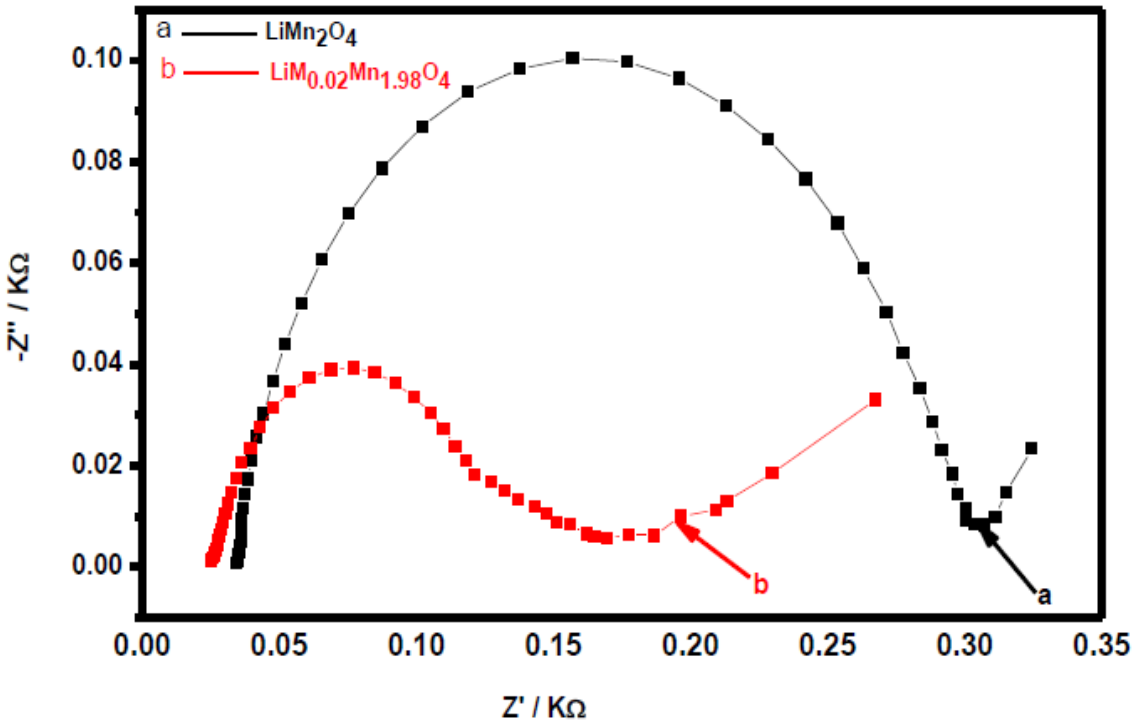

Figure 5.13: Nyquist plot of $LiMn_2O_4$ (a) and $Li[Cu\text{-}Au]_{0.02}Mn_{1.98}O_4$ with perturbation amplitude of 9 mV / s

Figure 5.14 displays the equivalent circuit obtained from fitting the data using ZView software. Where R_S is the effective resistance due to electrolyte impedance and electrical contacts and is obtained from the intercept of the semicircle at a high frequency with the x-axis. W_s is the Warburg impedance seen as a slope in the low frequency regime, Cdl is double layer capacitance of a solid electrolyte interphase (SEI) represented by CPE (constant phase element).

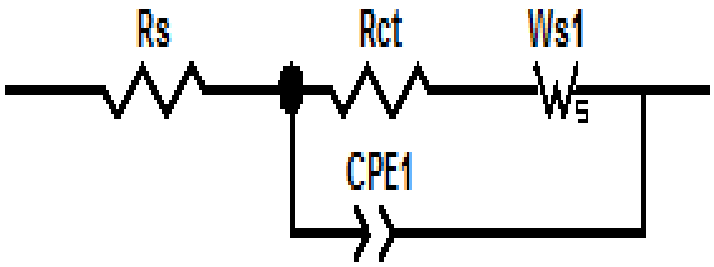

Figure 5.14: The model circuit obtained for $LiMn_2O_4$ and $Li[Cu\text{-}Au]_{0.02}Mn_{1.98}O_4$

Table 6 displays the kinetics parameters obtained from EIS for $LiMn_2O_4$ and $Li[Cu\text{-}Au]_{0.02}Mn_{1.98}O_4$. The resistance charge transfer (Rct) obtained for $Li[Cu\text{-}Au]_{0.02}Mn_{1.98}O_4$ was much lower, the decrease in charge resistance transfer implies the Li ion diffusion is enhanced in the Cu-Au nanocomposite modified $LiMn_2O_4$ more than in the pristine $LiMn_2O_4$. In addition, the largest Rct value of 201 Ω is observed for $LiMn_2O_4$ indicating that it has largest electrochemical polarization which results in relatively lower electrochemical performance. Additionally, the minimum Rct value of 14,18 Ω was obtained for $LiM_xMn_{2-x}O_4$ which implies that it has the lowest electrochemical polarization, and this leads to higher cycle performance. The increase in exchange current (I_o) obtained in $Li[Cu\text{-}Au]_{0.02}Mn_{1.98}O_4$ and the decrease in impedance suggest an increase in the rate of electron transfer compared to the pristine $LiMn_2O_4$. Furthermore, the double layer capacitance (Cdl) value for $LiMn_2O_4$ and $Li[Cu\text{-}Au]_{0.02}Mn_{1.98}O_4$ is 0.892 µF and 131.5 µF respectively. The increase in double layer capacitance (Cdl) in $Li[Cu\text{-}Au]_{0.02}Mn_{1.98}O_4$ proves that $Li[Cu\text{-}Au]_{0.02}Mn_{1.98}O_4$ has a higher surface area than $LiMn_2O_4$ which is ascribed to the surface modification of $LiMn_2O_4$ through doping of Cu-Au nanocomposite.

Table 6: Kinetics parameters of $LiMn_2O_4$ and $LiM_xMn_{2-x}O_4$ obtained from electrochemical impedance spectroscopy at 298 K

Cathode Materials	I_o / A	R_{ct} / Ω	K_{et} / cm s^{-1}	τ / s $rand^{-1}$	σ / $Ω^{-1/2}$	D./ cm^2 s^{-1}
$LiMn_2O_4$	1.28 x10^{-4}	201	1.86 x10^{-3}	9 x10^{-4}	11.73	1.90 x10^{-3}
$LiM_xMn_{2-x}O_4$	1.73 x10^{-3}	14.18	2.52 x10^{-4}	3.8 x10^{-4}	6.5	6.09 x10^{-3}

From the Bode plot in Figure 5.15, it can be seen that there is a shift towards higher frequency as the flow of electrons is faster. This is accredited to the decrease in time constant (τ) found to be 3 x 10^{-4} s $rand^{-1}$ for $Li[Cu\text{-}Au]_{0.02}Mn_{1.98}O_4$ and 9 x 10^{-4}s $rand^{-1}$ for $LiMn_2O_4$. Current exchange (I_o), heterogeneous rate transfer of electron (K_{et}), the constant time (τ), the angular frequency at maximum imaginary impedance of the semi-circle (ω_{max}) and the lithium ion diffusion coefficients (D) were all calculated from:

$$\tau = \frac{1}{\omega_{max}} \qquad (18)$$

$$R_{ct} = \frac{RT}{nFI_0} \tag{19}$$

$$I_0 = nFAK_{et}C \tag{20}$$

$$K_{et} = \frac{I_0}{nFAC} \tag{21}$$

$$\sigma = \left(R_s - R_{ct}\right)\omega^{\frac{1}{2}} \tag{22}$$

R is the gas constant = 8.314 l / mol K, T is the room temperature = 289 K, n is the number of Lithium ion transfer, F is the faraday constant = 96485 C / mol and A represents the area of the electrode as for this work glassy carbon electrode with area of 0.071 cm^2 (Bard and Faulkner, 1980). The Warburg coefficient σ is defined by the following equation (Bard and Faulkner, 1980):

$$\sigma = \frac{RT}{\sqrt{2}\, n^2F^2A}\left(\frac{1}{D_o^{1/2}C_o} + \frac{1}{D_r^{1/2}Cr}\right) \tag{23}$$

Let assume that $D_o = D_r = D$, the above equation becomes:

$$\sigma = \frac{RT}{\sqrt{2}n^2F^2A}\left(\frac{1}{\sqrt{DC}} + \frac{1}{\sqrt{DC}}\right) \tag{24}$$

$$\frac{1}{\sqrt{DC}} + \frac{1}{\sqrt{DC}} = \frac{\sigma\sqrt{2}n^2F^2A}{RT} \tag{25}$$

$$\frac{2\sqrt{D}}{DC} = \frac{\sigma\sqrt{2}n^2F^2A}{RT} \tag{26}$$

By squaring both sides we get:

$$\left(\frac{2\sqrt{D}}{DC}\right)^2 = \left(\frac{\sigma\sqrt{2}n^2F^2A}{RT}\right)^2 \tag{27}$$

$\left(\sqrt{2}\right)^2 = 2$, thus the equation becomes (28)

$$\frac{4D}{D^2C^2} = 2\left(\frac{\sigma n^2F^2A}{RT}\right)^2 \tag{29}$$

$$\frac{2}{DC^2} = \left(\frac{\sigma n^2 F^2 A}{RT}\right)^2 \tag{30}$$

$$\text{Hence } D = \frac{2(RT)^2}{\left(\sigma n^2 F^2 A\right)^2} \tag{31}$$

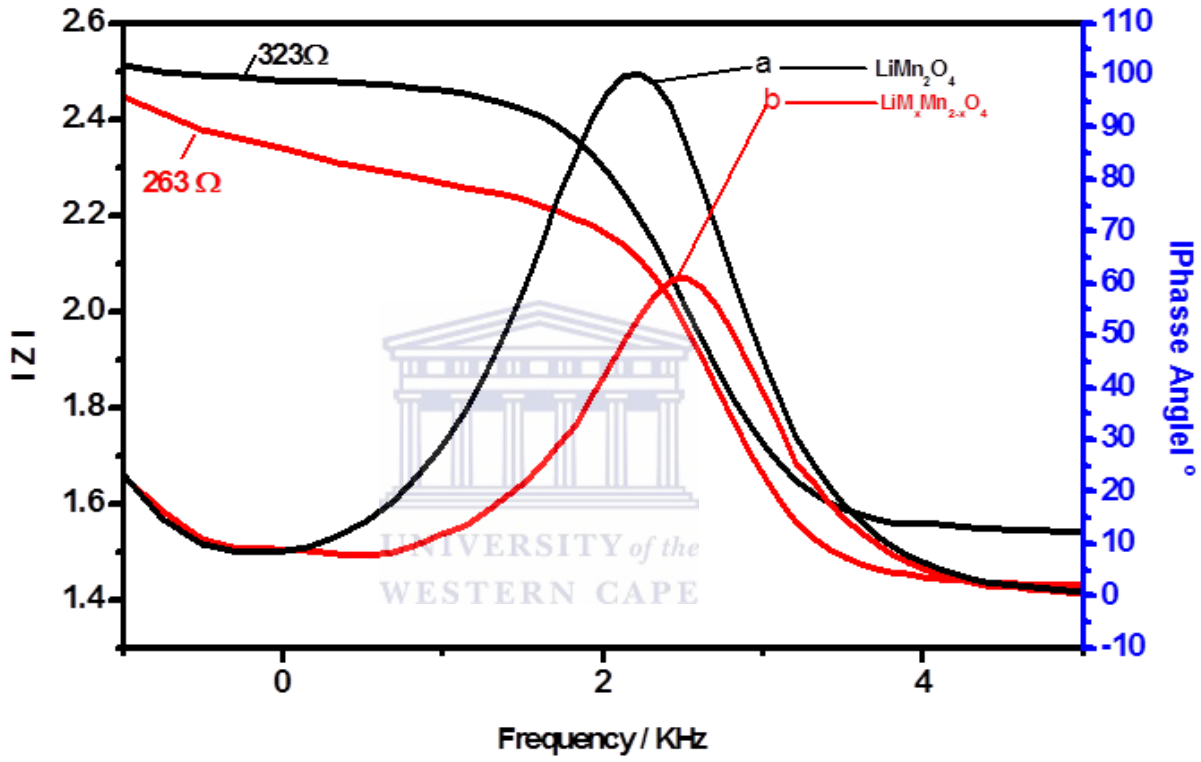

Figure 5.15: The Bode plot of $LiMn_2O_4$ (a) and $Li[Cu\text{-}Au]_{0.02}Mn_{1.98}O_4$ (b) with perturbation amplitude of 10 mV

CHAPTER 6 : CONCLUSION AND RECOMMENDATIONS

6.1 Conclusion

The energy problem faced today has led many researchers to the quest for new alternative sources of energy which are environmental friendly, cost effective and non-toxicity. $LiMn_2O_4$ has proven to be the ideal cathode material for Li-ion batteries as it meets these requirements but due to its disadvantages such as: the (1) the Jahn–Teller distortion caused by Mn^{3+} would lead to the degradation of cyclability in $LiMn_2O_4$ during the Li^+ intercalation and de-intercalation, (2) dissolution of manganese into the electrolyte and decomposition of the electrolyte, (3) cation mixing between Li and Mn ion in the spinel lattice (4) oxygen loss from the spinel lattice and (5) break down of the spinel lattice. Novel transition metal nanocomposite (M_x = Cu-Au) doped $LiMn_2O_4$ with improved stability and electrochemical performances has been successfully designed and synthesized. Since the metal nanocomposite can penetrate the surface of the spinel $LiMn_2O_4$, the modified $LiM_xMn_2O_4$ suppress the Jahn-Teller distortion. Good reproducibility was obtained after several experimental runs. LIBs have large spread application in computers, cars, and also medical dispositive purposes. At present time, their main limitation is that their capacity density cannot exceed 200 $\mu Ahcm^{-2}$. In order to increase that, it is suggested that nanomaterials used in positive and negative electrode should have the following characteristics: a high surface area which will be able to enhance electrochemical performances in order to improve their discharge capacity. This work exploited a novel approach for the surface modification of $LiMn_2O_4$ through doping of Cu-Au nanocomposite in order to improve the electrochemical performances of the $LiMn_2O_4$ cathode material. In fulfilment of the research criteria, following primary objectives were achieved:

- The successful synthesis of $LiMn_2O_4$ cathode material via co-precipitation method and Cu-Au nanocomposite via chemical reduction method by the reduction of copper acetate and gold acetate using sodium citrate.
- Doping the pristine $LiMn_2O_4$ cathode materials with an adequate amount of Cu-Au nanocomposite
- Spectroscopic and microscopic sample analysis of pristine $LiMn_2O_4$, Cu-Au nanocomposite and the modified cathode materials via X-ray diffraction (XRD), thermal gravimetric analysis (TGA), resolution scanning electron microscopy (HRSEM), high resolution transmission electron microscopy (HRTEM), fourier-transform infra-red (FTIR), ultraviolet visible spectroscopy (Uv-vis) and cyclic voltammetry (CV), electrochemical impedance spectroscopy (EIS)

The results obtained from that UV-visible results show the presence of red shift for the Cu-Au nanocomposite compared to the pure gold nanoparticles that have a narrower peak which implies that the synthesized Cu-Au nanocomposite has a larger particle distribution. The energy band gap of 2.28 eV was obtained for the synthesized Cu-Au nanocomposite which suggested that it's a semiconductor. Henceforth the synthesized Cu-Au nanocomposite would be able to enhance the conductivity of the synthesized cathode materials. HRTEM results showed that the negatively charged sodium citrate molecules were adsorbed on the surface of the nanocomposite leading to a repulsion of the nanoparticles against each other thus stabilizing the nanocomposite by stemming aggregation. Therefore a well dispersed Cu-Au nanocomposite was obtained with a size range between 20 -30 nm. A mixture of the novel Cu-Au nanocomposite with pristine $LiMn_2O_4$ was used for the synthesis of $LiM_xMn_{2-x}O_4$. XRD analysis of the modified $LiM_xMn_{2-x}O_4$ revealed good crystallinity with an increase in peak intensity. The main diffraction patterns at: (111), (311) and (400) were found to be at their specific 2θ values for both the modified and unmodified samples which denote an unaltered spinel structure after modification. HRSEM micrograph of the pristine $LiMn_2O_4$ shows two types of particles: small particles with a shape of spinel of about 50 nm and the second type of particles are much bigger with a size of more or less 100 nm and are well agglomerated by those smaller particles. In addition the Cu-Au nanocomposite appeared as well dispersed tinny spherical particles across the pristine $LiMn_2O_4$. HRSEM micrograph of $LiM_xMn_{2-x}O_4$ showed well-developed octahedral structures with sharp edges, which was bounded by eight (111) planes. The pristine $LiMn_2O_4$ has obvious visible fringes, indicating that the crystals of spinel $LiMn_2O_4$ grow very well and have good crystallinity which agrees with the XRD results. The EDX confirms that manganese appears at: Kα = 5.8951 KeV and Lα = 0.6374 whereas the oxygen appears at: Kα = 0.5249 KeV. FTIR results showed a presence of MnO_6 frequency bands responsible for the formation of spinel $LiMn_2O_4$.

The thermal gravimetric analysis (TGA) of pristine $LiMn_2O_4$ shows the weight lost loss takes place in three different regions: 20-200 ^oC, 200-500 ^oC and 500-600^oC. Additionally there is about 2.5% weight loss when the sample was heated to 200 °C, which is attributed to the adsorption of water. From 200 and 350 °C, about 5.5% weight loss is attributed to removal of acetates, followed by 2 wt% loss due to the elimination of the surfactant. The cyclic voltammetry of pristine $LiMn_2O_4$ didn't show any two distinct peaks for oxidation and reduction as found in the literature, but the broadening in peaks tells us that the process takes place in two different steps as found by some researchers as well. The first peak is accredited to the removal of lithium ions from the tetrahedral sites where Li–Li interactions occur, whereas the second peak is attributed to the removal of lithium ions again from the tetrahedral

sites but where Li–Li interaction does not occur. Moreover, the modified $LiMn_2O_4$ showed an improvement in the electrochemical performance which lead to an increase in discharge capacity as it was found to be 153 mAh / g which is higher than the theoretical value (148 mAh / g) reported in literature (Yi et al., 2007). The decrease in R_{ct} for $LiM_xMn_{2-x}O_4$ proves that the modified cathode material has lower electrochemical polarization, faster lithium- ion diffusion rates and increase material conductivity attributed to the presence of Cu-Au nanocomposite in the cathode material which concomitantly leads to improved cycle performance.

Based on the results obtained, it can be concluded that the research approach used here, is a viable method for synthesizing electrochemically enhanced $LiMn_2O_4$ cathode material for Li-ion batteries. The surface modification of $LiMn_2O_4$ through Cu-Au nanocomposite has shown a decrease in the dissolution of Mn^{2+} in the electrolyte. Additionally, it has proven to enhance the conductivity and provide short charge transportation distance due to smaller particle size of the cathode material leading to the improvement of its electrochemical performances. These improvements present the Cu-Au nanocomposite doped-$LiMn_2O_4$ as a promising cathode material for high power LIBs, solar cell and supercapacitors applications.

6.2 Recommendations

The future work that has to be done involve:
Characterizations such as:
Nuclear magnetic resonance (NMR), in order to investigate if the Jahn-Teller distortion has been diminished

Inductive Couple plasma (ICP), which would allow us to verify the amount of $LiMn_2O_4$ dissolution in the electrolyte during electrochemical characterization before and after surface modification.

The exploration of other nanocomposites that may be used in order to improve the electrochemical performances of the cathode material.

The application of the synthesized cathode material in a real Li-ion battery.

REFERENCES

ALONSO, J., DIAMANT, R., CASTILLO, P., ACOSTA–GARCÍA, M., BATINA, N. & HARO-PONIATOWSKI, E. **2009**. Thin films of silver nanoparticles deposited in vacuum by pulsed laser ablation using a YAG: Nd laser. *Applied Surface Science,* 255**,** 4933-4937.

ABELA, R., BRAUN, H., MING, P., PEDROZZI, M., QUITMANN, C., REICHE, S., DAALEN, M. V., VAN DER VEEN, J., MESOT, J. & SHIROKA, T. **2009**. Ultrafast phenomena at the nanoscale: science opportunities at the SwissFEL X-ray laser. Paul Scherrer Institute (PSI), Villigen (Switzerland).

AMATUCCI, G., TARASCON, J. & KLEIN, L. **1996**. Cobalt dissolution in $LiCoO_2$ non-aqueous rechargeable batteries. *Solid State Ionics,* 83**,** 167-173.

AMDOUNI, N., ZAGHIB, K., GENDRON, F., MAUGER, A. & JULIEN, C. **2006**. Structure and insertion properties of disordered and ordered $LiNi_{0.5}Mn_{1.5}O_4$ spinels prepared by wet chemistry. *Ionics,* 12**,** 117-126.

ARICÒ, A. S., BRUCE, P., SCROSATI, B., TARASCON, J.-M. & VAN SCHALKWIJK, W. **2005**. Nanostructured materials for advanced energy conversion and storage devices. *Nature materials,* 4**,** 366-377.

ARIGA, K., KROTO, H. & O'BRIEN, P. **2012**. *Manipulation of Nanoscale Materials: An Introduction to Nanoarchitectonics,* Royal Society of Chemistry.

AURBACH, D., EIN-ELY, Y. & ZABAN, A. **1994**. The surface chemistry of lithium electrodes in alkyl carbonate solutions. *Journal of the Electrochemical Society,* 141**,** L1-L3.

AURBACH, D., ZABAN, A., EIN-ELI, Y., WEISSMAN, I., CHUSID, O., MARKOVSKY, B., LEVI, M., LEVI, E., SCHECHTER, A. & GRANOT, E. **1997**. Recent studies on the correlation between surface chemistry, morphology, three-dimensional structures and performance of Li and Li-C intercalation anodes in several important electrolyte systems. *Journal of Power Sources,* 68**,** 91-98.

ZABAN, D., A., SCHECHTER, A., EIN-ELI, Y., ZINIGRAD, E. & MARKOVSKY, B. **1995**. The Study of Electrolyte Solutions Based on Ethylene and Diethyl Carbonates for Rechargeable Li Batteries I. Li Metal Anodes. *Journal of the Electrochemical Society,* 142**,** 2873-2882.

BALAJI, S., MANICHANDRAN, T. & MUTHARASU, D. **2012**. A comprehensive study on influence of Nd^{3+} substitution on properties of $LiMn_2O_4$. *Bulletin of Materials Science,* 35**,** 471-480.

BALAYA, P., BHATTACHARYYA, A. J., JAMNIK, J., ZHUKOVSKII, Y. F., KOTOMIN, E. A. & MAIER, J. **2006**. Nano-ionics in the context of lithium batteries. *Journal of Power Sources,* 159**,** 171-178.

BARD, A. J. & FAULKNER, L. R. **1980**. *Electrochemical methods: fundamentals and applications*, Wiley New York.

BAZITO, F. F. & TORRESI, R. M. **2006**. Cathodes for lithium ion batteries: the benefits of using nanostructured materials. *Journal of the Brazilian Chemical Society,* 17**,** 627-642.

BENBOW, E., KELLY, S., ZHAO, L., REUTENAUER, J. & SUIB, S. **2011**. Oxygen reduction properties of bifunctional α-manganese oxide electrocatalysts in aqueous and organic electrolytes. *The Journal of Physical Chemistry C,* 115**,** 22009-22017.

BESENHARD, J. & EICHINGER, G. **1976**. High energy density lithium cells: Part I. Electrolytes and anodes. *Journal of Electroanalytical Chemistry and Interfacial Electrochemistry,* 68**,** 1-18.

BRUCE, P. G., SCROSATI, B. & TARASCON, J. M. **2008**. Nanomaterials for rechargeable lithium batteries. *Angewandte Chemie International Edition,* 47**,** 2930-2946.

CAO, G. **2004**. *Synthesis, Properties and Applications,* World Scientific.

CHAN, H.-W., DUH, J.-G. & LEE, J.-F. **2006**. Valence change by in situ XAS in surface modified $LiMn_2O_4$ for Li-ion battery. *Electrochemistry Communications,* 8**,** 1731-1736.

CHAN, H.-W., DUH, J.-G., SHEEN, S.-R., TSAI, S.-Y. & LEE, C.-R. **2005**. New surface modified material for $LiMn_2O_4$ cathode material in Li-ion battery. *Surface and Coatings Technology*, 200**,** 1330-1334.

CHAN, H., DUH, J. & SHEEN, S. **2003a**. $LiMn_2O_4$ cathode doped with excess lithium and synthesized by co-precipitation for Li-ion batteries. *Journal of Power Sources,* 115**,** 110-118.

CHAN, H. W., DUH, J. G. & SHEEN, S. R. **2003b**. $LiMn_2O_4$ cathode doped with excess lithium and synthesized by co-precipitation for Li-ion batteries. *Journal of Power Sources,* 115**,** 110-118.

CHANG, S. H., RYU, K. S., KIM, K. M., KIM, M. S., KIM, I. K. & KANG, S. G. **1999**. Electrochemical properties of cobalt-exchanged spinel lithium manganese oxide. *Journal of Power Sources,* 84**,** 134-137.

CHERSTIOUK, O., SIMONOV, P. & SAVINOVA, E. **2003**. Model approach to evaluate particle size effects in electrocatalysis: preparation and properties of Pt nanoparticles supported on GC and HOPG. *Electrochimica Acta,* 48**,** 3851-3860.

CHURIKOV, A., KACHIBAYA, E., SYCHEVA, V., IVANISHCHEVA, I., IMNADZE, R., PAIKIDZE, T. & IVANISHCHEV, A. **2009**. Electrochemical properties of $LiMn_{2-y}Me_yO_4$ (Me= Cr, Co, Ni) spinels as cathodic materials for lithium-ion batteries. *Russian Journal of Electrochemistry,* 45**,** 175-182.

CURTIS, C. J., WANG, J. & SCHULZ, D. L. **2004**. Preparation and Characterization of $LiMn_2O_4$ Spinel Nanoparticles as Cathode Materials in Secondary Li Batteries. *Journal of the Electrochemical Society,* 151**,** A590-A598.

DAHN, J., FULLER, E., OBROVAC, M. & VON SACKEN, U. **1994**. Thermal stability of Li_xCoO_2, Li_xNiO_2 and λ-MnO_2 and consequences for the safety of Li-ion cells. *Solid State Ionics,* 69**,** 265-270.

DANIEL, M.-C. & ASTRUC, D. **2004**. Gold nanoparticles: assembly, supramolecular chemistry, quantum-size-related properties, and applications toward biology, catalysis, and nanotechnology. *Chemical Reviews,* 104**,** 293-346.

DEVARAJAN, S., VIMALAN, B. & SAMPATH, S. **2004**. Phase transfer of Au–Ag alloy nanoparticles from aqueous medium to an organic solvent: effect of aging of surfactant on the formation of Ag-rich alloy compositions. *Journal of Colloid and Interface Science,* 278**,** 126-132.

DOEFF, M. M. **2013**. Battery Cathodes. *Batteries for Sustainability.* Springer.

DRESSELHAUS, M., THOMAS, I., GRÄTZEL, M., STEELE, B. C., HEINZEL, A., SCHLAPBACH, L., ZÜTTEL, A., TARASCON, J. & ARMAND, M. **2001**. Materials for clean energy. *Nature,* 414**,** 332-337.

DU, G., SHARMA, N., PETERSON, V. K., KIMPTON, J. A., JIA, D. & GUO, Z. **2011**. Br-Doped Li4Ti5O_{12} and Composite TiO2 Anodes for Li-ion Batteries: Synchrotron X-Ray and in situ Neutron Diffraction Studies. *Advanced Functional Materials,* 21**,** 3990-3997.

EFTEKHARI, A. **2003**. Mixed-Metals Codeposition as a Novel Method for the Preparation of $LiMn_2O_4$ Electrodes with Reduced Capacity Fades. *Journal of the Electrochemical Society,* 150**,** A966-A969.

EICHINGER, G. & BESENHARD, J. O. **1976**. High energy density lithium cells: Part II. Cathodes and complete cells. *Journal of Electroanalytical Chemistry and Interfacial Electrochemistry,* 72**,** 1-31.

EIN-ELI, Y., URIAN, R., WEN, W. & MUKERJEE, S. **2005**. Low temperature performance of copper/nickel modified $LiMn_2O_4$ spinels. *Electrochimica Acta,* 50**,** 1931-1937.

FERGUS, J. W. **2010**. Recent developments in cathode materials for lithium ion batteries. *Journal of Power Sources,* 195**,** 939-954.

FERRANDO, R., JELLINEK, J. & JOHNSTON, R. L. **2008**. Nanoalloys: From theory to applications of alloy clusters and nanoparticles. *Chem. Rev.,* 108**,** 845-910.

FEY, G., WANG, K. & YANG, S. **1997**. New inverse spinel cathode materials for rechargeable lithium batteries. *Journal of Power Sources,* 68**,** 159-165.1-27.

GOSSER, D. K. **1993**. *Cyclic voltammetry: simulation and analysis of reaction mechanisms*, VCH New York.

GUMMOW, R., DE KOCK, A. & THACKERAY, M. **1994**. Improved capacity retention in rechargeable 4 V lithium/lithium-manganese oxide (spinel) cells. *Solid State Ionics,* 69**,** 59-67.

GUYOMARD, D. & TARASCON, J. **1994**. The carbon/$Li_{1+x}Mn_2O$system. *Solid State Ionics,* 69**,** 222-237.

HA, H.-W., YUN, N. J. & KIM, K. **2007**. Improvement of electrochemical stability of $LiMn_2O_4$ by CeO_2 coating for lithium-ion batteries. *Electrochimica Acta,* 52**,** 3236-3241.

Hallam, S. Infrared Absorption Spectroscopy-Theoritical Principles. University Biosciences Online Learning, **2010**. March 12, **2014**.

HEBIÉ, S., KOKOH, K. B., SERVAT, K. & NAPPORN, T. **2013**. Shape-dependent electrocatalytic activity of free gold nanoparticles toward glucose oxidation. *Gold Bulletin,* 46**,** 311-318.

HU, M., PANG, X. & ZHOU, Z. **2013**. Recent progress in high-voltage lithium ion batteries. *Journal of Power Sources,* 237**,** 229-242.

HU, M. Z. & EASTERLY, C. E. **2009**. A novel thermal electrochemical synthesis method for production of stable colloids of "naked" metal (Ag) nanocrystals. *Materials Science and Engineering: C,* 29**,** 726-736.

HUANG, X. & EL-SAYED, M. A. **2010**. Gold nanoparticles: optical properties and implementations in cancer diagnosis and photothermal therapy. *Journal of Advanced Research,* 1**,** 13-28.

HUNTER, J. C. **1981**. Preparation of a new crystal form of manganese dioxide: λ-MnO_2. *Journal of. Solid State Chemistry,* 39**,** 142-147.

HUSAIN, I. **2011**. *Electric and hybrid vehicles: design fundamentals,* CRC press.

JANG, D. H., SHIN, Y. J. & OH, S. M. **1996**. Dissolution of Spinel Oxides and Capacity Losses in 4 V Li/$L_xMn_2O_4$ Cells. *Journal of the Electrochemical Society,* 143**,** 2204-2211.

JIANG, Z. & ABRAHAM, K. **1996**. Preparation and Electrochemical Characterization of Micron-Sized Spinel $LiMn_2O_4$. *Journal of the Electrochemical Society,* 143**,** 1591-1598.

KAKUDA, T., UEMATSU, K., TODA, K. & SATO, M. **2007**. Electrochemical performance of Al-doped $LiMn_2O_4$ prepared by different methods in solid-state reaction. *Journal of Power Sources,* 167**,** 499-503.

KAMARULZAMAN, N., YUSOFF, R., KAMARUDIN, N., SHAARI, N., ABDUL AZIZ, N., BUSTAM, M., BLAGOJEVIC, N., ELCOMBE, M., BLACKFORD, M. & AVDEEV, M. **2009**. Investigation of cell parameters, microstructures and electrochemical behaviour of $LiMn_2O_4$normal and nano powders. *Journal of Power Sources,* 188**,** 274-280.

KIANI, M., MOUSAVI, M. & RAHMANIFAR, M. **2011**. Synthesis of Nano-and Micro-Particles of $LiMn_2O_4$: Electrochemical Investigation and Assessment as a Cathode in Li Battery. *Int. J. Electrochem. Sci,* 6**,** 2581-2595.

KIM, K. W., LEE, S.-W., HAN, K.-S., CHUNG, H. J. & WOO, S. I. **2003**. Characterization of Al-doped spinel LiMn2O4 thin film cathode electrodes prepared by Liquid Source Misted Chemical Deposition (LSMCD) technique. *Electrochimica Acta,* 48**,** 4223-4231.

KIRKLAND, A. & HUTCHISON, J. **2007**. *Nanocharacterisation,* Royal Society of Chemistry.

KURIBAYASHI, I., YOKOYAMA, M. & YAMASHITA, M. **1995**. Battery characteristics with various carbonaceous materials. *Journal of Power Sources,* 54**,** 1-5.

LANGILLE, M. R., PERSONICK, M. L., ZHANG, J. & MIRKIN, C. A. **2012**. Defining rules for the shape evolution of gold nanoparticles. *Journal of the American Chemical Society,* 134**,** 14542-14554.

LENG, Y. **2008**. X-Ray Diffraction Methods. *Materials Characterization.* John Wiley & Sons (Asia) Pte Ltd.

LI, X. & XU, Y. **2008**. Enhanced cycling performance of spinel $LiMn_2O_4$ coated with $ZnMn_2O_4$ shell. *Journal of Solid State Electrochemistry,* 12**,** 851-855.

LIANG, R.-F., WANG, Z.-X., GUO, H.-J., LI, X.-H., PENG, W.-J. & WANG, Z.-G. **2008**. Fabrication and electrochemical properties of lithium-ion batteries for power tools. *Journal of Power Sources,* 184**,** 598-603.

LIU, D.-Q., HE, Z.-Z. & LIU, X.-Q. **2007a**. Synthesis and characterization of $LiGa_xMn_{2-x}O_4$ (0≤< i> x</i>≤ 0.05) by triethanolamine-assisted sol–gel method. *Journal of Alloys and Compounds,* 440**,** 69-73.

LIU, D.-Q., LIU, X.-Q. & HE, Z.-Z. **2007b**. The elevated temperature performance of $LiMn_2O_4$ coated with $Li_4Ti_5O_{12}$ for lithium ion battery. *Materials Chemistry and Physics,* 105**,** 362-366.

LIU, H., WU, Y., RAHM, E., HOLZE, R. & WU, H. **2004**. Cathode materials for lithium ion batteries prepared by sol-gel methods. *Journal of Solid State Electrochemistry,* 8**,** 450-466.

LIU, Q., WANG, S., TAN, H., YANG, Z. & ZENG, J. **2013**. Preparation and Doping Mode of Doped $LiMn_2O_4$ for Li-Ion Batteries. *Energies,* 6**,** 1718-1730.

LIU, Y., FUJIWARA, T., YUKAWA, H. & MORINAGA, M. **2001**. *Electrochim. Acta,* 46**,** 1151.

LU, Z., MACNEIL, D. & DAHN, J. **2001**. Layered cathode materials $Li[Ni_xLi_{(1/3-2x/3)}Mn_{(2/3-x/3)}]O_2$ for lithium-ion batteries. *Electrochemical and solid-state letters,* 4**,** A191-A194.

MACDONALD, D. D. **2006**. Reflections on the history of electrochemical impedance spectroscopy. *Electrochimica Acta,* 51**,** 1376-1388.

MARTIN, L. **2013**. *Etude de l'oxyde de cuivre CuO, matériau de conversion en film mince pour microbatteries au lithium: caractérisation des processus électrochimiques et chimiques en cyclage.* Pau.

MCFARLAND, A. D., HAYNES, C. L., MIRKIN, C. A., VAN DUYNE, R. P. & GODWIN, H. A. **2004**. Color my nanoworld. *Journal of Chemical Education,* 81**,** 544A.

MENG, Y. S. & ARROYO-DE DOMPABLO, M. E. **2009**. First principles computational materials design for energy storage materials in lithium ion batteries. *Energy & Environmental Science,* 2**,** 589-609.

MOHAMEDI, M., TAKAHASHI, D., UCHIYAMA, T., ITOH, T., NISHIZAWA, M. & UCHIDA, I. **2001**. Explicit analysis of impedance spectra related to thin films of spinel $LiMn_2O_4$. *Journal of Power Sources,* 93**,** 93-103.

MONK, P. M. **2008**. *Fundamentals of electro-analytical chemistry,* John Wiley & Sons.

NAGAURA, T. & TOZAWA, K. **1990**. Lithium ion rechargeable battery. *Prog. Batteries Solar Cells,* 9**,** 209.

NAGHASH, A. & LEE, J. Y. **2000**. Preparation of spinel lithium manganese oxide by aqueous co-precipitation. *Journal of Power Sources,* 85**,** 284-293.

ODANI, A., NIMBERGER, A., MARKOVSKY, B., SOMINSKI, E., LEVI, E., KUMAR, V., MOTIEI, M., GEDANKEN, A., DAN, P. & AURBACH, D. **2003**. Development and testing of nanomaterials for rechargeable lithium batteries. *Journal of Power Sources,* 119**,** 517-521.

OH, S. W., MYUNG, S.-T., BANG, H. J., YOON, C. S., AMINE, K. & SUN, Y.-K. **2009**. Nanoporous structured LiFePO4 with spherical microscale particles having high volumetric capacity for lithium batteries. *Electrochemical and solid-state letters,* 12**,** A181-A185.

OKADA, M., LEE, Y.-S. & YOSHIO, M. **2000**. Cycle characterizations of $LiM_xMn_{2-x}O_4$ (M = Co, Ni) materials for lithium secondary battery at wide voltage region. *Journal of Power Sources,* 90**,** 196-200.

PAL, A., SHAH, S., KULKARNI, V., MURTHY, R. & DEVI, S. **2009**. Template free synthesis of silver–gold alloy nanoparticles and cellular uptake of gold nanoparticles in Chinese Hamster Ovary cell. *Materials Chemistry and Physics,* 113**,** 276-282.

PAULSEN, J., THOMAS, C. & DAHN, J. **2000**. O_2 Structure $Li_{2/3}[Ni_{1/3}Mn_{2/3}]O_2$: A New Layered Cathode Material for Rechargeable Lithium Batteries. I. Electrochemical Properties. *Journal of the Electrochemical Society,* 147**,** 861-868.

PISTOIA, G., ANTONINI, A., ROSATI, R., BELLITTO, C. & INGO, G. **1997**. Doped Li-Mn spinels: physical/chemical characteristics and electrochemical performance in Li batteries. *Chemistry of materials,* 9**,** 1443-1450.

PISTOIA, G. & WANG, G. **1993**. Aspects of the Li^+insertion into $Li_xMn_2O_4$ for 0<< i> x</i>< 1. *Solid State Ionics,* 66**,** 135-142.

POLO FONSECA, C., BELLEI, M., AMARAL, F., CANOBRE, S. & NEVES, S. **2009**. Synthesis and characterization of $LiM_xMn_{2-x}O_4$ (M = Al, Bi and Cs ions) films for lithium ion batteries. *Energy Conversion and Management,* 50**,** 1556-1562.

PRÖLL, J., KOHLER, R., TORGE, M., ULRICH, S., ZIEBERT, C., BRUNS, M., SEIFERT, H. & PFLEGING, W. **2011**. Laser microstructuring and annealing processes for lithium manganese oxide cathodes. *Applied Surface Science,* 257**,** 9968-9976.

RAJA, M. W., MAHANTY, S. & BASU, R. N. **2009**. Influence of S and Ni co-doping on structure, band gap and electrochemical properties of lithium manganese oxide synthesized by soft chemical method. *Journal of Power Sources,* 192**,** 618-626.

RAO, M. M., LIEBENOW, C., JAYALAKSHMI, M., WULFF, H., GUTH, U. & SCHOLZ, F. **2001**. High-temperature combustion synthesis and electrochemical characterization of $LiNiO_2$, $LiCoO_2$ and $LiMn_2O_4$ for lithium-ion secondary batteries. *Journal of Solid State Electrochemistry,* 5**,** 348-354.

ROBERTSON, A., LU, S., AVERILL, W. & HOWARD, W. **1997**. M^{3+}-Modified $LiMn_2O_4$ Spinel Intercalation Cathodes I. Admetal Effects on Morphology and Electrochemical Performance. *Journal of the Electrochemical Society,* 144**,** 3500-3505.

RODRIGUEZ-CARVAJAL, J., ROUSSE, G., MASQUELIER, C. & HERVIEU, M. **1998**. Electronic crystallization in a lithium battery material: columnar ordering of electrons and holes in the spinel $LiMn_2O_4$. *Physical review letters,* 81**,** 4660.

ROSSOUW, M., DE KOCK, A., DE PICCIOTTO, L., THACKERAY, M., DAVID, W. & IBBERSON, R. **1990**. Structural aspects of lithium-manganese-oxide electrodes for rechargeable lithium batteries. *Materials research bulletin,* 25**,** 173-182.

SAıDI, M., BARKER, J., HUANG, H., SWOYER, J. & ADAMSON, G. **2003**. Performance characteristics of lithium vanadium phosphate as a cathode material for lithium-ion batteries. *Journal of Power Sources,* 119**,** 266-272.

SAU, T. K. & MURPHY, C. J. **2004**. Room temperature, high-yield synthesis of multiple shapes of gold nanoparticles in aqueous solution. *Journal of the American Chemical Society,* 126**,** 8648-8649.

SCHOONMAN, J., TULLER, H. & KELDER, E. **1999**. Defect chemical aspects of lithium-ion battery cathodes. *Journal of Power Sources,* 81**,** 44-48.

SHAFIEE, S. & TOPAL, E. **2009**. When will fossil fuel reserves be diminished? *Energy Policy,* 37**,** 181-189.

SHI, J. Y., YI, C.-W. & KIM, K. 2**010**. Improved electrochemical performance of $AlPO^{4-}$ coated $LiMn_{1.5}Ni_{0.5}O_4$ electrode for lithium-ion batteries. *Journal of Power Sources,* 195**,** 6860-6866.

SHIN, Y., BAE, I.-T., AREY, B. W. & EXARHOS, G. J. **2008**. Facile stabilization of gold-silver alloy nanoparticles on cellulose nanocrystal. *The Journal of Physical Chemistry C,* 112**,** 4844-4848.

SIDES, C. R., CROCE, F., YOUNG, V. Y., MARTIN, C. R. & SCROSATI, B. **2005**. A High-Rate, Nanocomposite $LiFePO_4$/ Carbon Cathode. *Electrochemical and solid-state letters,* 8**,** A484-A487.

SON, J., PARK, K., KIM, H. & CHUNG, H. **2004**. Surface-modification of $LiMn_2O_4$ with a silver-metal coating. *Journal of Power Sources,* 126**,** 182-185.

STAROWICZ, M., STYPUŁA, B. & BANAŚ, J. **2006**. Electrochemical synthesis of silver nanoparticles. *Electrochemistry Communications,* 8**,** 227-230.

SUN, H., CHEN, Y., XU, C., ZHU, D. & HUANG, L. **2012**. Electrochemical performance of rare-earth doped $LiMn_2O_4$ spinel cathode materials for Li-ion rechargeable battery. *Journal of Solid State Electrochemistry,* 16**,** 1247-1254.

TALEB, A., PETIT, C. & PILENI, M. **1997**. Synthesis of highly monodisperse silver nanoparticles from AOT reverse micelles: a way to 2D and 3D self-organization. *Chemistry of materials,* 9**,** 950-959.

TAN, S. M. & JOHAN, M. R. **2011**. Effects of MnO_2 nano-particles on the conductivity of PMMA-PEO-$LiClO_4$-EC polymer electrolytes. *Ionics,* 17**,** 485-490.

TARASCON, J., COOWAR, F., AMATUCI, G., SHOKOOHI, F. & GUYOMARD, D. **1995**. The $Li_{1+x}Mn_2O_4$ C system Materials and electrochemical aspects. *Journal of Power Sources,* 54**,** 103-108.

TARASCON, J. M. & ARMAND, M. **2001**. Issues and challenges facing rechargeable lithium batteries. *Nature,* 414**,** 359-367.

TAY, S. F. & JOHAN, M. R. **2010**. Synthesis, structure, and electrochemistry of Ag-modified $LiMn_2O_4$ cathode materials for lithium-ion batteries. *Ionics,* 16**,** 859-863.

THACKERAY, M. **1995**. Structural considerations of layered and spinel lithiated oxides for lithium ion batteries. *Journal of the Electrochemical Society,* 142**,** 2558-2563.

THACKERAY, M., DE KOCK, A. & DAVID, W. **1993**. Synthesis and structural characterization of defect spinels in the lithium-manganese-oxide system. *Materials research bulletin,* 28**,** 1041-1049.

THIRUNAKARAN, R., KIM, K.-T., KANG, Y.-M. & LEE, J.-Y. **2004**. Solution synthesis of boron substituted LiMn2O4 spinel oxide for use in lithium rechargeable battery. *Ionics,* 10**,** 188-192.

TU, J., ZHAO, X., CAO, G., ZHUANG, D., ZHU, T. & TU, J. **2006**. Enhanced cycling stability of $LiMn_2O_4$ by surface modification with melting impregnation method. *Electrochimica Acta,* 51**,** 6456-6462.

VAKKASOĞLU, V. **2009**. *Üzüntüsüz Yaşamak*, Nesil Basım Yayın Gıda Ticaret ve Sanayi A. Ş.

VAN DEN BOSSCHE, P., VERGELS, F., VAN MIERLO, J., MATHEYS, J. & VAN AUTENBOER, W. **2006**. SUBAT: An assessment of sustainable battery technology. *Journal of Power Sources,* 162**,** 913-919.

WANG, G., WANG, J., MAO, W., SHAO, H., ZHANG, J. & CAO, C. **2005**. Physical properties and electrochemical performance of LiMn2O4 cathode materials prepared by a precipitation method. *Journal of Solid State Electrochemistry,* 9**,** 524-530.

WANG, J. & SUN, X. **2012**. Understanding and recent development of carbon coating on $LiFePO_4$ cathode materials for lithium-ion batteries. *Energy & Environmental Science,* 5**,** 5163-5185.

WEI, Y. J., YAN, L. Y., WANG, C. Z., XU, X. G., WU, F. & CHEN, G. **2004**. Effects of Ni Doping on [MnO_6] Octahedron in LiMn2O4. *The Journal of Physical Chemistry B,* 108**,** 18547-18551.

WILLIAMS, G. P. **2001**. X-ray data booklet. *X-RAY DATA BOOKLET*.

WINTER, M. & BESENHARD, J. O. **1999**. Electrochemical lithiation of tin and tin-based intermetallics and composites. *Electrochimica Acta,* 45**,** 31-50.

WU, H., TU, J., CHEN, X., LI, Y., ZHAO, X. & CAO, G. **2007**. Effects of Ni-ion doping on electrochemical characteristics of spinel $LiMn_2O_4$ powders prepared by a spray-drying method. *Journal of Solid State Electrochemistry,* 11**,** 173-176.

XIA, Y. **2008**. Development of Low Cost Cathode Materials for Lithium-ion Batteries. *Department of Energy and Materials Science, Graduate School of Science and Engineering (Saga University*.

XIA, Y. & YOSHIO, M. **1997**. Studies on Li-Mn-O spinel system (obtained from melt-impregnation method) as a cathode for 4 V lithium batteries Part IV. High and low temperature performance of $LiMn_2O_4$. *Journal of Power Sources,* 66**,** 129-133.

XU, K. **2004**. Nonaqueous liquid electrolytes for lithium-based rechargeable batteries. *Chemical Reviews,* 104**,** 4303-4418.

YAMADA, A. & TANAKA, M. **1995**. Jahn-Teller structural phase transition around 280 K in $LiMn_2O_4$. *Materials research bulletin,* 30**,** 715-721.

YAMADA, A., TANAKA, M., TANAKA, K. & SEKAI, K. **1999**. Jahn–Teller instability in spinel Li–Mn–O. *Journal of Power Sources,* 81–82**,** 73-78.

YANG, S., JIA, J., DING, L. & ZHANG, M. **2003**. Studies of structure and cycleability of $LiMn_2O_4$ and $LiNd_{0.01}Mn_{1.99}O_4$ as cathode for Li-ion batteries. *Electrochimica Acta,* 48**,** 569-573.

YANG, Z., ZHANG, J., KINTNER-MEYER, M. C., LU, X., CHOI, D., LEMMON, J. P. & LIU, J. **2011**. Electrochemical energy storage for green grid. *Chemical Reviews,* 111**,** 3577-3613.

YI, T.-F., HU, X.-G., DAI, C.-S. & GAO, K. **2007**. Effects of different particle sizes on electrochemical performance of spinel $LiMn_2O_4$ cathode materials. *Journal of materials science,* 42**,** 3825-3830.

YING, J., WAN, C. & JIANG, C. **2001**. Surface treatment of $LiNi_{0.8}Co_{0.2}O_2$ cathode material for lithium secondary batteries. *Journal of Power Sources,* 102**,** 162-166.

YUNJIAN, L., XINHAI, L., HUAJUN, G., ZHIXING, W., QIYANG, H., WENJIE, P. & YONG, Y. **2009**. Electrochemical performance and capacity fading reason of $LiMn_2O_4$ graphite batteries stored at room temperature. *Journal of Power Sources,* 189**,** 721-725.

ZHAO, X., REDDY, M., LIU, H., RAMAKRISHNA, S., RAO, G. S. & CHOWDARI, B. V. **2012**. Nano $LiMn_2O_4$ with spherical morphology synthesized by a molten salt method as cathodes for lithium ion batteries. *RSC Advances,* 2**,** 7462-7469.

ZHOU, M., CHEN, S., ZHAO, S. & MA, H. **2006**. RETRACTED: One-step synthesis of Au–Ag alloy nanoparticles by a convenient electrochemical method. *Physica E: Low-dimensional Systems and Nanostructures,* 33**,** 28-34.

ZHU, H.-L., CHEN, Z.-Y., JI, S. & LINKOV, V. **2008**. Influence of different morphologies on electrochemical performance of spinel $LiMn_2O_4$. *Solid State Ionics,* 179**,** 1788-1793.